ANTHROPOMORPHIC HEAD PHANTOM FOR QUANTITATIVE IMAGE QUALITY ASSESSMENT IN CONE BEAM COMPUTED TOMOGRAPHY

MASTER THESIS

By Yichao Wang BSc - 4104390

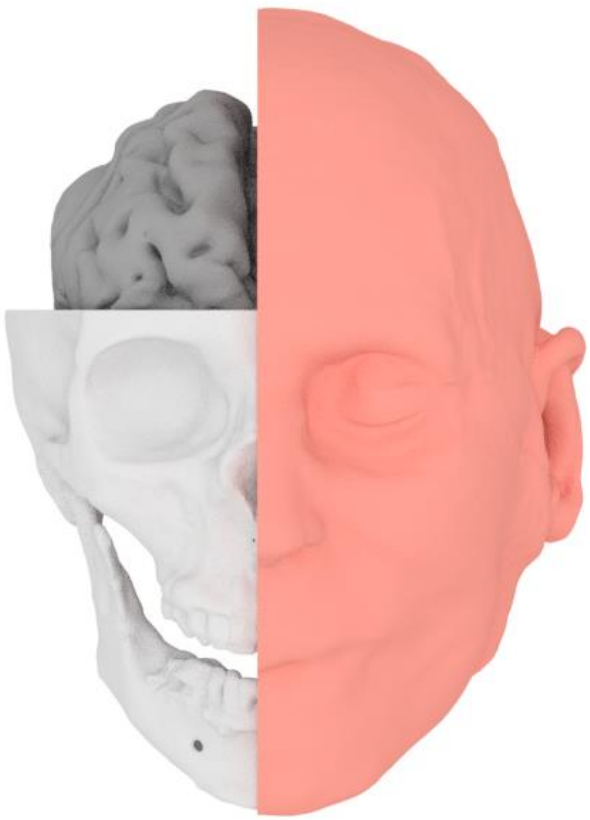

Delft University Of Technology and Philips Healthcare

TU Delft

PHILIPS

Anthropomorphic head phantom for quantitative image quality assessment in cone beam computed tomography

MASTER THESIS

By

Yichao Wang BSc

In partial fulfilment for the requirements for the degree of

Master of Science in Biomedical Engineering

Student number	4104390	
Project duration:	May 15th 2016 – December 30th 2016	
Supervisors:	Prof. dr. Jenny Dankelman	TU Delft
	Dr. ir. Danny Ruijters	Philips Healthcare
Exam committee	Prof. dr. Jenny Dankelman	TU Delft (Chairman)
	Ir. T. de Jong	TU Delft
	Dr. Y. Song	TU Delft
Contact	Email: yichaowang1991@gmail.com	
	Phone: +316 557 31 688	
	Address: Enschotsestraat 165, 5014 DE, Tilburg	

Delft University of Technology and Philips Healthcare

PREFACE

For the last six months I have been performing my graduation project as partial fulfillment for the degree of master of science at Delft university of technology in Delft, the Netherlands. The graduation project was performed in close collaboration with the people from the innovation group within the department of image guided therapy (IGT) at Philips Healthcare in Best, the Netherlands. The goal of this project is to develop an anthropomorphic head phantom that can be used for quantitative image quality assessment of cone beam computed tomography systems. The steps that were taken in order to achieve this goal are described in this thesis.

This project would not have been possible without the many people from both Philips and Delft university of technology, who have supported me in many ways. These people include, Peter van der Haar, Rens Schoones, Arjan Dijke, Richard van der Laan, Menno van Baardwijk and William van der Sterren. I owe special thanks to my weekly supervisor at Philips, Danny Ruijters, who did not only provide useful feedback about my work on a regular basis, but also gave me the possibility to explore my own creativity and ideas. I would also like to thank my supervisor Jenny Dankelman from Delft university of technology for her feedback and support from the side of the university. Furthermore, I would also like to thank my fellow intern Martijn Pieters, who has developed a Monte Carlo based simulation tool for scatter estimation, which has been used many times during this project. Last but not least I would like to thank my parents, friends and girlfriend for their support and motivation throughout my time as a student.

Yichao Wang BSc. - Author

SUMMARY

Cone beam computed tomography (CBCT) is a fast medical imaging technique using x-rays, which can be used for diagnostic and peri-interventional imaging of the head. Unfortunately, soft tissue and brain visualization is still inferior in terms of contrast resolution compared to traditional (fan beam) CT or MRI (among other imaging techniques). One of the causes for the lower contrast resolution of the image is scatter radiation, which causes noise on the flat detector of the CBCT system. Fortunately, researchers have investigated several effective ways to reduce the effects of scatter radiation on the x-ray image. Phantoms are used to physically assess the (enhanced) image quality of the (CB)CT systems and there are several head phantoms that are commonly used for this purpose, including the Rando-Alderson, CIRS ATOM max and ACY Kyoto Kagaku phantom (among others). Unfortunately, these phantoms have several important drawbacks, including an underattenuation (in terms of radiodensity) of the materials that are used in some the phantoms, in the lower diagnostic energy range of the x-ray photons, which could cause a bias during the interpretation of image quality. Another limitation is the lack of inserts that can be used for quantitative evaluation of the image quality (e.g. the contrast or spatial resolution of the image). Furthermore, the materials that are used for the construction of these phantoms were not explicitly evaluated for their scatter characteristics, while scatter is an important aspect of the attenuation characteristics of a material. Some researchers tried to overcome these issues by ordering customized phantoms, where inserts for the measurement of the contrast resolution were added afterwards, or even proposed newly developed phantoms, but customization of the phantoms are extremely costly and therefore, the accessibility to these kind of phantoms is very limited.

It is therefore of importance to address these issues, by investigating the possibilities to develop an improved alternative for the phantoms that are currently available, which has realistic attenuation characteristics (both in terms of the radiodensity and scatter), which has a comparable anatomy to the human head and preferably, which can be fabricated by researchers themselves, using simple and accurate fabrication techniques such as silicone casting and 3D printing.

In this study, a design of the phantom was made, based on CBCT data of an anonymous patient, which is entirely suitable for 3D printing. A range of materials were selected based on the literature, which satisfied the criteria in theory. The materials were evaluated for their radiodensity and scatter characteristics and compared to the theoretical radiodensity and scatter characteristics of bone, muscle and brain tissue. The materials were also used for the fabrication of two prototypes, in order to investigate the practical aspects regarding the suitability for the desired fabrication techniques and imaging aspects.

Preliminary results show that the measured radiodensity of the materials fall within the theoretical range of bone tissue, a mixture of muscle and adipose (fat) tissue and brain tissue. The measured scatter characteristics of the proposed materials, which were quantified in terms of scatter magnitude and distribution had a maximal absolute difference of 3 percent in comparison with simulated scatter characteristics of human tissue, in terms of the normalized magnitude and a maximal absolute difference of 2 percent in terms of the scatter distribution. It was possible to fabricate prototypes using the proposed materials and desired fabrication techniques and while several image artifacts were present (including air bubbles), the overall prototype could be used for quantitative evaluation of the contrast resolution of the image.

From this work, it can be concluded that it is feasible to fabricate a head phantom for quantitative image quality assessment in CT or CBCT, using materials that are suitable for silicone casting or 3D printing. Further optimization of the design and further investigation of novel materials could result in affordable and easily customizable phantoms that can be ‘home made’ fabricated.

TABLE OF CONTENTS

LIST OF ACRONYMS

CBCT	Cone beam computed tomography
CSF	Cerebrospinal fluid
CT	Computed tomography
EM	Edge magnitude
ESF	Edge spread function
FDM	Fused deposition modeling
HU	Hounsfield Unit
IGT	Image guided therapy
IQA	Image quality assessment
IQR	Inter quartile range
MCPH	Monocalcium phosphate
MCPHG	Monocalcium phosphate gypsum mixture
MSPR	Maximal scatter to primary ratio
NIST	National Institute of Standards and Technology
PMMA	Polymethylmethacrylate
SD	Scatter distribution
SLS	Selective laser sintering
SMP	Silyl modified polymer
TEM	Tissue equivalent material

IMPORTANT SYMBOLS AND VARIABLES

I, I_0	Absorbed and incident photon intensity [-]
$K_{1,c}$	Mode 1 stress intensity factor [$MPa^{1/2}$]
μ, μ_m	Linear and mass attenuation coefficient [cm^{-1}]
ρ	Physical density [g/cm^3]
σ	Photon cross section [-]
σ_y	Yield stress [MPa]
x_l, x_c	Lead edge pixel position and collimator edge pixel position [-]
Z, Z_{eff}	Atomic number and effective atomic number [-]

1

INTRODUCTION

1.1 RATIONALE

Cone beam computed tomography (CBCT) is a state of the art technique for medical imaging including diagnostic and peri-interventional imaging of the head, for example to assess tumors, increased intracranial pressure or hemorrhages. For this purpose, it is of importance that the image quality is sufficiently high (in terms of spatial and contrast resolution) in order to visualize the different tissue types within the head. CBCT systems can produce images with excellent spatial resolution, but unfortunately, the contrast resolution is still somewhat inferior when compared to other imaging techniques such as traditional (fan beam) CT or magnetic resonance imaging (MRI) (among other techniques). This is primarily caused by scatter radiation (among other causes). Researchers have investigated several methods to correct for the effects of scatter radiation in the x-ray image some promising results were obtained. In order to physically assess the improved image quality, phantoms can be used. For image quality assessment (IQA) in cranial CBCT procedures, a wide range of commercial head phantoms (figure 1.1) are provided by manufacturers (among others) such as CIRS, QRM, Rando Alderson and Kyoto Kagaku. However, in a previously performed literature study it became clear that these commercial head phantoms have certain drawbacks such as a limited functionality for *quantitative* IQA due to the lack of inserts for the measurement of the spatial resolution and contrast resolution. Furthermore, tissue equivalent materials (TEMs) that are used as substitutes for human tissues in these phantoms often do not have realistic x-ray attenuation characteristics (which are the x-ray absorption and scatter characteristics of a material). This can result in a biased interpretation of the image quality. Some researchers have developed alternatives for the commercial phantoms in an academic setting, by adding inserts for measurement of the contrast resolution. However, these designs still have drawbacks such as an underattenuation of TEMs that are used for the construction of these phantoms. Furthermore, while scatter is an important part of the attenuation characteristics of a material and can influence the image quality from a CT scan directly, it is hardly reported upon by manufacturers and researchers. For these reasons, it is of interest to develop an alternative which overcomes the limitations that the current head phantoms have and to quantify the scatter characteristics of the materials that are used as substitutes for relevant tissues within the human head. Therefore, the following goal was set for this project:

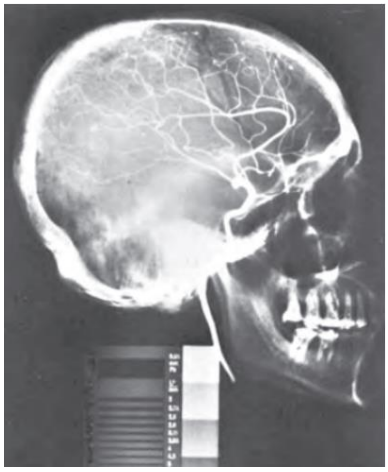

Figure 1.1 - Rando-Alderson head phantom for image quality assessment in computed tomography

To develop a head phantom tool with accurate attenuation (absorption and scatter) characteristics, accurate anatomy and inserts for quantitative image quality assessment.

1.2 APPROACH

The following steps were taken in order to achieve the goal of this project (figure 1.2):

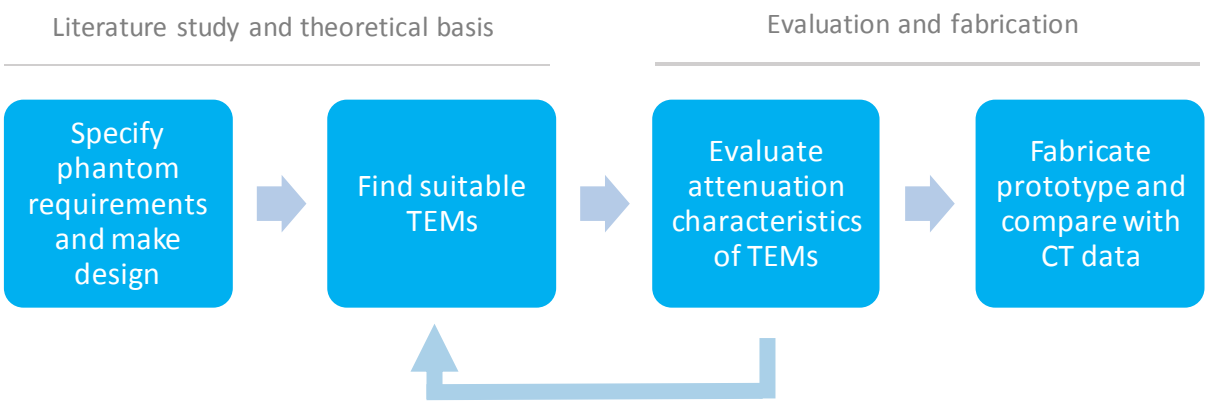

Figure 1.2 – Schematic overview of the approach to achieve the goal of the project.

As a preparation for this project, a literature study was performed to evaluate existing head phantoms that are commonly used for IQA of CBCT systems for their attenuation characteristics and options for quantitative IQA. Based on this evaluation, critical design criteria were formulated.

In the same literature study, TEMs that are commercially used and TEMS that were reported in the literature with representative attenuation characteristics (in terms of mass attenuation coefficient) were evaluated in terms of durability and suitability for the fabrication methods that are available for this project.

Based on the specified critical design criteria from the literature study, a computer model of the head phantom was created and made suitable for the available fabrication techniques for this project (which are simple casting techniques and rapid prototyping via fused deposition modeling or selective laser sintering).

Based on the selected TEMS for further research in this project from the literature study, the attenuation characteristics (both the absorption characteristics (radiodensity) and scatter characteristics) were measured, using a validated experimental setup that was designed specifically for this purpose.

Following from the design and the selected TEMs, a prototype of the head phantom was constructed and compared to actual CT data from which the phantom was based on.

1.3 THESIS ORGANIZATION

This thesis is organized in the following way:

Chapter 2 is a theoretical background about cone beam computed tomography, image quality and image quality assessment using phantom tools, the fundamental physics behind x-ray attenuation and the attenuation characteristics of the human head.

Chapter 3 describes the design of the head phantom, based on the design criteria that followed from the evaluation of anthropomorphic head phantoms for quantitative IQA in CBCT in the literature.

Chapter 4 describes the selection of potentially suitable TEMs for further investigation, based on the literature and describes an alternative approach to find TEMs for bone substitute which were not found in the literature study.

Chapter 5 provides the methodology and the results for the measurement of the radiodensity of the included TEMs.

Chapter 6 provides the methodology and results for the measurement of the scatter characteristics of the included TEMs.

Chapter 7 describes the fabrication steps of two prototypes of the head phantom and provides a qualitative evaluation regarding the usability and practical aspects of the TEMs for the construction of a phantom.

Chapter 8 and 9 are an overall discussion of the results and limitations of the current work and recommendations for future work are provided, followed by a final conclusion.

2

THEORETICAL BACKGROUND[1]

2.1 CONE BEAM COMPUTED TOMOGRAPHY

2.1.1 DESIGN AND BASIC WORKING PRINCIPLE

Cone beam computed tomography (CBCT) is a state of the art imaging technique that uses x-rays to view the (inner) anatomical structure of a region of interest. CBCT systems can be used for many clinical purposes, such as diagnostic imaging, image guided therapy (IGT) and dental CBCT [1]. A modern CBCT system for IGT consists of a C-shaped arm (among other configurations) where an x-ray source is positioned in one end of the C-arm and a digital multi-array flat detector is positioned on the other end of the C-arm (figure 2.1a). By rotating the C-arm while radiating the patient, 3D image reconstructions can be made. Because the x-ray beam is a cone or pyramid shaped beam (figure 2.1b), making such a 3D image reconstruction is a very time-efficient procedure. In fact it takes only several seconds and a single rotation to achieve this.

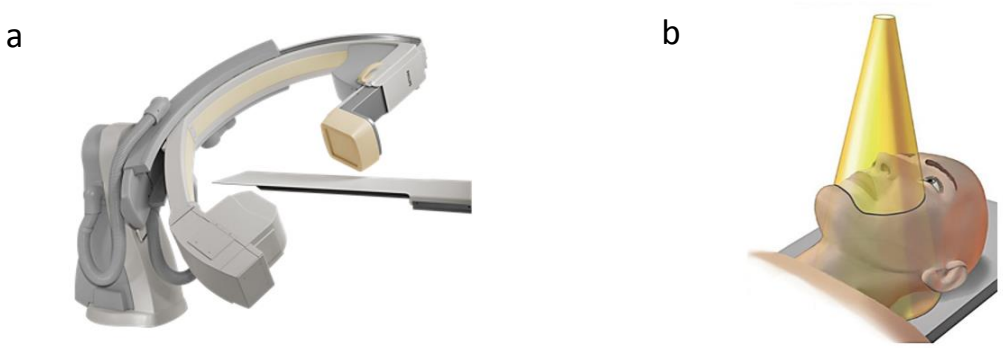

Figure 2.1 - a) Cone beam computed tomography system (Philips Allura FD 10, Philips Healthcare, Best, the Netherlands) b) A cone shaped x-ray beam that is used to scan the region of interest. Adopted from [50][51]

2.1.2 DIAGNOSTIC IMAGING OF THE HEAD

One specific field of application of CBCT is diagnostic and peri-interventional imaging of the head. Examples of such imaging procedures include the detection of hemorrhages, increased intracranial pressure or brain tumors. There are four types of tissue in the human head that are clinically relevant for diagnostic imaging. (1) *Bone tissue*, which can be assessed for fractures. (2) *Brain tissue* and (3) *soft tissue* can be assessed for hemorrhages or abnormal growths such as tumors. Furthermore, (4) *cerebrospinal fluid* (CSF) can be assessed for the detection of increased intracranial pressure. Even though CBCT is versatile in its applications, the image quality when visualizing the brain using CBCT is still inferior in terms of contrast resolution when compared to traditional CT (figure 2.2) [2]. Minor hemorrhages are for example hard to detect due to the relatively low contrast resolution of the image[3] [4]. One phenomenon that can have direct influence on the contrast resolution is called x-ray scatter (see section 2.2 for a detailed explanation of x-ray scatter).

[1] Chapter 2 was directly adopted from a previously performed literature study [15].

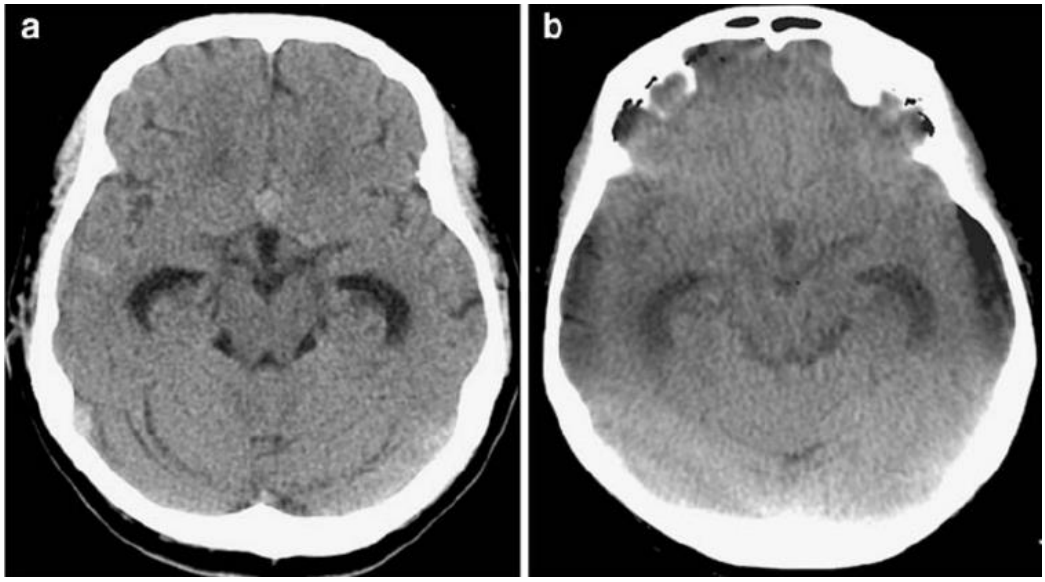

Figure 2.2 – The contrast resolution of cone beam computed tomography (CBCT) is somewhat inferior compared that of traditional computed tomography. a) traditional CT b) CBCT. Adopted from [52]

2.1.3 IMAGE QUALITY AND SCATTER CORRECTION

Because correcting for scatter can greatly improve the image quality (especially the contrast resolution), researchers are constantly investigating novel techniques to do so. A technique that is currently commonly applied in CBCT systems is a physical anti-scatter grid (figure 2.3). Anti-scatter grids are lamellae shaped plates that are positioned in front of the detector of the CBCT system. Because the lamellae are parallel with the x-ray beam, scattered photons are blocked because these photons reach the anti-scatter grid in a different angle. However, in CBCT systems, anti-scatter grids are not always fully effective because the detector can move in a perpendicular direction. Therefore, in some situations the direction of the lamellae are not completely parallel with the x-ray beam anymore [2]. To overcome this problem, researchers have investigated other scatter correction techniques including primary beam modulation and image based scatter estimation and correction. Readers who are interested in this topic are referred to (for example) [5]–[9][8].

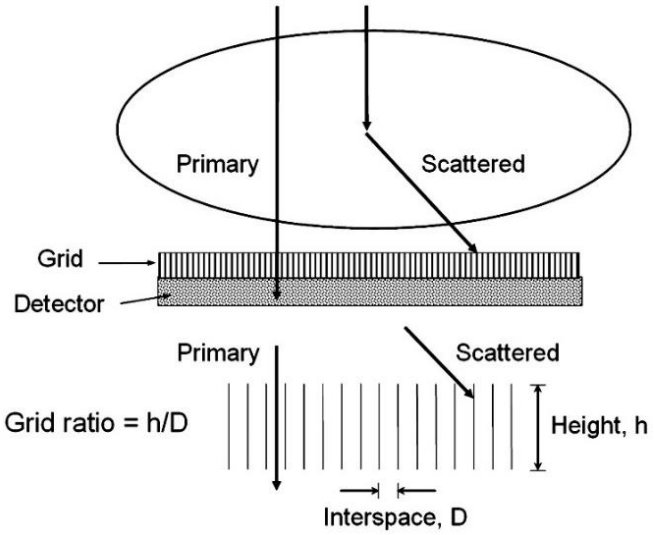

Figure 2.3 – An anti-scatter grid is often positioned in front of the detector of the cone beam computed tomography system and blocks the scattered photons that reach the detector in a different angle. Adopted from [53]

2.1.4 IMAGE QUALITY ASSESSMENT USING PHANTOM TOOLS

To physically assess the effectiveness of these scatter correction techniques (and other image quality related aspects), phantom tools are often used (figure 2.4 a and b). Phantoms tools for quantitative IQA are often equipped with different kinds of inserts. These inserts are used for analyzing different aspects of the image quality, i.e. low contrast inserts have a known radiodensity and can be used to measure the contrast resolution, which is quantified in Hounsfield Units [HU] (figure 2.4c) (a linear scale of grey values of a CT image). Spatial resolution inserts have varying line pair patterns which can be used to measure the sharpness of an image, which is quantified in line pair per centimeter [lp/cm] (figure 2.4d). The number of visible lines are counted to quantify the sharpness of the image. A more thorough evaluation of anthropomorphic head phantoms for IQA in CBCT are provided in chapter 3.

Figure 2.4 – a) Cylindrical phantom tool for quantitative image quality analysis of computed tomography systems. b) An anthropomorphic phantom tool for qualitative image quality assessment. c) Inserts for quantitative analysis of the contrast resolution (range of grey values) of the (CBCT) image. d) Inserts for quantitative analysis of the spatial resolution of the image (sharpness). Adopted from [20], [54].

2.2 X-RAY INTERACTION WITH MATTER

2.2.1 X-RAY ABSORPTION AND SCATTER

In the diagnostic energy range of x-rays (typically between 60 and 160 [kEv]), two types of interactions dominate between the incident photon and the atom of a material. The first type of interaction is called the photoelectric effect, also known as absorption characteristics of a material. The second type of interaction is scattering of the x-ray photons, which can be divided into Compton scattering and Rayleigh scattering. Together, these two types of interaction form the attenuation characteristics of a material (figure 2.5). The following sections in this chapter describe these interacting processes in more detail [2], [10] [11].

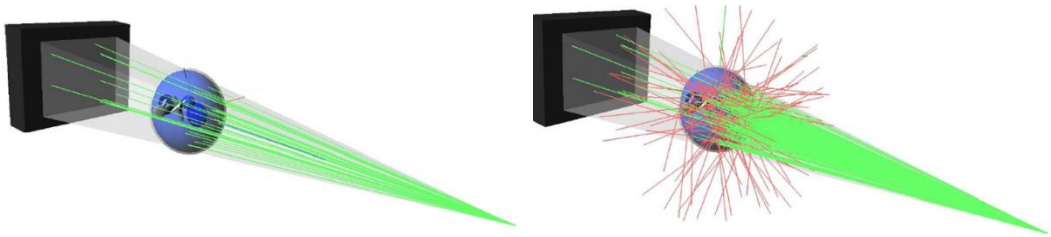

Figure 2.5 – An X-ray image is created when the photons reach the detector after interaction with the material. Only photons from the photoelectric effect are relevant for the generation of the image (left). Photons that are being scattered become useless for the generation of the image(right). Adopted and modified from [2].

The photoelectric effect

The photoelectric effect occurs at the K-shell (most inner shell) of an atom. An incident photon enters and collides with an electron in the K-shell and thereby ejects that electron from the K-shell. The ejected electron creates a vacancy in the K-shell that gets filled with an electron from an outer shell with a lower binding energy (figure 2.6). During this transition, the energy that comes free is emitted as x-radiation. The probability that this effect occurs depends mainly on the mass density (ρ) of the material and on the type of atom. The probability is proportional to the energy of the x-ray beam.

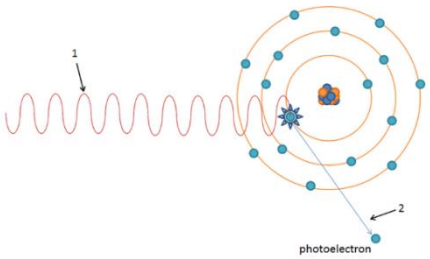

Figure 2.6 – Schematic drawing of the photoelectric effect. Adopted from [55]

Compton scattering

Compton scattering occurs when an incident photon interacts with an electron from the outer (M) shell. The photon collides with this electron and ejects it from the shell, creating a recoil electron (figure 2.7). This electron loses energy as heat or creates radiation, called bremsstrahlung. After the collision with the electron, the photon is scattered into a different direction. The angle of deflection is inversely proportional to the photon energy. The higher the photon energy, the smaller the angle of deflection.

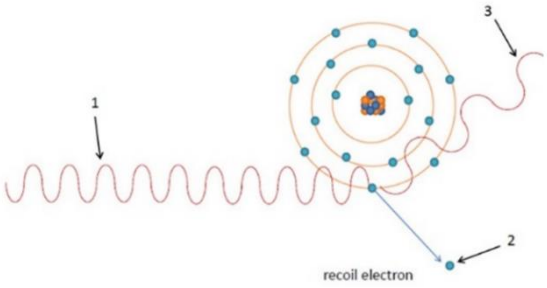

Figure 2.7 – Schematic drawing of Compton scattering. Adopted from [55].

Rayleigh scattering

Rayleigh scattering occurs at a low photon energy level (from around 10 keV). The incident photon interacts with an electron from the outer (M) shell, by transferring all its energy to the electron. The electron then releases this energy in the form of a photon, in a different direction from the original incident photon (figure 2.8). Because no energy is converted to kinetic energy or transferred to the material, the scattered wave has the same energy as the incident beam.

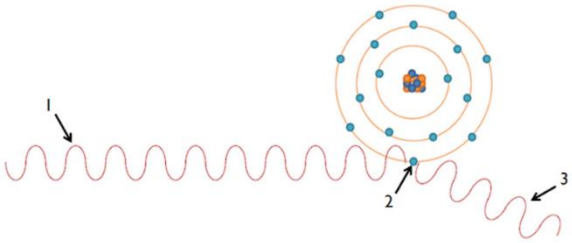

Figure 2.8 – Schematic drawing of Rayleigh scattering Adopted from [55].

2.3 THE LINEAR AND MASS ATTENUATION COEFFICIENT

One variable that is widely used for the quantification of attenuation characteristics is called the linear attenuation coefficient (μ). The linear attenuation coefficient (figure 2.9) describes the fraction of an x-ray beam that is being absorbed or scattered through a unit thickness of the material it passes through. Two important material properties that define the attenuation characteristics are the effective atomic number (Z), and the physical density of the material (ρ). The calculation of the linear attenuation coefficient is commonly performed by researchers using a computer program called XCOM, which was developed by the National Institute of Standards and Technology (NIST) [12]. The theoretical basis of this computer program is elaborated in the following section to provide better understanding how the material properties Z and ρ influence the attenuation characteristics. All following calculations involving the linear attenuation coefficient that are made in this thesis are based on XCOM and the theory behind the program.

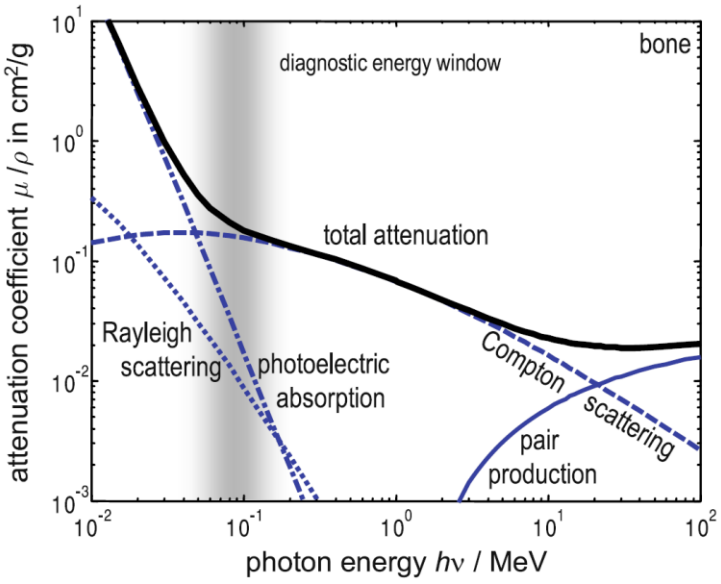

Figure 2.9 – The linear attenuation coefficient of bone tissue over a photon energy range of 0.01 to 100 MeV. The diagnostic range is shown in the gray area. Here it can be seen that Compton scattering dominates the attenuation process. For each different material, the dominating type of interaction can be different in the diagnostic energy range. Adopted from [1].

2.3.1 CALCULATION OF THE LINEAR ATTENUATION COEFFICIENT

When an incident x-ray beam passes through matter, the change of beam intensity can be expressed by equation 2.1. This equation is known as the law of Lambert-Beer [11].

$$I = I_0 e^{-\mu x} \tag{2.1}$$

In this equation I is the initial intensity, I_0 is the intensity after traveling through matter with a unit distance x. μ is the linear attenuation coefficient in $[cm^{-1}]$, which is further specified in equation 2.2.

$$\mu = N\sigma = \left(\frac{N_a \rho}{A}\right)\sigma \tag{2.2}$$

Where N is the density of the atom, which can be further specified as the number of Avogadro (N_a) times the physical density of the material (ρ) divided by the molecular weight of the material (A). σ is a proportional constant that represents the probability of a photon being absorbed or scattered (also called the cross section of a photon). For interactions in the diagnostic energy range, σ can be expressed by equation 2.3:

$$\sigma = \sigma_{pe} + \sigma_c + \sigma_r \tag{2.3}$$

Where σ_{pe} , σ_c and σ_r are the probability constant of the photoelectric absorption, Compton scattering and Rayleigh scattering respectively. In the lower diagnostic range, the probability constant are approximately proportional to the effective atomic number Z in the following way [10]:

$$\sigma \begin{cases} \sigma_{pe} \sim Z^4 \\ \sigma_c \sim Z \\ \sigma_r \sim Z^2 \end{cases} \tag{2.4}$$

2.3.2 CALCULATION OF THE MASS ATTENUATION COEFFICIENT

Because the linear attenuation coefficient depends on the density of a material or compound, researchers often report the mass attenuation coefficient (μ_m) in $[cm^2/g]$ for convenience. The mass attenuation coefficient is simply the linear attenuation coefficient which is divided by the density of the material or compound (equation 2.5).

$$\mu_m = \frac{\mu}{\rho} \tag{2.5}$$

2.4 ATTENUATION CHARACTERISTICS OF THE HUMAN HEAD

As explained in section 2.1.2, there are four tissue types in the human head that are clinically relevant for diagnostic imaging purposes: (1) *bone tissue*, (2) *brain tissue*, (3) *muscle tissue* and (4) *cerebrospinal fluid* (CSF)). These tissues all have a different chemical compositions. Because the chemical composition is different, the physical density (ρ) in [g/cm^3] and the effective atomic number (Z) are different too (although the differences are very small). This results in slightly different attenuation characteristics for each tissue type, which is why it is hard to differentiate these tissues on the CBCT system with the relatively low contrast ratio. The following section provides an overview of the chemical composition, physical density, effective atomic number and mass attenuation coefficient of these four tissue types.

2.4.1 CHEMICAL COMPOSITION

Human tissue is mainly composed (among other atoms) of the following atoms: H, C, N, and O (and Ca and P for bone) [13]. CSF is similar to water and contains very small fractions of constituents including ions, enzymes and other substances [14]. Therefore, CSF is further considered as pure water in terms of chemical composition in this thesis. The following table (table 2.1) shows the mass fraction of each atom that is present in a specific tissue type. Atoms that contribute significantly to the composition are highlighted in ***bold italic*** font.

Table 2.1 - Elemental mass fractions (%) of human tissues [13]. Numbers in bold Italian font indicate a significant contribution in the composition of the tissue. Adopted from [15].

Atomic number	Symbol	Bone	Muscle	Brain	Cerebrospinal fluid
1	H	***3.4***	***10.2***	***10.5***	***0.11***
6	C	***15.5***	***14.3***	***12.5***	0
7	N	***4.2***	***3.4***	***2.6***	0
8	O	***43.5***	***71***	***73.5***	***0.89***
11	Na	0.1	0.1	0.2	0
12	Mg	0.2	0	0	0
15	P	***10.3***	0.2	0.2	0
16	S	0.3	0.3	0.18	0
17	Cl	0	0.1	0.22	0
19	K	0	0.4	0.21	0
20	Ca	***22.5***	0	0.01	0
26	Fe	0	0	0,01	0
53	I	0	0	0.01	0

2.4.2 MASS ATTENUATION COEFFICIENT

The following table (table 2.2) is an overview of the mass attenuation coefficient of relevant human tissue types at different x-ray energy levels (60, 80, 100 and 150 [keV]). Furthermore, the physical density (ρ) and effective atomic (Z) number (at 100 keV) are given in this table.

Table 2.2 – The mass attenuation coefficient (μ/ρ) of human tissue (at different tube energies [keV]), the density (ρ) and effective atomic number (ℤ) of human tissue [12], [16][17]. Adopted from [15].

Human tissue	μ_{60}/ρ	μ_{80}/ρ	μ_{100}/ρ	μ_{150}/ρ	ρ	Z**(at 100 keV)**
Bone	0.3148	0.2229	0.1855	0.148	1.92	13.84
Muscle	0.2048	0.1823	0.1693	0.1492	1.05	7.65
Brain	0.2058	0.1831	0.1701	0.1498	1.05	7.74
Cerebrospinal fluid	0.2057	0.1827	0.1695	0.1492	1.00	7.68

3

DESIGN OF THE HEAD PHANTOM

3.1 INTRODUCTION

In a previously performed literature study [15] two types of head phantoms for IQA in (cone beam) CT were found: simple geometry (e.g. cylindrical, square) phantoms and anthropomorphic head phantoms. Because the simple geometry phantoms cannot be used for clinically relevant (qualitative) IQA due to the shape of the phantom (specifically when taking scatter radiation into account), they were disregarded for further evaluation. The anthropomorphic head phantoms (referred to as phantoms from now on) in the commercial and academic setting were evaluated for their attenuation characteristics and features for quantitative IQA (see figure 3.1 for an overview of the evaluated phantoms). A detailed description of the phantoms from this overview can be found in appendix A.

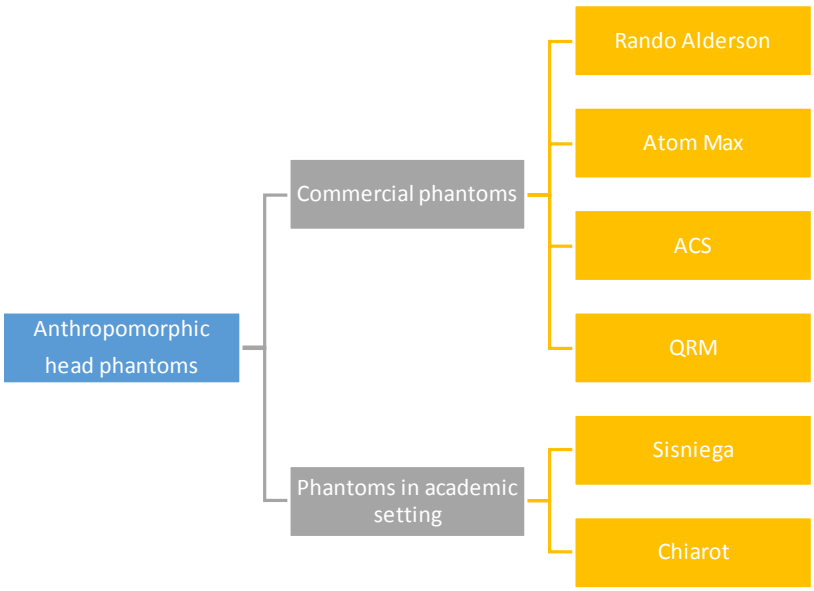

Figure 3.1 – Overview of anthropomorphic phantoms for image quality assessment in (cone beam) CT. Adopted from [15]

From the results of the literature study, several remarkable drawbacks of these phantoms were found. Commercial phantoms appear to be composed of materials that are not representative in terms of attenuation characteristics in the low diagnostic x-ray energy range [18], [19]. These phantoms also often lack inserts for quantitative image quality assessment [20]–[22] (figure 3.2a), while in many cases this is a desired feature among researchers. Nevertheless these phantoms are still often used due to the lack of better alternatives [23]. Some researchers have introduced alternatives for the commercial phantoms which contain low contrast inserts for quantitative IQA (figure 3.2b and c), but the evaluation of the phantoms show that the attenuation properties of the materials that were selected for the construction of these phantoms are often still not representative in the lower diagnostic energy range [19]. Furthermore, none of these phantoms have been evaluated specifically for their scatter characteristics, while scatter is an important factor in the attenuation characteristics of a material. An overview summarizing the findings of the evaluated phantoms is presented in table 3.1.

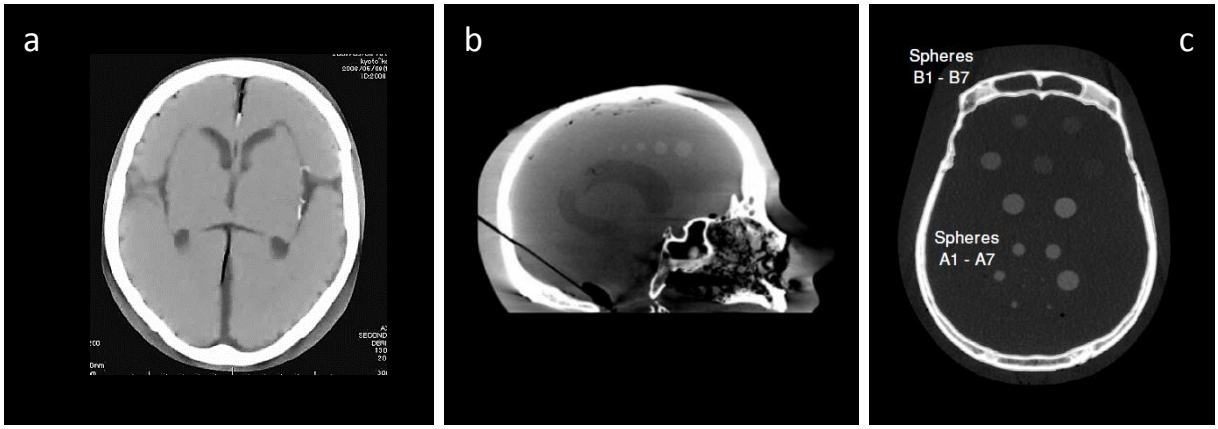

Figure 3.2 – Examples of anthropomorphic head phantoms that are used for (quantitative)image quality assessment in (cone beam) CT. A) ACS head phantom (Kyoto Kagaku, Kyoto, Japan) b) modified Rando-Alderson phantom by [25] *(RSD phantoms, Long beach, CA 90810, USA) c) Newly developed phantom using RSD materials* [19].

Table 3.1 – Attenuation characteristics and features quantitative image quality assessment of anthropomorphic head phantoms. Adopted from [15].

Commercial phantom	Realistic attenuation	Inserts for IQA	Remarks	Source
Rando-Alderson by RSD	No	Step wedge and line pair pattern	Underattenuation under 90 keV Inserts not suitable for CT reconstruction	[18], [21]
Atom Max by CIRS	Yes	no	Features for dental CBCT	[20]
ACS by Kyoto Kagaku	Yes	no	Contrast medium filled arteries	[22]
Semi-anthropomorphic phantom by QRM	Not specified	Optional	No muscle/soft tissue	[24]
Phantom in academic setting	**Realistic attenuation**	**Inserts for IQA**	**Remarks**	
Sisniega	Not specified	Low contrast inserts	Modified Rando-Alderson Image artifacts due to opening in head	[25]
Chiarot	No	Low contrast inserts	Full body phantom Rando-Alderson material with too low attenuation	[19]

3.2 DESIGN CRITERIA

Based on findings from the literature study, the design of the phantom should at least satisfy the following criteria:

- Realistically resemble the anatomy of the human head for qualitative IQA
- Contain inserts for quantitative IQA of the contrast and spatial resolution
- Use materials with similar attenuation (in terms of both absorption and scatter) properties as relevant tissues in the human head

Additionally, the desire was to use materials that are suitable for simple fabrication techniques such as simple casting and 3D printing, in order to make 'home made' fabrication of the phantom possible. This way, researchers can have a better accessibility to cost-efficient and customized phantoms, by designing and fabricating the phantom themselves.

3.3 CBCT-DATA BASED DESIGN

3.3.1 CREATING MESH MODELS USING MANUAL SEGMENTATION OF CBCT DATA

The basic design of the phantom was based on anatomical data (DICOM format) from a head XperCT of an anonymous male patient, which was acquired using the head XperCT protocol on a Philips Allura FD20 (Philips Healthcare, Best, the Netherlands). The DICOM data were manually segmented by setting a threshold for a soft tissue shell and for the skull (figure 3.3a and b). The soft tissue shell was segmented using a low threshold (HU: -460) and the skull was segmented using a high threshold (HU: 463). The segmented models were converted into an .STL mesh using a CT-volume processing tool (AixiaViewer, D. Ruijters, Philips Healthcare, Best, the Netherlands).

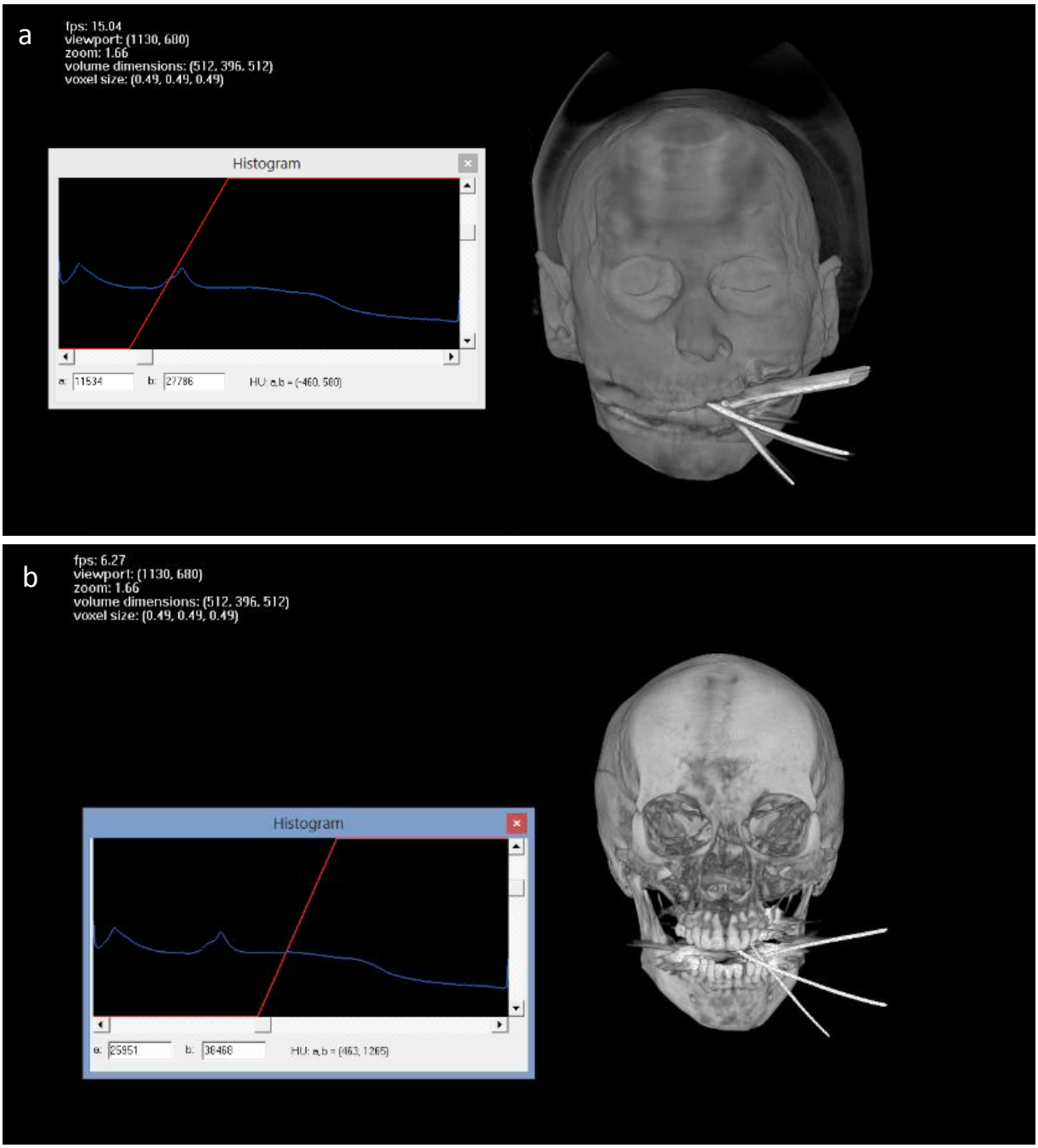

Figure 3.3 – Examples of manually segmented patient cone beam CT data by adjusting the threshold of the image. The images can be saved as .STL mesh file, using AixiaViewer. a) Segmented muscle shell. b) segmented skull.

In the first of the two design iterations, where nylon was selected as brain equivalent material based on the theory from the literature study (see chapter 4), a 3D mesh of the brain was needed. However, the mesh of the brain could not be obtained using the manual segmentation technique. Because the HU values of muscle tissue and brain tissue are very similar, brain tissue could not be made separately visible for the creation of the mesh file (figure 3.4). The mesh of the brain was therefore created using an inverse shrinkwrap technique in Blender (Blender, Amsterdam, the Netherlands), which is an open source program for editing and creating mesh-based 3D models. The methodology of the processing of the obtained meshes from AixiaViewer are explained in the following section of this chapter.

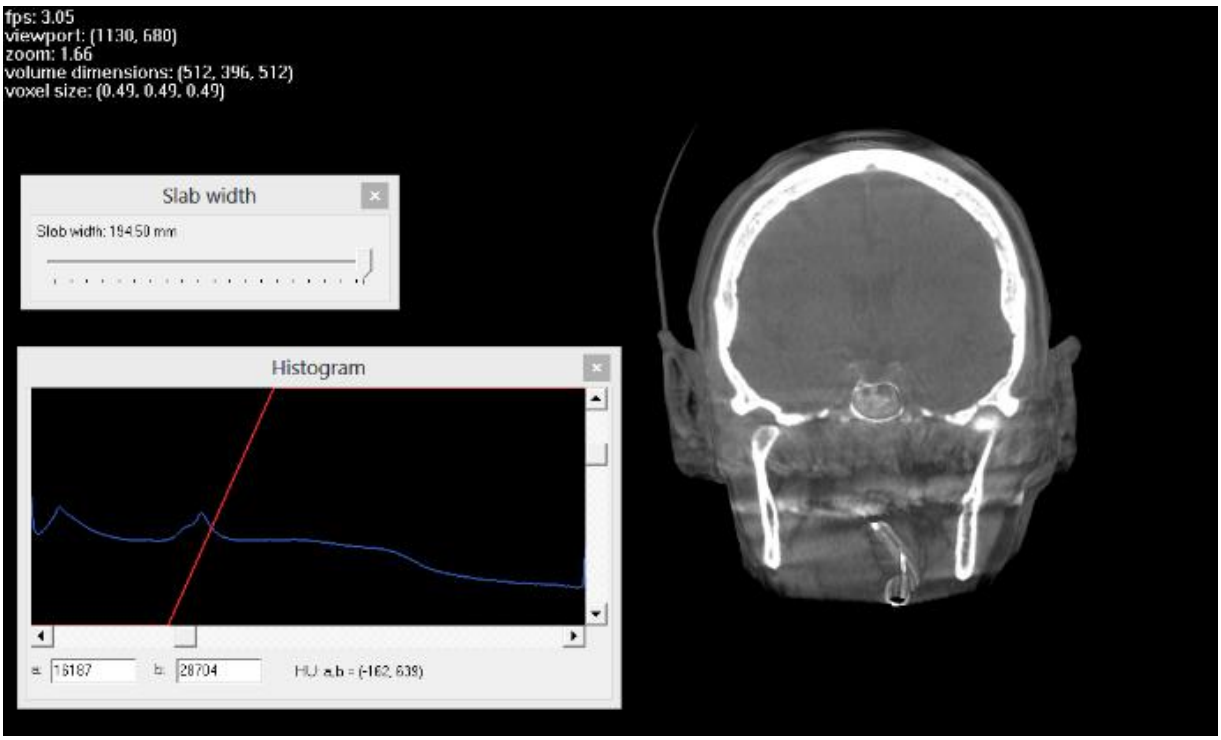

Figure 3.4 – Cross section of patient CBCT data made in AixiaViewer. As can be seen, brain tissue could not be segmented from these data because the radiodensity of brain tissue is similar or lower than the radiodensity of muscle or bone tissue. (Manual segmentation is only possible for tissues with a higher radiodensity.)

3.3.2 MESH PROCESSING USING BLENDER

The editing of the mesh files consisted of several steps (figure 3.5). In the first step, the mesh data were cleaned up by removing loose vertices and unwanted artifacts such as the head support and tubing in the patients mouth. After this step, the (damaged) mesh files were repaired, by closing up big open vertices and big holes. Afterwards, a shrinkwrap operation was performed, in order to create a smooth copy of the original mesh without damages in the mesh. Where necessary, manual adjustments were made in the new shrinkwrap mesh and finally the mesh was made manifold, which is required for 3D printing. From this process, the shrinkwrap operation and manual adjustments are explained in more detail.

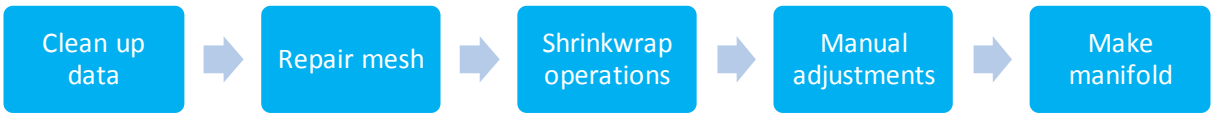

Figure 3.5 – Schematic overview of the processing of the mesh files using Blender (Blender, Amsterdam, the Netherlands).

Shrinkwrap operation and brain design

The shrinkwrap process is a feature of blender that allows a new mesh to be created around an existing mesh and hereby, the new mesh is wrapped tightly around the existing mesh (just like a shrinkwrap). The tightness (and in this case also the similarity of the form) of the wrap with respect to the existing mesh depends on the number of iterations that are performed and the offset of the shrinkwrap can be chosen. Because the mesh of the brain could not be obtained using the manual segmentation technique within AixiaViewer, an inverse shrinkwrap operation was performed within the cranial cavity of the skull mesh (figure 3.6).

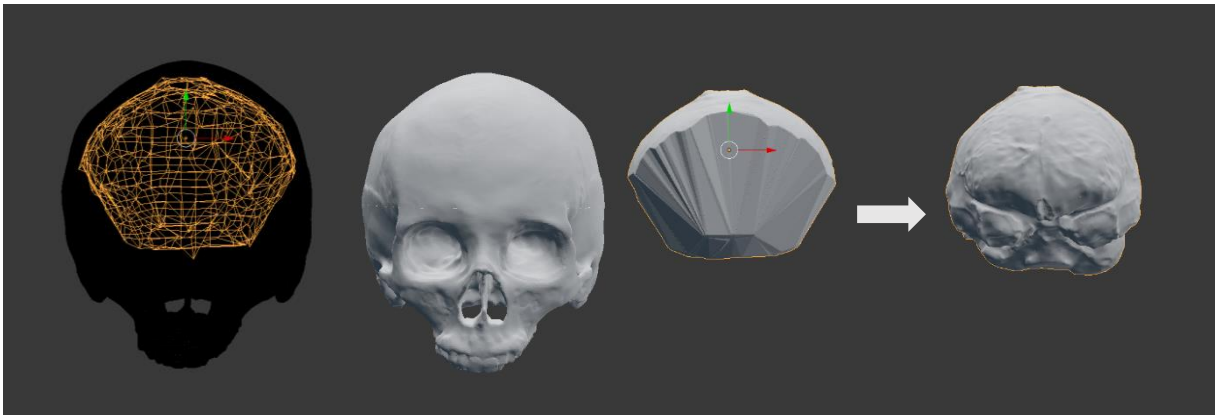

Figure 3.6 – Example of the application of a shrinkwrap operation within the cranial cavity in order to create a mesh of the brain.

By following these steps, a solid mesh of the brain could be created which fits exactly within the cranial cavity (with a 0.5 mm offset tolerance). A mesh of the ventricles, which contains the CSF was obtained from an open source website for medical 3D models [26] and manually positioned at the right location within the brain. Cavities for (low) contrast resolution inserts were created axially at the posterior area of the brain. By performing a Boolean operation (merging) afterwards between the brain mesh ventricle mesh and insert cavities, an final model of the brain could be created (figure 3.7).

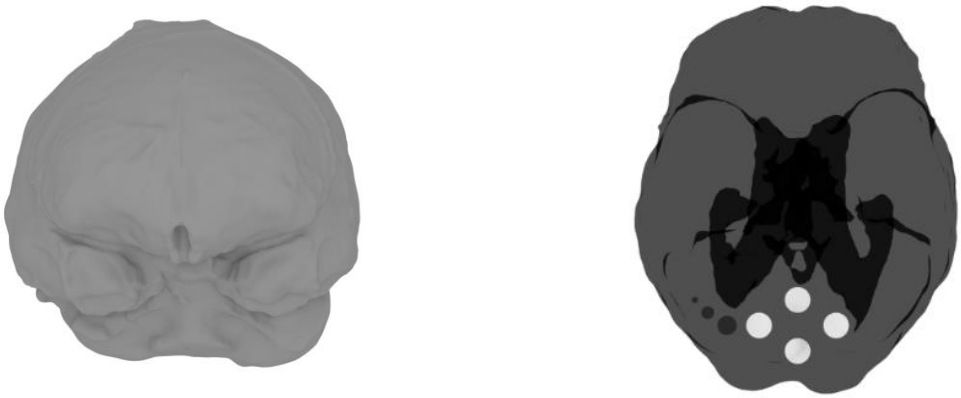

Figure 3.7 –Left: anterior-posterior view of the final mesh of the brain model, which was needed in the first design iteration. Right: axial superior inferior view of the brain mesh where inserts are positioned axially at the posterior area of the brain and the ventricles, containing cerebrospinal fluid are also incorporated into the design of the brain.

Skull design and manual adjustments

The mesh file of the skull that was obtained using AixiaViewer contained many open structures in the maxillofacial area (figure 3.8a). These structures are potentially too weak or too complex for fabrication using simple casting or rapid prototyping techniques. By applying the shrinkwrap operation over the original skull mesh (after dividing the skull in three parts (calvaria, maxillofacial area and mandible) using Autodesk's Netfabb program for manipulating 3D meshes (Autodesk, San Rafael, CA,

USA)), most of the holes were closed and a smooth mesh could be created (figure 3.8b) (the ocular and nasal cavity were manually created). However, there are several air filled cavities within the skull, including the maxillary sinus, ethmoid sinus and sphenoid sinus (figure 3.9a). By taking into account the fabrication methods that will used for the fabrication of the skull (simple casting and rapid prototyping), the decision was made to disregard the closed cavities within the skull from the design, which are the maxillary sinus, the ethmoid sinus, and the sphenoid sinus (because simple casting and selective laser sintering are not suitable for the fabrication of objects with closed holes). The frontal sinus cavity was included in the design because the cut between the calvaria and the maxillary region was made exactly through the frontal sinus cavity (and thus the frontal sinus is not a closed cavity anymore within this design) (figure 3.9b).

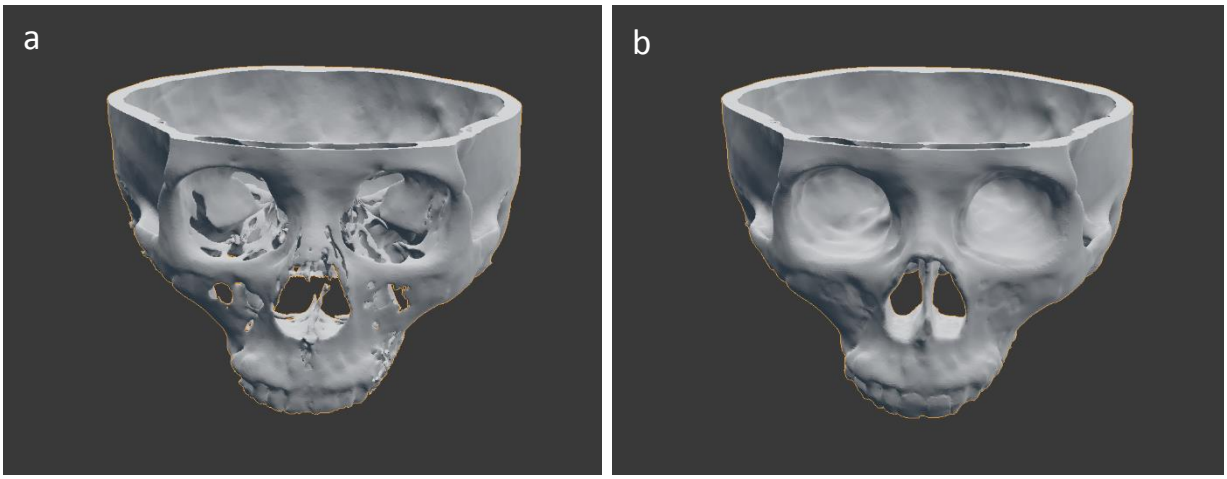

Figure 3.8 – Mesh model of the maxillofacial area of the skull. A) Before applying the shrinkwrap operation and manual adjustments. B) After applying the shrinkwrap operation and manual adjustments. The orbits (ocular cavities) and nasal cavities were created using the sculpting tool within Blender.

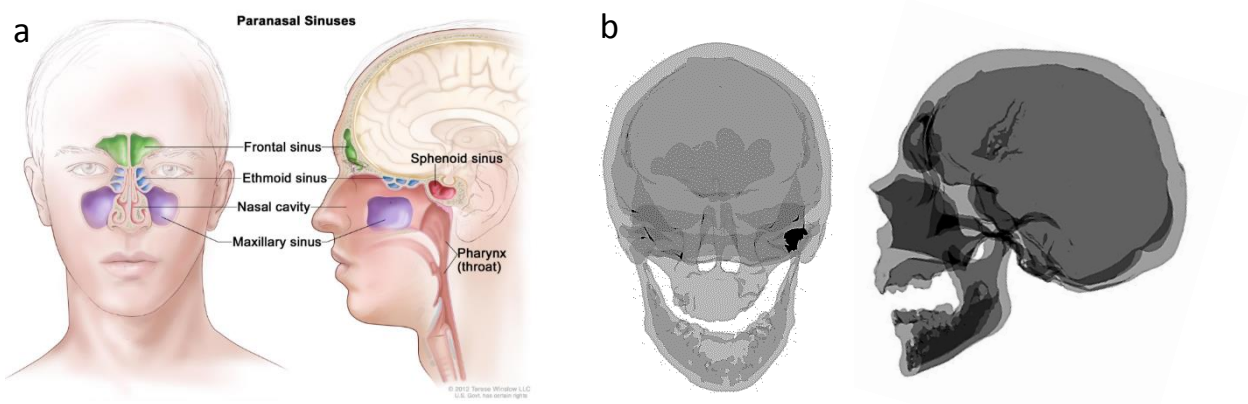

Figure 3.9 – a) Natural air filled cavities within the human skull [56]*. B) Incorporated natural cavities (dark grey areas) within the design of the phantom. Included cavities are the frontal sinus, orbits (ocular cavities), the nasal and oral cavity. Excluded cavities are the maxillary sinus, the ethmoid sinus, and the sphenoid sinus.*

Insert design

Within the cranial cavity, the ventricles and inserts for the measurement of the (low) contrast and spatial resolution are incorporated. In the first design iteration, holes for the ventricle and inserts were created with a Boolean operation between the mesh of the brain and the ventricle/inserts. Because later an SMP gel was selected as brain equivalent material, this configuration could not be achieved anymore. Therefore the skull was used as a support for the ventricle and insert, by making holes in the inner surface of the cranial cavity, in which the ventricle and inserts can be clamped (figure 3.10). The selected inserts have diameters varying from 1 to 10 mm , with a length of approximately 40mm (+- 5

mm), depending on the maximal height of the cranial cavity at the position of the insert. In total, 10 inserts for low contrast resolution are incorporated in the design, with two different levels of attenuation (5 inserts per attenuation level). 1 insert for spatial resolution (QRM micro-insert, Moehrendorf, Germany) and a ventricle are incorporated into the design as well.

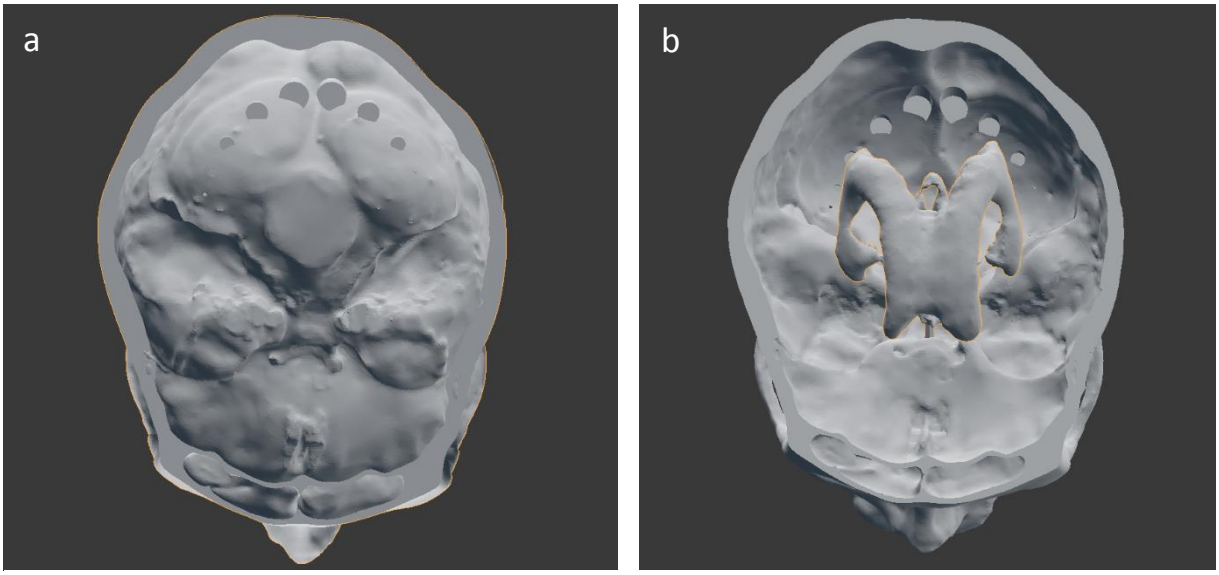

Figure 3.10 – Insert design and placement. Cutouts are made at the posterior side of the skull where the (low) contrast resolution inserts can be positioned. A cutout is made at the 'sella turcica' where the ventricles can be inserted into. A large cylindrical cutout is made at the anterior side of the skull where the insert for spatial resolution can be positioned.

3.4 FINAL DESIGN

In the final design (after the second design iteration), the mesh of the brain was disregarded, because a silyl modified polymer (SMP) gel would be used as brain substitute. The soft tissue shell is vertically split into two parts (figure 3.11a) and the skull is split into three separate parts: the calvaria, the maxillofacial area and the mandible (figure 3.11b). Within the cranial cavity of the brain, holes were created in the axial direction to lock in the ventricle and the inserts for low contrast resolution measurement (figure 3.10c). The specifications of the design are summarized in table 3.2.

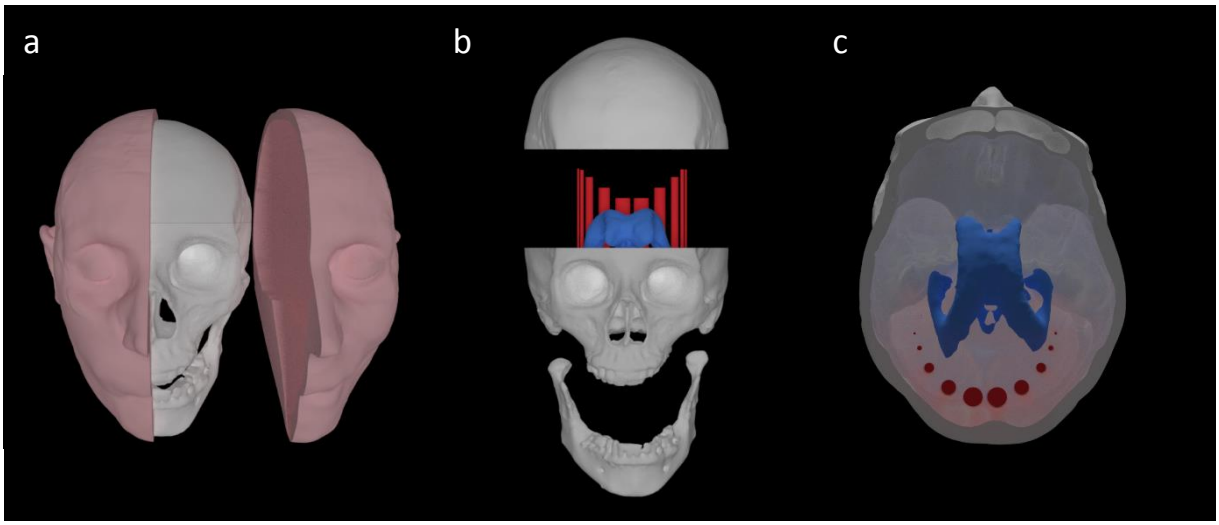

Figure 3.11 – Final design of the head phantom. A) Outer muscle shell B) Anterior-posterior view of the calvaria, maxillofacial area and mandible skull, with inserts C) Axial superior-inferior view of the insert and ventricle positions.

Table 3.2 – Specifications of the head phantom

Part	Features	Dimensions (roughly)	Remarks
Outer muscle shell	2 parts enclosure	180x140x180 (LxWxH)	Vertically cut
Skull	3 Parts Natural cavities Holes for inserts	180x140x180 (LxWxH)	Closed natural cavities not included Manual adjustments in the anatomy
Brain	Low contrast ventricles with CSF	150x125x120 (LxWxH)	No actual 3D computer model for second design iteration
Inserts	10x low contrast resolution (1x spatial resolution)[2]	D = 10, 5, 2.5 and 1.25 mm L = 40 mm (roughly)	

3.5 DISCUSSION AND CONCLUSIONS

During the design of the head phantom, several anatomical features of the human head were simplified or manually adjusted. Closed cranial cavities, including the maxillary sinus, ethmoid sinus and sphenoid sinus were excluded in this design, because these cavities cannot be fabricated using simple casting or rapid prototyping techniques. The structural integrity of maxillofacial area was also manually adjusted, because in the original mesh, this are contained many open structures which were likely to be too weak for fabrication (and is therefore also not sufficiently durable for normal usage). It is expected that the changes to the anatomy will have slight influence on the scatter characteristics of the phantom, because scatter is also geometry dependent. Especially the maxillary sinuses are relatively big and therefore, this area might lead to more scatter radiation compared to a real head in this area.

Overall, a head model could be created which is composed of different tissue layers with a high resemblance to the original anatomy of a male head. The scatter characteristics of such a phantom are therefore likely to be much more representative, compared to simple geometry phantoms for quantitative IQA. Also this current design offers the possibility for quantitative IQA by adding inserts for quantitative measurement of the (low) contrast and spatial resolution in the area of the brain, which is a major advantage compared to many commercial phantoms which do not have this option. Furthermore, because this design can be completely manufactured using simple casting and rapid prototyping techniques, wide adoption from users in both an academic or business related setting is possible (only the computer models of the design and access to these fabrication techniques are needed).

[2] The spatial resolution inserts can be commercially bought and are an option for future design, but in this design spatial resolution inserts were not included due to the high costs of commercial inserts.

4

SELECTION OF TISSUE EQUIVALENT MATERIALS

4.1 INTRODUCTION

TEMs that are used for phantoms should be carefully selected. In terms of attenuation characteristics, the material should have similar absorption and scatter characteristics compared to the tissue they resemble in the diagnostic energy range. In terms of mechanical properties, the material should have sufficient strength and toughness in order to sustain the impact forces that can occur during transportation and usage. For this specific project, the material should also be suitable for fabrication methods that are selected for this project, which are simple casting and rapid prototyping techniques such as fused deposition modeling (FDM) and selective laser sintering (SLS). This chapter provides an overview of TEMs that are recommended in the literature and TEMs that are potentially suitable for this project are selected for further research.

4.2 TISSUE EQUIVALENT MATERIALS IN THE LITERATURE

In a previously performed literature study, an overview of bone equivalent materials and muscle/brain equivalent materials for x-ray imaging and dosimetry was made. The following figures are an overview of bone equivalent materials (figure 4.1) and muscle/brain equivalent materials (figure 4.2) that are commonly used in a commercial setting and TEMs that were recommended in the literature.

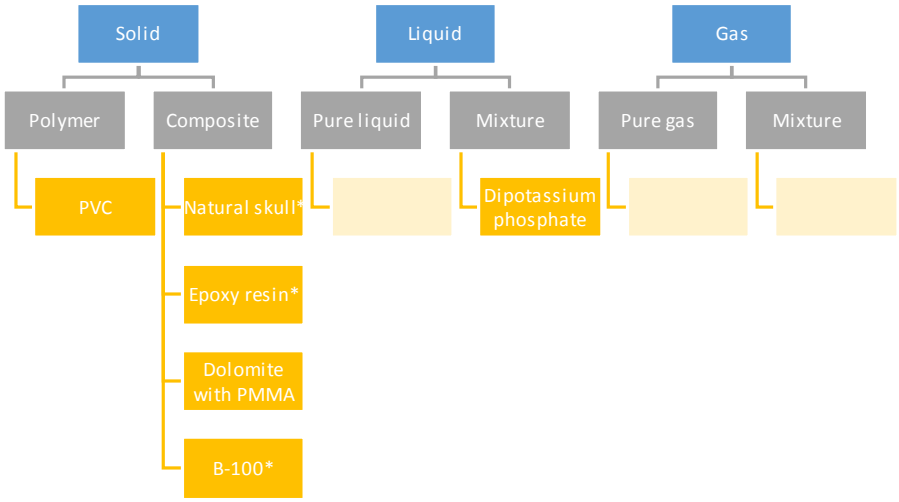

Figure 4.1 – Overview of bone equivalent materials that are commercially used (indicated with a '' sign) and bone equivalent materials that were recommended in the literature. Adopted from* [15].

TEMs that are commercially used include natural bone [21] and bone equivalent plastic (called B-100) [27]. Bone equivalent materials that are reported in the literature include polymers such as polyvinylchloride [27] and polycarbonate [28] or are mainly composed of a mix of minerals and a constituent, for example dolomite with PMMA [29] or dipotassium phosphate-water solution [30].

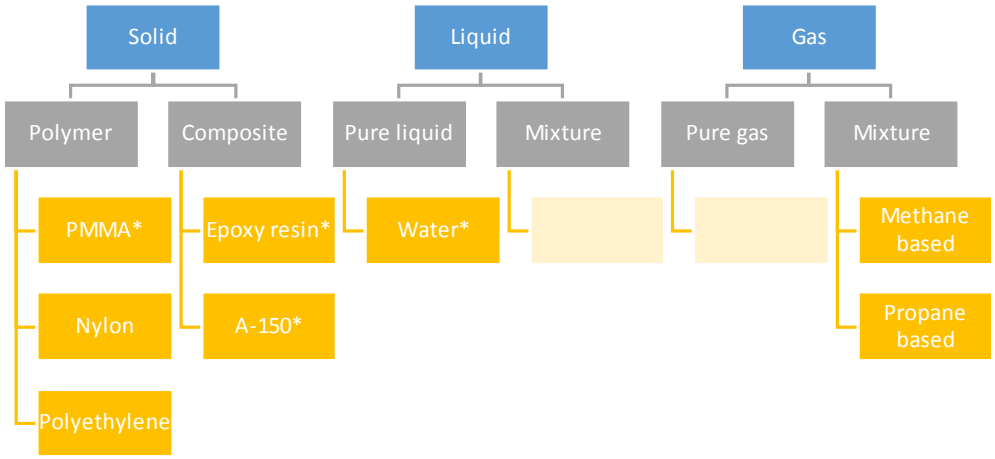

Figure 4.2 – Overview of muscle or brain equivalent materials that are commercially used (indicated with a '' sign) and muscle or brain equivalent materials that were recommended in the literature. Adopted from* [15].

Commercial TEMs that are commonly used for simulating muscle or brain tissue include epoxy-resin based materials [31], PMMA [32], [33] and water [33]. TEMs that are reported in the literature include polymers such as nylon [13], [34] and polyethylene [27], [35], but also composite materials such as epoxy resins [23], [31], waxes, modelling clay, bolus and pitch [13], [33]. Representative materials in terms of mass attenuation were the further evaluated in terms of durability and suitability for the selected fabrication methods [15].

Based on the evaluation of the materials in terms of mass attenuation coefficient, durability (strength and toughness) and suitability for the selected fabrication methods, many TEMS turned out to be not very suitable (table 4.1). In fact, no suitable bone equivalent material was found within the materials from the literature study. As muscle/brain equivalent material, nylon was the best option. (Nylon has the best overall mass attenuation coefficient compared to the alternatives, is sufficiently durable and is suitable for laser sintering). For this reason, an alternative approach was used to find suitable bone equivalent materials. This methodology is further described in section 4.3 in this chapter.

Table 4.1 – Overview of excluded tissue equivalent materials that are not suitable for this specific project.

Excluded TEM	Reason for exclusion	Source
Bone equivalent material		
PVC	Not suitable for selected fabrication methods (toxic when heated)	
Natural skull	Underattenuation , not suitable for selected fabrication methods	[23]
Epoxy resin	Underattenuation, unknown composition	[31]
Dolomite with PMMA resin	Not suitable for selected fabrication methods	
B-100	Not suitable for selected fabrication methods	
Dipotassium phosphate	Not suitable for selected fabrication methods	
Muscle/brain equivalent material		
PMMA	Underattenuation	[36]
Polyethylene	Underattenuation (60-80 keV) overattenuation (80-150 keV)	[35], [37]
A-150	Not suitable for selected fabrication methods	

4.3 CALCIUM RICH BONE EQUIVALENT MATERIALS

Because the bone equivalent materials from the literature study did not satisfy all inclusion criteria for this project (most bone equivalent materials were not suitable for the selected fabrication methods), an alternative approach was used to find a suitable material. Since some studies show that mineral rich materials can have a similar chemical composition compared to bone tissue [29], [30], these types of materials were further investigated. Several studies in the field of (bone) regenerative medicine have shown that some calcium rich materials which can be used as scaffolds, including calcium phosphates (figure 4.3a and b), are suitable for rapid prototyping techniques and can potentially serve as bone equivalent material if the attenuation characteristics are representative. Therefore, these materials were evaluated for their mass attenuation coefficient. Figure 4.4 is an overview the mass attenuation coefficient of the investigated calcium rich materials with representative mass attenuation coefficient, which were determined using XCOM.

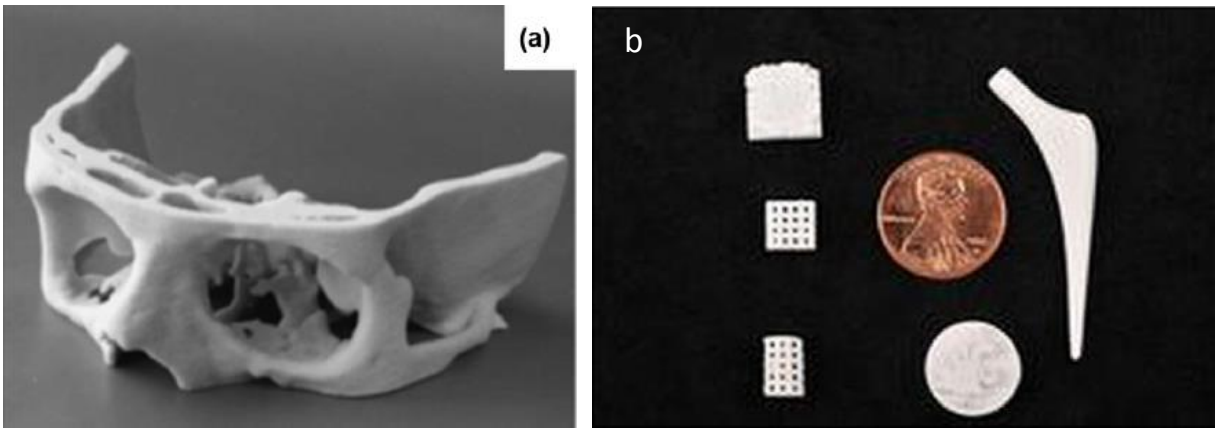

Figure 4.3 – Examples of bone structures that were 3D printed (using selective laser sintering techniques)from calcium rich materials. A) A part of a maxillofacial are. B) small scaffolds and a model of a hip implant. [57]

4.3.1 MASS ATTENUATION COEFFICIENT

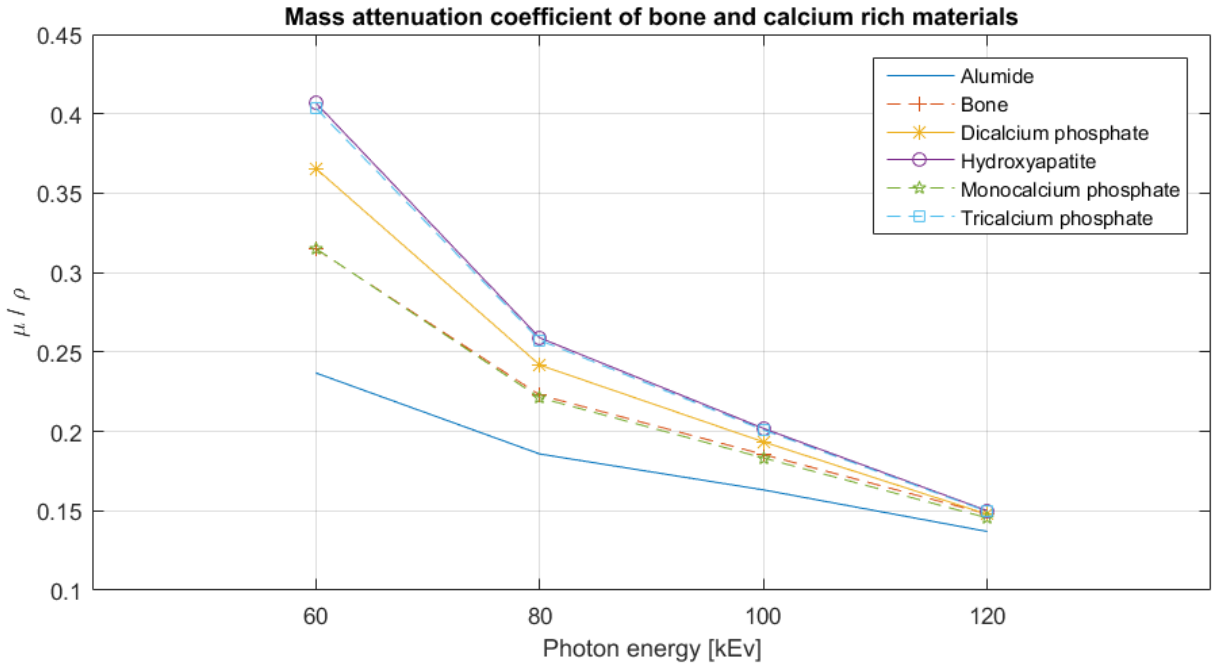

Figure 4.4 – Mass attenuation coefficient of calcium rich materials. Data obtained from [12].

It can be seen from figure 4.4 that monocalcium phosphate has a mass attenuation coefficient which is in theory very similar to bone tissue.

4.3.2 MECHANICAL PROPERTIES

Because the mechanical properties of the calcium rich can affect the durability of the phantom, these were also evaluated using measurements of the yield strength and fracture toughness found in the literature. In a recent study by Inzana et al [38], the mechanical strength of these calcium rich materials after sintering were evaluated. The results of this study are listed in table 4.2.

Table 4.2 – Mechanical properties, specified in the yield strength (σ_y) in [MPa] and stress intensity factor ($K_{1,c}$) in [MPa^1/2] of calcium rich materials [38].

Material	$\boldsymbol{\sigma_{y,min}}$	$\boldsymbol{\sigma_{y,max}}$	$\boldsymbol{K_{1,c\ min}}$	$\boldsymbol{K_{1,c\ max}}$
Hydroxyapatite	16	45	0.51	0.96
Calcium phosphates	33	50	1.27	1.62
Alumina	150	600	2.6	6

As can be seen from table 4.2, all materials have respectable strength and toughness, based on a comparison to commercial TEMs that were evaluated in the previously performed literature study [15]. However, the authors have shown that the sintering temperature and exposure to water have influence on the mechanical properties of the material. So while these results provide a rough indication about the durability of the materials, the actual durability of the material should still be tested. Thorough testing of the mechanical properties of these materials is however outside the scope of this project.

4.4 INCLUDED MATERIALS FOR FURTHER RESEARCH

In the design process of the phantom, two iterations were needed before reaching satifying results, because of differences between measured and theoretical radiodensity values of certain materials (see chapter 5) and because of some unforseen circumstances regarding the avaliability of fabrication resources for 3D (SLS) printing of some selected TEMs. The following section provide a general description of the materials that were included in the two iterations. Furthermore, because PMMA is a widely used material for the construction of phantoms, it is also included for further research as a reference to compare to.

4.4.1 MATERIALS FROM THE FIRST ITERATION

Based on the literature study and based on the evaluation of the calcium-rich materials, monocalcium phosphate (MCPH) and nylon were included as bone and muscle/nylon equivalent material respectively in the first design iteration for further research.

Monocalcium phosphate as bone equivalent material

Monocalcium phosphate (MCPH) (also known as calcium dihydrogen phosphate) is one of the three naturally occurring calcium phosphate minerals with the chemical formula $Ca(H_2PO_4)_2$. MCPH is commonly used as food additive in the agricultural industry. MCPH is commercially available in powder form, with powder granules ranging from several microns to several millimeters in diameter. The production of MCPH is done by reacting phosphate rock or calcium hydroxide with a phosphoric acid (equation 4.1).

$$Ca(OH)_2 + 2\ H_3PO_4 \rightarrow Ca(H_2PO_4)_2 + 2\ H_2O \qquad (4.1)$$

MCPH is partially soluble in water, but after evaporation of excess water it turns in a hard substance with some mechanical strength.

Nylon as muscle and brain equivalent material

Nylon (also known as polyamide) is a versatile group of synthetic materials that has many applications, which includes the textile industry, for packaging and for the fabrication of machine parts. From this group of polymers, nylon 12 (or polyamide 12) is suitable for fabrication using SLS. Nylon 12 consists of acid amide groups with 12 carbons in the monomer unit (hence the name). Nylon 12 can be produced in two ways, the first one being the polycondensation of ω-aminolauric acid with an amine and an carboxylic acid group (equation 4.2).

$$n\ H_2N(CH_2)_{11}CO_2H \rightarrow [(CH_2)_{11}CONH]_n + n\ H_2O \qquad (4.2)$$

The second way is through ring-opening polymerization of laurolactam (equation 4.3) at high temperatures (typically between 260 and 300 ℃). This way is the preferred way in the industry because the end product is more stable [39].

$$n\ [(CH_2)_{11}CONH] \rightarrow [(CH_2)_{11}CONH]_n \qquad (4.3)$$

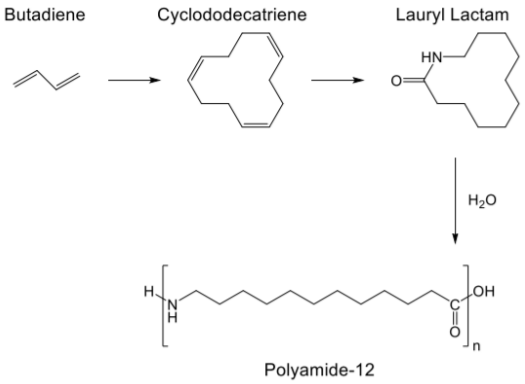

Figure 4.5 – Ring opening polymerization process for the fabrication of nylon 12. Adopted from [39].

4.4.2 MATERIALS FROM THE SECOND ITERATION

Because nylon showed an underattenuation (chapter 5) compared to brain tissue and there were several other practical drawbacks, including the presence of air in the 3D printed model of the brain, a gel-based polymer (silyl modified polymer) was eventually chosen as brain equivalent material. Because selective laser sintering was not available anymore for monocalcium phosphate, several constituent materials were investigated to make the fabrication of a MCPH mixture possible, while remaining the desired x-ray imaging characteristics

Monocalcium phosphate with gypsum mixture as bone equivalent material

As a slight variation on the MCPH powder that was initially intended for SLS fabrication, a calcium phosphate-gypsum mixture was investigated, based on calculation of the theoretical mass coefficient for the mass fractions of each constituent in the mixture (using XCOM). The ideal mixture consists of 3.85 wt% MCPH, 60 wt% calcium sulfate and 36.15 wt% water. After hardening of the MCPH and gypsum-water mixture (MCPHG), a stable solid material with what appeared to have high mechanical strength and toughness remained. During the hardening process, air bubbles appeared, presumably caused by a chemical reaction with the MCPH. After leaving the substance for approximately two hours, with constant stirring in between, most of the air bubbles could be removed.

The exact chemical reaction between the MCPH, gypsum and water is unknown, but thorough investigation of this chemical reaction is beyond the scope of the project. However, based on observations during the hardening process of the material, an assumption was made that all MCPH powder and gypsum reacted with the water molecules and that the remaining water evaporated during this process. After several days, no further reactions were observed, except for a slight change of color (from grey to white) due to evaporation of the excess water. The stable end result of this material after hardening was eventually investigated in terms of attenuation characteristics.

Silyl modified polymer as brain equivalent material

Silyl modified polymers (SMP) are gel-like adhesives that uses an organic solvent to dissolve a polymer that will act stick to a surface. SMPs are commercially available and are used as sealant or filler. The production of SMPs is achieved by bonding polymers containing a silicon to oxygen. SMPs set by hydrolysis of water, forming cross linkages between the polymer chains (equation 4.4). After setting, the mechanical properties of SMPs are highly elastic and the material also becomes inert.

$$2RSi(OCH_3)_2R' + H_2O \rightarrow [RSi(OCH_3)R']_2O + 2CH_3OH \quad (4.4)$$

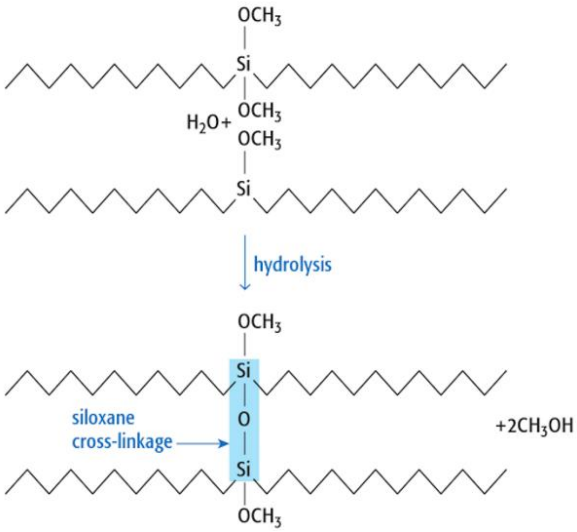

Figure 4.6 – Siloxane cross-linking between polymer chains through hydrolysis. Adopted from [58].

The exact materials that were used and the important material properties (chemical formula, mass attenuation coefficient (μ_m) and physical density (ρ)) of the included materials are summarized in table 4.3.

Polymethylmethacrylate as brain equivalent material

PMMA, also known as Perspex, Plexiglas or acrylic is a widely used material for the construction of phantoms for IQA in CT or CBCT. PMMA is a transparent thermoplastic which can be produced by different types of polymerization processes, including bulk or emulsion polymerization [40].

Table 4.3 – Overview of the material characteristics of the included tissue equivalent materials: the chemical formula, mass attenuation coefficient (μ_m) and physical density (ρ).

Included TEM and source	Chemical formula	$\mu_{m,60}$	$\mu_{m,80}$	$\mu_{m,100}$	$\mu_{m,150}$	ρ
MCPH (de bron B.V.)	$Ca(H_2PO_4)_2$	0.315	0.221	0.183	0.146	2.22
Nylon 12 (Shapeways 'strong and flexible plastic')	$(C_{12}H_{23}NO)_n$	0.195	0.179	0.169	0.150	1.01
SMP (Bison polymax crystal)	$[RSi(OCH_3)R']_2$	0.248	0.196	0.173	0.145	1.04
MCPHG (de Bron B.V. and Krone 'modelgips')	Unknown	0.314	0.223	0.187	0.149	2.3
PMMA	$(C_5O_2H8)_n$	0.192	0.175	0.164	0.146	1.18

5

RADIODENSITY OF THE TEMS

5.1 INTRODUCTION

In chapter 4, the mass attenuation coefficient (μ_m) and the physical density (ρ) of the TEMs were determined over the diagnostic energy range between 60 and 150 keV. With these two variables known, the radiodensity of a material can be calculated in Hounsfield Units (HU), which is a linear scale of grey values of voxels (pixels with the thickness of a single slice in the 3D volume). The HU value can be calculated using equation 5.1.

$$HU = 1000 * \frac{\mu_x - \mu_{water}}{\mu_{water}} \quad (5.1)$$

Where μ_x is the *linear* attenuation coefficient of the material and μ_{water} is the linear attenuation coefficient for water a specific photon energy (typically at 120 keV for XperCT).

It is of clinical importance that the HU values of the phantom are within the range of HU values for each specific tissue type, because in a clinical assessment, these HU values are used by the physician to differentiate for example a benign tumor from a malignant one. For adequate quantitative IQA, the HU values of the phantom must also fall between this range. This is especially of importance for an unbiased quantification of the contrast resolution of the image. The methodology and results of the HU measurements are explained in the following sections of this chapter, followed with a discussion and conclusions about the representativeness of the selected TEMS, which are compared with human tissue, in terms of radiodensity.

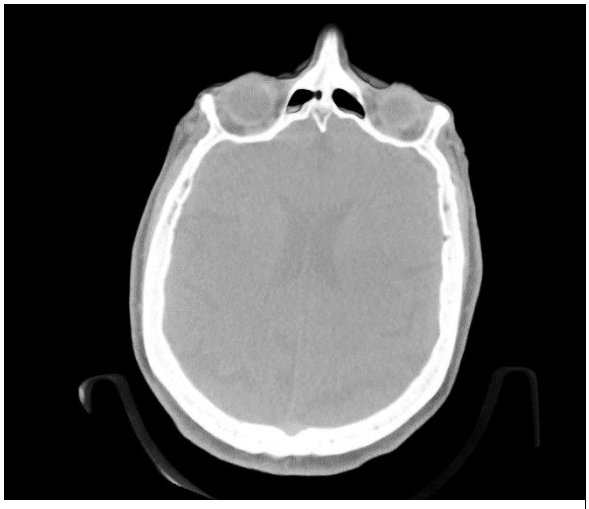

Figure 5.1 - Axial view (from below) of a patients head where different tissue types are visualized in different Hounsfield Units (grey values).

Typical HU values of relevant tissue types in the head (figure 5.1) are listed in table 5.1.

Table 5.1 – Typical HU values of human tissues and theoretical HU values of the TEMs.

Tissue type/TEM	Lowest HU value	Highest HU value
Bone	700	3000
Muscle	10	40
Brain	20	45
Cerebrospinal fluid	5	15

5.2 METHODS AND MATERIALS

5.2.1 MATERIAL SAMPLES AND EXPERIMENTAL DESIGN

The HU values were measured for the four TEMs that were included for further investigation in this project (MCPH (grains), nylon, SMP and MCPHG) and for PMMA, because PMMA is widely used for the construction of phantoms for IQA. Blocks of 20 mm were used for the measurements A QRM 2DMC phantom (Quality Assurance in Radiology and Medicine, Moehrendorf, Germany) was used for calibration of the HU measurement (figure 5.2c), since the measured HU values tend to deviate from the actual HU value on CBCT systems [41].

Figure 5.2 – Material samples and calibration phantom. A) Monocalcium phosphate samples in custom containers. B) PMMA sample. C) Calibration phantom (Quality Assurance in Radiology and Medicine, Moehrendorf, Germany)[54].

5.2.2 EXPERIMENTAL SETUP

A Philips Allura FD20 x-ray system (Philips Healthcare, Best, the Netherlands) within a testing facility "Pieterburen" at Philips Healthcare in Best, the Netherlands, was used to measure the radiodensity of the included TEM samples. The TEM samples were placed at the head side of the patient table (Maquet holding B.V. & Co. KG, Rastatt, Germany) along with the calibration phantom (QRM, Moehrendorf, Germany) and a Head XperCT low dose, fast acquisition protocol was performed (at 120 kVp) to acquire the 3D reconstructed image of the TEMs. The data were stored in DICOM format on a computer that was connected to the Allura system (figure 5.3).

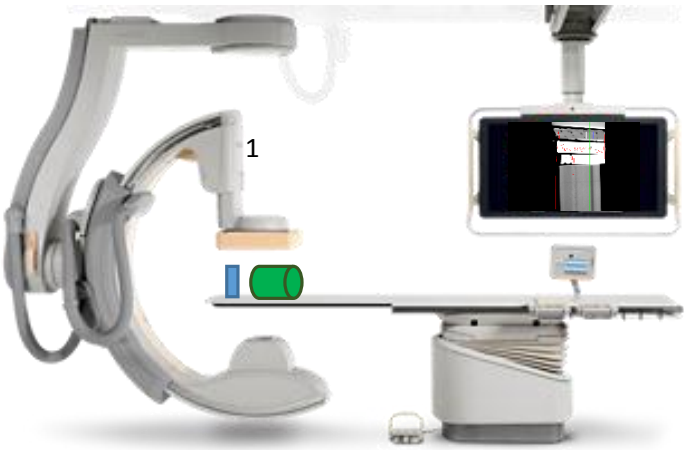

Figure 5.3 – Philips Allura FD20 x-ray system (Philips Healthcare, Best, the Netherlands) [50], *which was used for the radiodensity measurements. The TEM sample (blue box) and calibration phantom (green cylinder) were placed at the head position of the patient table and a 3D reconstruction was made using the C-arm (1) of the Allura.*

5.2.3 DATA PROCESSING

The HU values from the data were obtained using an image processing tool (DviewX, P. van der Haar, Philips Healthcare, Best, the Netherlands) (figure 5.4). DviewX converts the voxel values (V) of the Allura's detector to HU values via a linear scaling of the integer value range (0 to 65535) of the detector to a HU value range of -1000 to 3000 HU (equation 5.2).

$$HU = aV + i \tag{5.2}$$

Where a is the slope of the converted linear HU scale, V is the voxel value and i is an intercept value. The median HU value of each measured sample in DviewX was calculated by manually assessing the HU value at 10 points at three slices of the 3D volume per TEM sample.

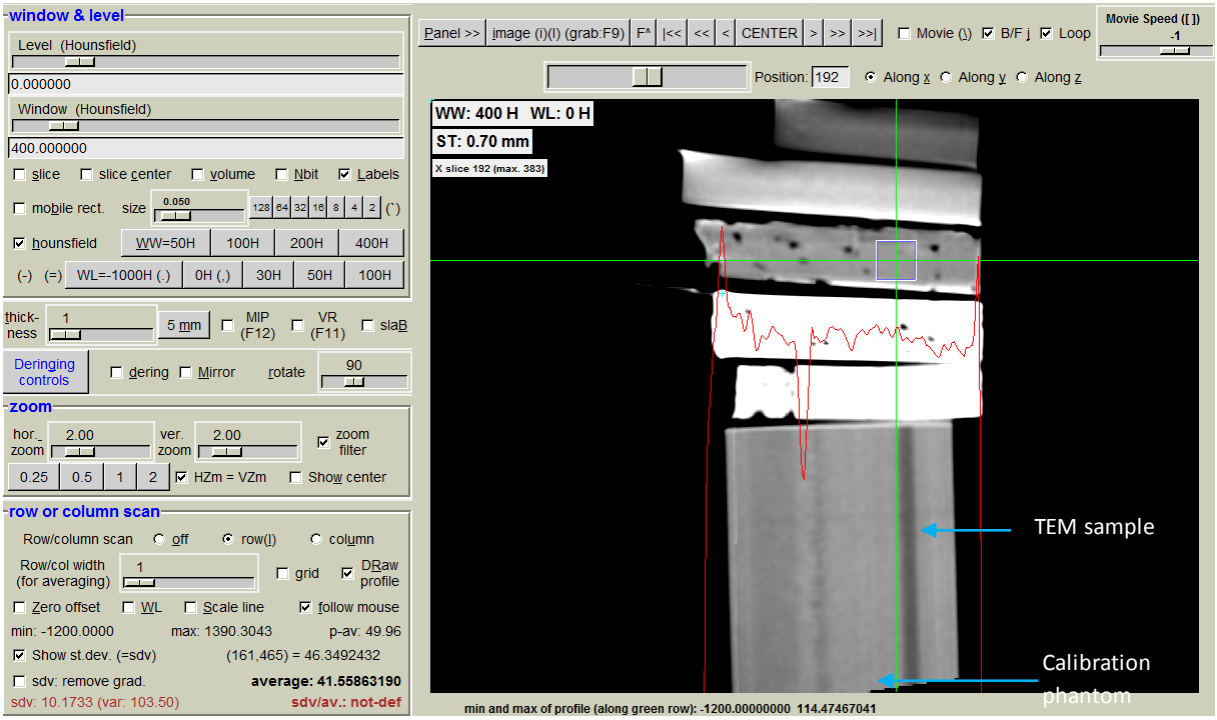

Figure 5.4 – x-ray image processing tool for the radiodensity measurements of the materials (DviewX, P. van der Haar, Philips Healthcare, Best, the Netherlands), displaying one slice of the 3D CT- volume.

Corrections for measurement bias and scaling effects

Because HU that are obtained with a CBCT system can deviate from the true HU value of the material, a calibration was performed using a calibration phantom (QRM-2DMC, QRM, Moehrendorf, Germany) with known HU values. The base material of this calibration phantom has a HU value of 38 HU. The HU deviation was determined by performing 30 HU measurements on the calibration phantom and subtracting the average measured value from 38 (e.g. the average HU value of 48 was measured on the phantom, so the bias of the measurement is 10 HU and needs to be subtracted from the other measurements). Scaling effects of the measurement were assessed by calculating the relative HU values at three different locations of the calibration phantom (at the 38 HU base material and at the -25 and -100 HU inserts, relatively to the base material). The measured HU values of the TEM samples are presented in the following section of this chapter.

5.3 RESULTS

Figure 5.5 is a summary plot of the HU values of the measurements before calibration for the HU bias and the theoretical HU values, calculated using formula 5.1, are also plotted for comparison. The data of the measurements can be found in appendix c.

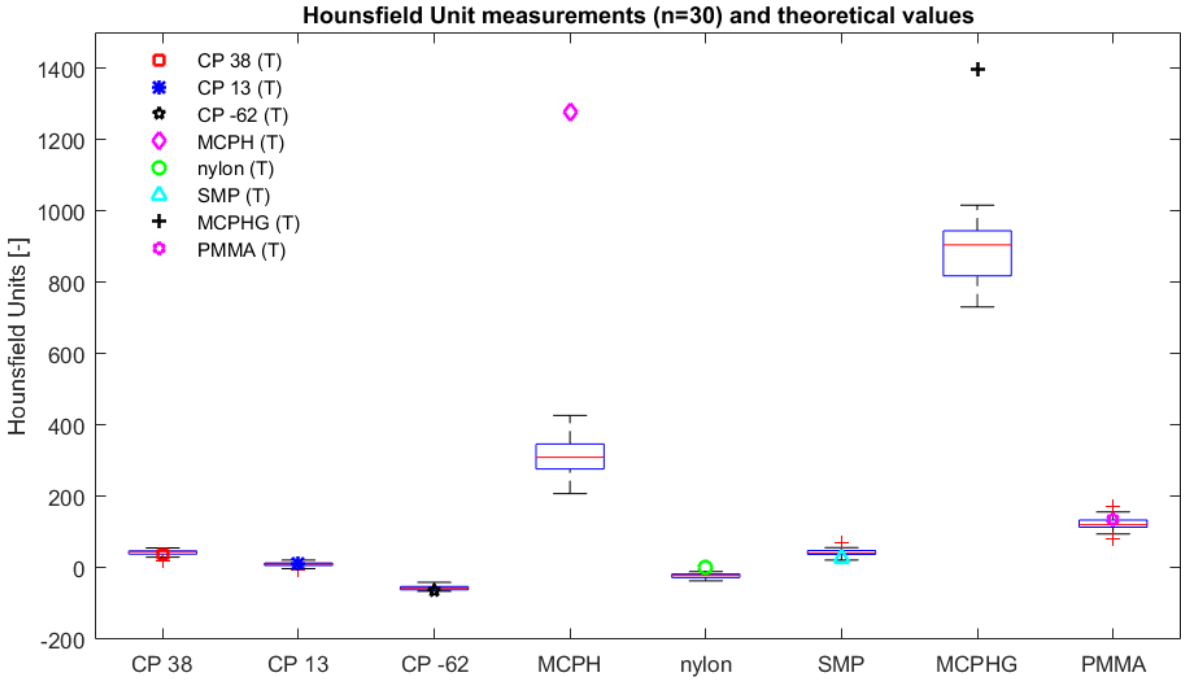

Figure 5.5 – Summary plot of the measured Hounsfield Units of the calibration phantom (CP) at 38, 13 and -62 HU (n=30) and each individual TEM (n = 30). The theoretical (T) values are plotted for reference and comparison.

A summary of the median, 25th percentile (Q1) and 75th percentile (Q3) HU values of the measurements along with the theoretical HU values are presented in table 5.2.

Table 5.2 – Summary of the HU measurements for the calibration phantom (CP) and TEMs.

TEM	Median HU value	Q1	Q3	Theoretical HU value (at 120 keV)
CP 38	46	39	48	38
CP 13	12	7	14	-13
CP -62	-56	-61	-52	-62
MCPH	310	277	347	1275
Nylon	-21	-27	-17	1
SMP	42	38	49	27
MCPHG	905	818	944	1398
PMMA	121	114	134	135

5.4 DISCUSSION OF THE RESULTS

The measured HU values for MCPH were significantly lower than the expectations based on the calculation of the linear attenuation coefficient. This could have two causes. The first possible cause is that due to the relatively big grain size, much air was trapped between the grains. The presence of air can influence the HU value of the measurement negatively if an average voxel value of a MCPH grain and air is calculated. The second possible cause is that the physical density of the MCPH sample was too low, because of the air between the grains.

While nylon had a representative theoretical radiodensity, in practice the case was different. The HU values were outside the HU range of brain tissue and therefore nylon seems not usable as brain equivalent material in terms of radiodensity. However, nylon could still be used as muscle equivalent material, because of the following reasons. The first reason is that the human face is not just composed of muscle tissue, but it is also composed of adipose (fat) tissue. The radiodensity of adipose tissue is much lower that muscle tissue (between -100 and -50 HU), so by averaging the radiodensity of muscle tissue and adipose tissue, nylon can be considered as a representative 'soft tissue' (muscle plus adipose tissue) equivalent material, since the measured HU values fall within this range. Another reason to choose for nylon is the fact that nylon is a durable and easy to work with material, which is suitable for rapid prototyping techniques (as shown in the previously performed literature study). The third reason to consider nylon as muscle equivalent material is that for the IQA purposes of the phantom, the radiodensity of this region in the head is less relevant. Especially bone and brain equivalent materials should have a representative radiodensity. Therefore, unless a better alternative for muscle tissue can be found in the future, nylon can still be considered the best option for muscle equivalent material.

Because nylon turned out to be not very suitable as brain equivalent material, an alternative material (SMP) was introduced for this purpose in the second iteration. SMP has representative HU values compared to brain tissue. However, while injecting the SMP into the container, some air bubbles got trapped within the sample during injection using a narrow nozzle. Therefore, in future usage, SMP should be carefully injected with a wider nozzle in order to prevent the formation of air bubbles (a simple test has shown that this is possible).

The HU values of the MCPHG sample were lower than the theoretical HU value, but fell well within the theoretical range of HU values for bone tissue. Therefore, this mixture is considered a representative bone equivalent material in terms of radiodensity. However, during the hardening process of the material, air bubbles got trapped inside the material. The amount of air bubbles can be reduced by thorough stirring of the material during the hardening process.

The measurements also show that PMMA, which is a widely used material for the construction of phantoms for IQA purposes, is not very representative as a brain equivalent material in terms of radiodensity.

5.5 CONCLUSION

From the four included materials, two materials have representative HU values compared to the HU values of human tissue. In terms of radiodensity, the MCPHG and SMP are representative as bone and brain equivalent material, respectively. Nylon had lower HU values than expected, but due to the good durability and suitability for the available fabrication methods and due to the fact that the human tissue is not only composed of muscle tissue, but is also composed of adipose (fat) tissue, which has much lower HU values, nylon is still considered as a representative muscle (plus adipose) equivalent material in terms of radiodensity.

6

SCATTER CHARACTERISTICS OF THE TEMS

6.1 INTRODUCTION

As explained in chapter 2, the attenuation characteristics of a material are defined by both the absorption and the scatter characteristics of the material. Some researchers have already evaluated the scatter characteristics of several TEMs for radiological purposes, such as for nylon and for water [36], [42], [43]. However, the materials that were investigated are only measured for coherent (Rayleigh) scattering, while incoherent (Compton) scattering is also part of the interaction between x-ray and matter. Also, the techniques that were used in these studies only provide the scatter characteristics for a specific scattering angle, while it is of interest to know the spatial distribution of the scatter radiation. Furthermore, the bone and brain equivalent materials that were introduced in this project for further research have not been quantified yet in terms of scatter. This chapter describes the methodology that was used to measure the scatter characteristics of the included TEMs and provides the results of the scatter measurements for the TEMs.

6.1.1 SCATTER MEASUREMENT TECHNIQUES

Several techniques are described in the literature for the measurement of scatter. The following section is a comparison of techniques for scatter measurement which are commonly used. Based on this comparison, the measurement technique that was most suitable for the implementation into the existing experimental equipment (Allura FD20 x-ray system within a testing facility that resembles an operating room environment) and provided the most relevant quantification metrics was selected.

The energy dispersive x-ray technique

The energy dispersive x-ray technique (also known as the small angle technique) uses one detector to measure the energy distribution of the scattered photons and another detector to measure the energy distribution of the transmitted photons. One photon detector is placed at a small angle (e.g. 7 degrees) from the photon path and another photon detector is placed at the end of the beam, opposite to the x-ray source tube. A collimator is placed between the x-ray source tube and the detectors, to reduce the beam size. The material sample that is measured is placed on top of the goniometer, where the collimated beam passes through the material (6.1a). The output of this measurement provides the magnitude and the scatter spread for a specific scatter angle [43] (figure 6.1b).

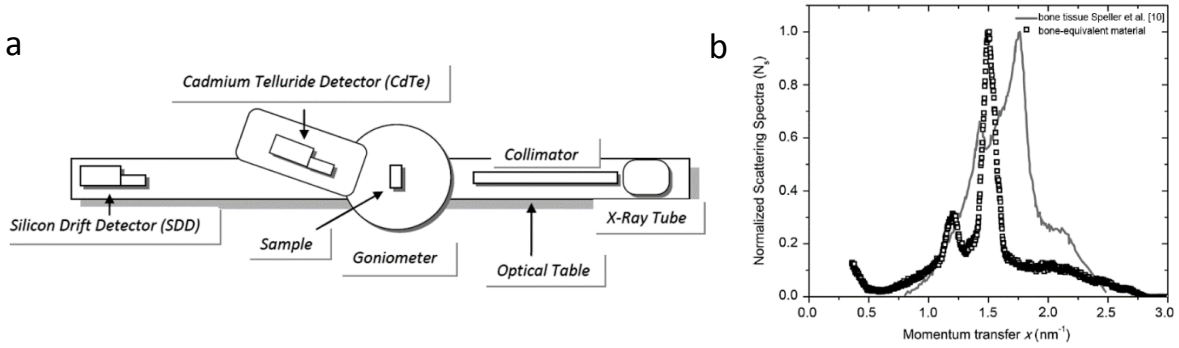

Figure 6.1 – Energy dispersive technique for scatter measurement a) schematic drawing of the experimental setup. B) scatter function that is produced with this measurement technique. Adopted from [43].

The beam stop technique

One of the best known techniques for scatter *estimation* is the beam stop technique. A radiodense (e.g. lead) plate with holes is positioned between the x-ray source tube and the detector and the material of interest is positioned between the radiodense plate and the detector (figure 6.2a). the radiodense plate blocks the primary photon beam in the regions where no openings are present and the remaining narrow photon beams pass through the holes. With no material sample between the radiodense plate and the detector, this creates a characteristic pattern on the detector. When a material sample is placed between the radiodense plate and the detector, the material will scatter a part of photons within the narrow beams, which results in a signal outside of the characteristic pattern on the detector. By subtracting an empty measurement from a measurement with material sample, the scatter magnitude can then be estimated using extrapolation of each individual signal (figure 6.2b).

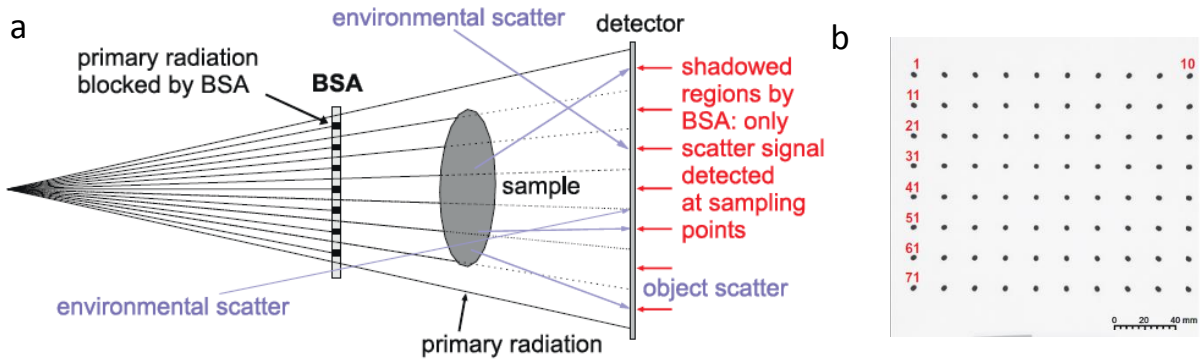

Figure 6.2 – Beam stop technique. A) a radiodense plate with holes, called the beam stop array (BSA) is positioned between the photon beam and the detector. B) Small portions of the beam pass through the BSA and fall on the detector. The detector signal is extrapolated to estimate the scatter magnitude. Adopted from [59]

The edge spread technique

The edge spread technique is a slight variation of the beam stop technique, where the scatter magnitude and spatial scatter distribution can be measured directly, without having to subtract the scatter measurement from the primary measurement (which is the case for the beam stop technique). A radiodense plate is positioned between the x-ray source and a detector. This plate blocks one part of the primary photon beam that should reach the detector and lets another part of the primary photon beam pass onto the detector. When a material is positioned between the radiodense plate and the detector, scattered photons of the material reach the part of the detector behind the radiodense plate (figure 6.3a) [44]. This signal can be directly measured as the scatter magnitude and spatial scatter distribution behind the lead plate. The maximal scatter to primary ratio can be estimated using this technique (figure 6.3b).

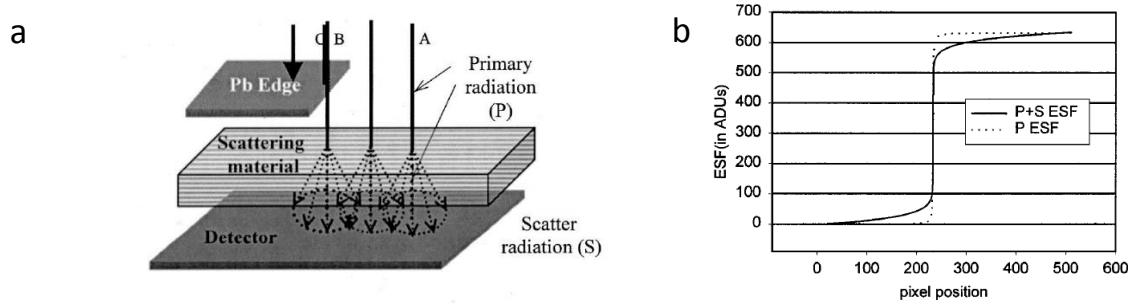

Figure 6.3 – Edge spread technique. A) schematic overview of the edge spread technique. A portion of the primary photon beam is blocked with a radiodense plate. Scattered photons by the measured material fall on the detector behind the radiodense plate and can be directly measured for the magnitude and distribution. B) example of a (ideal) scatter function. Adopted from [60].

Table 6.1 – Overview of the experimental techniques for the measurement of scatter characteristics.

Scatter measurement technique	Quantification of the scatter magnitude	Quantification of the scatter distribution	Easy integration in available equipment
EDX technique	Yes	No	No, needs a second detector
Beam stop technique	Yes*	No	No, needs a complex beam stopper plate
Edge spread technique	Yes*	Yes	Yes

* The scatter magnitude is estimated and not measured in the scatter plus primary region of the image

6.2 MATERIALS AND METHODS

Based on the comparison of scatter measurement techniques, the edge spread technique is the easiest one to implement into the available experimental equipment and provides both the scatter magnitude and distribution. For these reasons, this technique was selected for the measurement of the scatter characteristics of the TEMs. This section describes the methodology of the experiment and the steps for data processing of the measurements.

6.2.1 MATERIAL SAMPLES AND EXPERIMENTAL DESIGN

The scatter characteristics of the TEMs (nylon, SMP, MCPH (powder), MCPHG and PMMA) were measured for three different thicknesses per TEM type (20, 40 and 60 mm). The SMP polymer and MCPH powder were filled in custom made PMMA containers (figure 6.4). The 20 mm and 40 mm samples of PMMA, nylon and the MCPHG were closely taped together to make the 60 mm sample. The TEM samples were radiated at four different tube voltages in the lower diagnostic energy range (60, 80, 100 and 120 kVp at 100 mA) using the Allura FD20 x-ray system[3], which was modified for the edge spread technique for scatter quantification (see section 6.2.2).

Figure 6.4 – Experimental setup. 1) detector 2) radiodense (3mm lead) plate 3) TEM samples in 20, 40 and 60 mm thickness.

After validation of the experimental setup, the measured scatter characteristics of the TEMs were compared with MC simulations of the scatter characteristics of bone, muscle and brain tissue. Table 6.2 is an overview of which TEM is compared to which simulated tissue.

Table 6.2 – Included materials for measurement and comparison with Monte Carlo based scatter simulations.

Measured (tissue equivalent) material	Simulated tissue/material
Monocalcium phosphate powder (MCPH)	Bone tissue
Nylon	Muscle tissue
Silyl modified polymer (SMP)	Brain tissue
Monocalcium phosphate/gypsum mixture (MCPHG)	Bone tissue
Polymethylmethacrylate (PMMA)	PMMA (for validation)
PMMA	Brain tissue

[3] Two different Allura x-ray systems in two different test labs (Pieterburen lab and IGIT lab) were used for the measurements due to the available time slots.

6.2.2 OVERVIEW OF THE EXPERIMENTAL SETUP

The following figure is an overview of the entire experimental setup (figure 6.8).
The TEMs were measured with the Allura FD20 x-ray system. The anti-scatter grid in front of the Allura's flat detector was removed before the experiments. The C-arm of the Allura in the Pieterburen lab was positioned in a 90 degrees roll and the detector was positioned in portrait mode. A lead plate (200 mm by 100 mm by 3 mm) was positioned at a distance of 200 mm from the detector using a custom built holder and each TEM sample was positioned at 100 mm distance from the detector, measured from the center of the material thickness. The x-ray beam was collimated on the remaining three edges using the built in collimator (lead shutters for blockage of the x-ray beam) of the Allura.

A custom image acquisition protocol was created on the Allura for the measurement of the scatter characteristics, where a sequence of 15 fluoroscopic images was shot per measurement. The grey values of each image have a linear scale (with integers from 0 to 65535) and each image was stored directly on a computer that was connected to the Allura system. The images are then processed using Matlab R2015b (Mathworks, Natick, Massachusetts, USA) in order to obtain the characteristic scatter function of each TEM at a specific tube voltage.

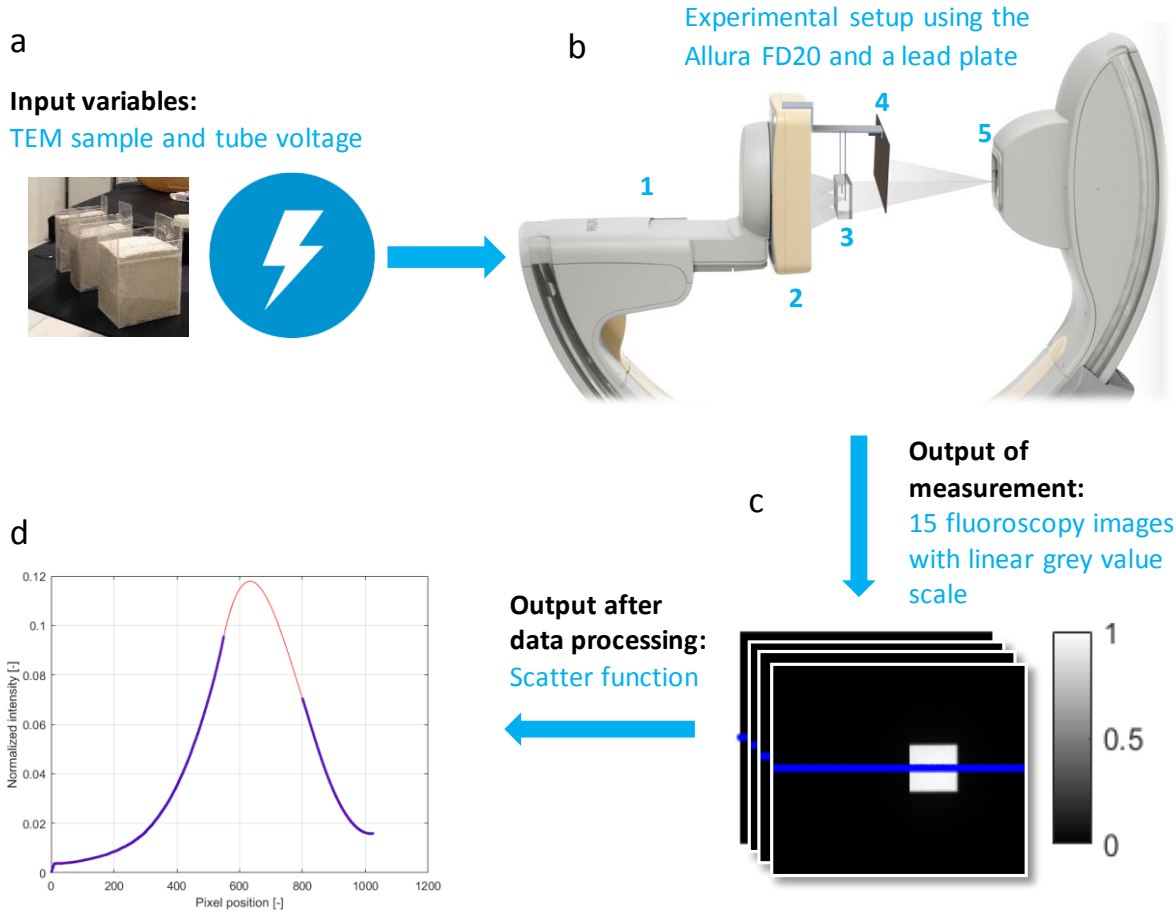

Figure 6.8 – Schematic overview of the experimental design for the measurement of the scatter characteristics. A) The TEM sample thickness and tube voltage are the input variables. B) The Allura FD20 CBCT system (Philips Healthcare, Best, the Netherlands) (1) is modified for the edge spread technique by removing the anti-scatter grid from the detector (2) and the TEM sample (3) is positioned 100 mm from the detector, between the detector and the lead plate (4), which is positioned 200 mm from the detector. The x-ray beam is collimated at the side of the x-ray source (5). C) The output of the measurement is a sequence of 15 fluoroscopic images with linear gray scale (integers from 0 to 65535). D) The data are processed using Matlab R2015b (Mathworks, Natick, Massachusetts, USA) in order to construct the scatter function of each TEM sample with specific thickness at a specific tube voltage.

The conditions of the experimental setup are summarized in table 6.2.

Table 6.2 – Experimental conditions for scatter measurement using the edge spread technique and the Allura FD20.

Experimental conditions	
Material samples	MCPH (grains), nylon, SMP, MCPHG, PMMA
Material thickness	20, 40 and 60 [mm] thickness
Tube voltage	60, 80, 100 and 120 [kVp] (at 100 mA)
Imaging protocol	Sequential CINE fluoroscopy shots (n=15)
Lead plate to detector distance	200 mm
Sample to detector distance	100 mm
Collimator settings	Collimated at 554 to 748 pixels horizontally and 305 to 410 pixels vertically (in landscape mode)

6.2.3 QUANTIFICATION OF THE SCATTER CHARACTERISTICS

The scatter characteristics of the TEMs were quantified in terms of scatter magnitude and spatial scatter distribution. This was done using the edge spread function (ESF), which is a normalized horizontal line of the measured intensities with respect to the vertical pixel position (x) of the flat detector in portrait mode (figure 6.5).

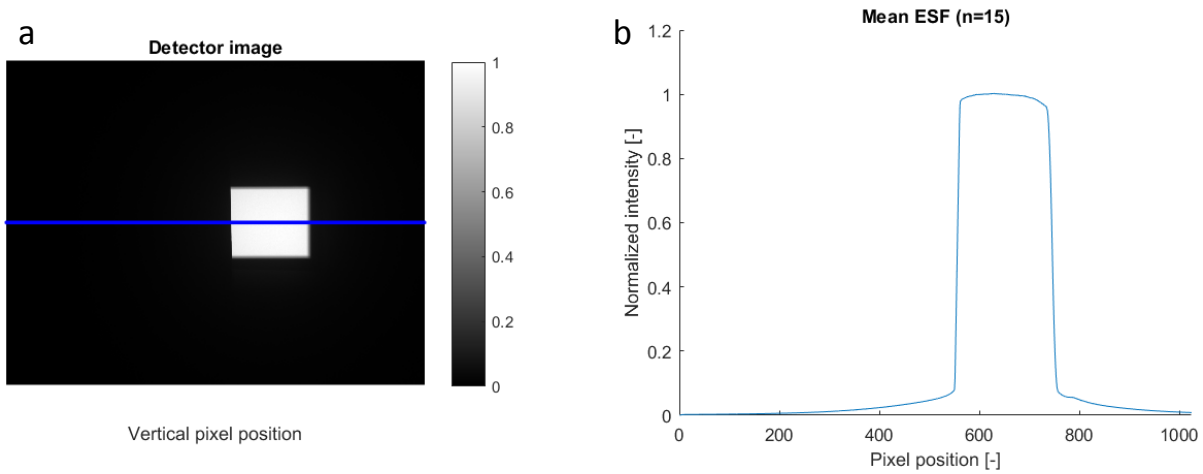

Figure 6.5 – Obtained mean edge spread function (n=15) after averaging, calibration and normalization of the detector image. A) rotated (!) detector image where the horizontal line was analyzed to obtain the ESF. B) mean ESF of 15 detector images.

The ESF is obtained by blocking the incident x-ray beam using a lead plate and collimator shutters of the Allura, in such way that only the TEM sample is radiated. When the x-ray photons pass through the TEM sample, a part of the scattered radiation will fall on the region behind the lead plate, which can be measured directly as pure scatter radiation. The signal on the center region of the detector is a mixture of primary and scatter radiation (figure 6.6).

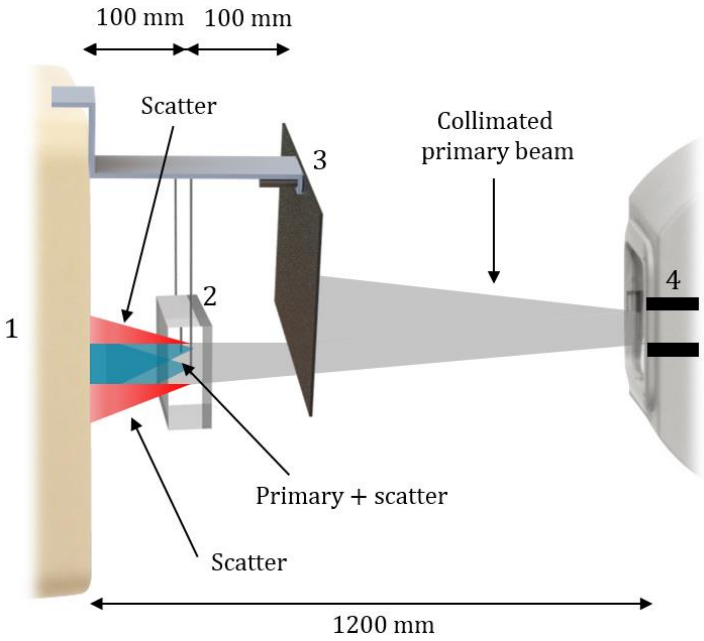

Figure 6.6 – Schematic overview of the experimental setup for the measurement of scatter using a modified version of the edge spread technique [60]. *The anti-scatter grid in front of the flat detector of the Allura FD20 x-ray system (1) was removed and the TEM sample (2) was positioned between the detector and a lead plate (3). The lead plate and built in collimator shutters of the Allura (4) are used to block a portion of the incident x-ray beam so only the TEM is radiated. Scatter radiation falls on the regions behind the lead plate and can be directly measured this way. The signal on the center region of the flat detector is a mixture of the primary and scatter signal.*

The scatter magnitude was quantified as the max scatter to primary ratio ($MSPR$) (figure 6.7) (equation 6.1).

$$MSPR = \frac{\max(S(x))}{P(x)} \tag{6.1}$$

Where $S(x)$ is the scatter function and $P(x)$ is the primary function with respect to the pixel position (x). $S(x)$ and $P(x)$ are both derived from the mean ESF (see section 6.2.4 on the next page). The scatter magnitude was also quantified as the edge magnitude (EM), which is the scatter magnitude at the edge of the lead plate (figure 6.7) (equation 6.2).

$$EM = S(x_l) \tag{6.2}$$

Where x_l is the pixel position of the scatter function S at the edge of the lead plate on the image. On the ESF, this is the point where the signal drastically starts to increase. x_l can be obtained by differentiating the ESF twice with respect to the pixel position (x) and taking the position where the maximal value of the differentiated function occurs (equation 6.3).

$$x_l = \max\left(\frac{d^2 ESF(x)}{dx^2}\right) \tag{6.3}$$

The scatter distribution (SD) was quantified as the pixel position behind the lead plate where the scatter signal was 2% of the normalized ESF signal (figure 6.7). The threshold of 2% was chosen because a smaller magnitude (<2%) would result in less distinctive SD for different thicknesses.

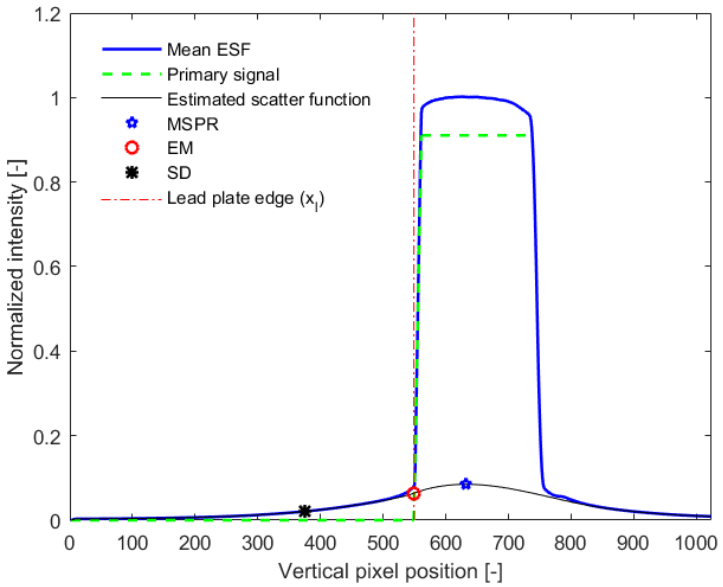

Figure 6.7 – Visualization of the metrics for the quantification of the scatter characteristics. The blue line is the mean ESF (n=15), which was obtained from a sequence of 15 x-ray images and the scatter function (black line) and primary function (green dashed line) were estimated and calculated. The red dash dot line represents the edge of the lead plate, where the signal left from this line is pure scatter and the signal right from this line is the scatter plus primary signal.

6.2.4 DATA PROCESSING

The following steps were taken in order to process the data of the measurements (figure 6.9):

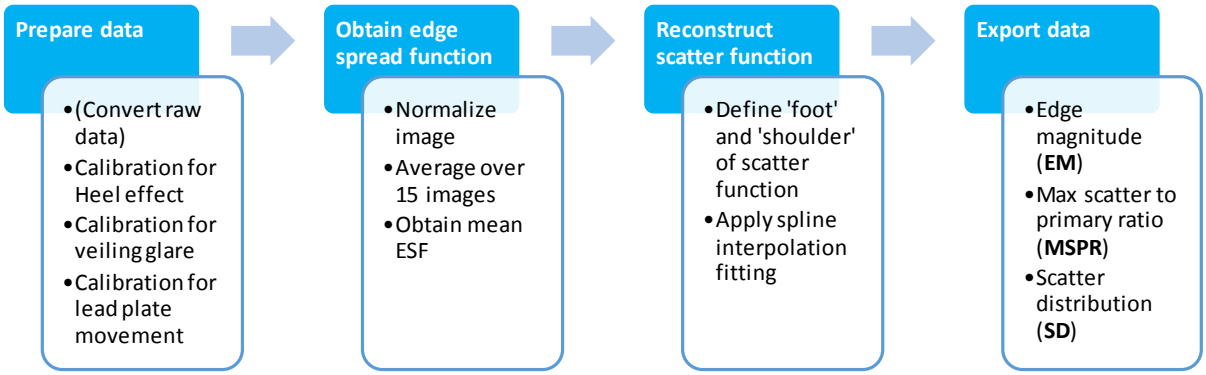

Figure 6.9 – Schematic overview of the data processing methodology.

Prior to the data processing of the images using Matlab, the sequence of 15 raw images was converted from .dvlp format to a matrix $[I]$ of 1024 by 768 integer elements (with a range of 0 to 65535). The images were then individually calibrated for several influencing effects of the (x-ray) system, which could cause a bias in the output. These effects include the Heel effect of the anode, veiling glare of the detector and movements of the lead plate. The images were normalized after calibration and the mean ESF was obtained from the 15 images after averaging of the sequence of images. The mean ESF was used to estimate the scatter function, by applying a spline interpolation between the measured pure scatter fractions behind the lead plate and collimator shutter. Finally, the metrics for the scatter characteristics were obtained from the scatter function.

Calibration for the Heel effect

The anode of the x-ray system causes the Heel effect, which results a gradient in the intensity of the image (figure 6.10). Not calibrating could introduce inaccuracies during the normalization of the image. This effect was calibrated for by element-wise division (./) of the image matrix of an empty Heel effect measurement [H] by the image matrix of a TEM measurement [I] (equation 6.5).

$$[I_H] = [\mathrm{H}]./[\mathrm{I}] \tag{6.5}$$

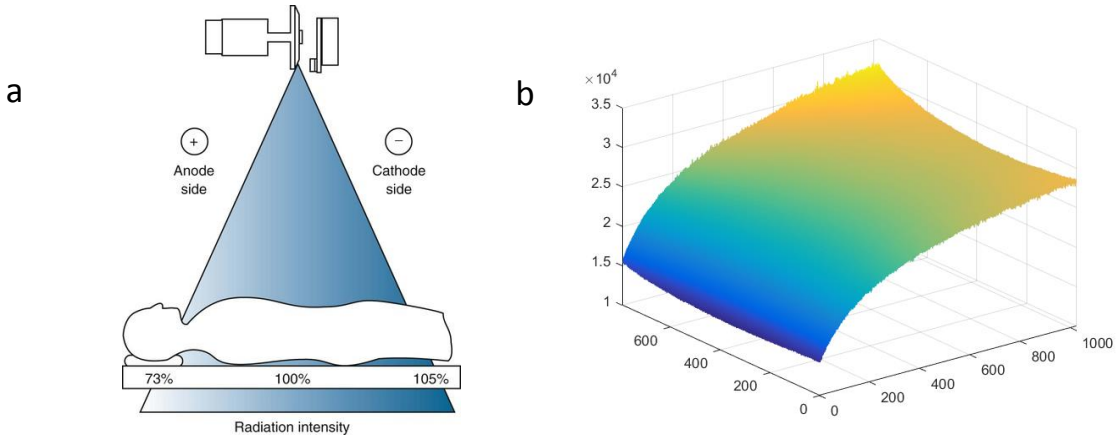

Figure 6.10 – The Heel effect. A) Schematic drawing of the Heel effect in a clinical setting. B) Measurement of the Heel effect on the Allura FD20 (Philips Healthcare, Best, the Netherlands)

Figure 6.11a and b show the mean ESF before and after calibration for the Heel effect. What can be seen is a clear slope at the top region of the mean ESF before calibration, where the mean ESF after calibration has a symmetrical top region.

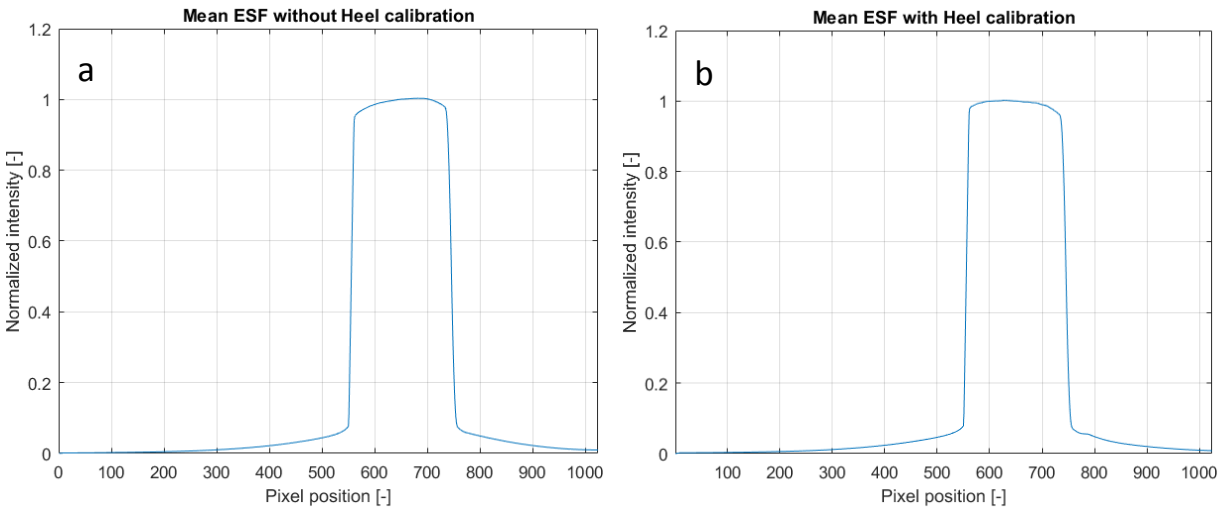

Figure 6.11 – Calibration of the Heel effect. A) Normalized mean ESF before calibration for the Heel effect. B) Normalized mean ESF after calibration for Heel effect.

Calibration for veiling glare

The flat detector of the Allura system may scatter as well, which is known as veiling glare of the detector. The effect of veiling glare can result in an overestimation of up to 15% of the scatter function at the edge of the lead plate [45] and should therefore be corrected for. The effect of veiling glare was calibrated for by conducting an empty (collimated) air measurement and subtracting the measured veiling glare signal at the region behind the lead plate ($\mathbf{v}$) from the scatter fraction of the TEM sample behind the lead plate ($\mathbf{s}$) (equation 6.6). For this calibration step, the contribution of scatter radiation by air was assumed to be zero.

$$\boldsymbol{s_v}=\mathbf{s}-\mathbf{v}=(s_1\ s_2\cdots s_{xl})-(v_1 v_2\cdots v_{xl}) \tag{6.6}$$

Where $\mathbf{s_v}$ is the resulting scatter signal behind the lead plate after calibration and $x_i$is the position of 'foot' of the edge spread function at the edge of the lead plate from equation 6.3. Figure 6.12 shows the left side of the mean ESF where the scatter function is obtained after calibration for veiling glare. The same calibration was performed at the right (collimator) side of the mean ESF (not shown in the figure).

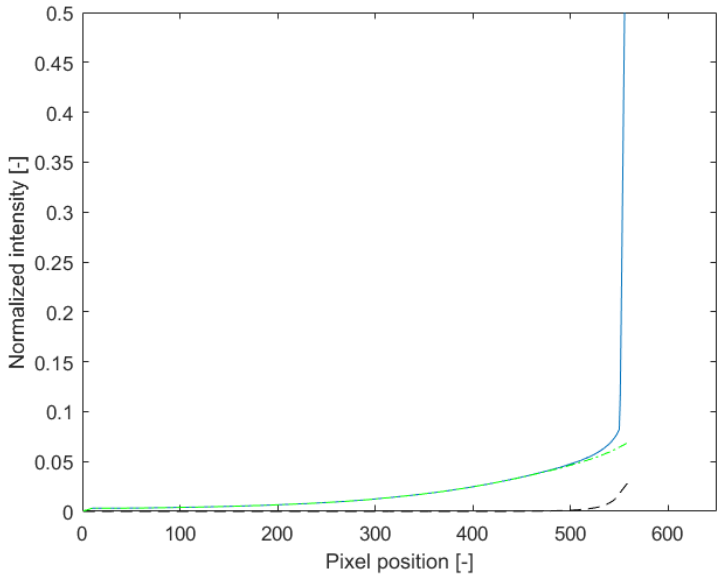

Figure 6.12 – Calibration for veiling glare. The veiling glare (black dashed line) is subtracted from the mean ESF (blue line), resulting in the calibrated scatter signal of the material behind the lead plate (green dash dot line). The same step was performed for the right side of the mean ESF.

Calibration for lead plate movements

The lead plate that is positioned in front of the detector can have slight up and down movements during the positioning of the TEM, which can cause a shift of the edge of the lead plate on the image. When calibrating for veiling glare, it is important that the edges of the air measurement and the TEM measurement are aligned. Otherwise, too much or too little signal of the veiling glare can be subtracted from the ESF. The veiling glare calibration is performed by aligning the lead edge of each air measurement with the lead edge of the material sample measurement (equation 6.7).

$$\mathbf{s_m}=\mathbf{s_v}-(\mathbf{v}-\mathbf{v'}) \tag{6.7}$$

Where $\mathbf{s_m}$ is the aligned calibrated signal behind the lead plate and where $\mathbf{v'}$ is the difference array between the edge position of the air measurement and the edge position of the TEM measurement.

Normalization and averaging of the image

The normalization of the image for homogeneous materials (e.g. PMMA, nylon) was done by calculating the maximal intensity value of the image (equation 6.8). A Gaussian filter was applied to blur the image in order to remove outliers due to noise in the image.

$$[\mathrm{I_n}] = \frac{[\mathrm{I}]}{\max(\mathrm{blur}([\mathrm{I}]))} \tag{6.8}$$

Where I_n is the matrix of the normalized image. Because heterogeneous materials (e.g. SMP, MCPH, MCPHG) have a wide variety in intensities in the scatter plus primary region, an average value of this region was calculated and used as maximal intensity value for the normalization (equation 6.9).

$$[\mathrm{I_h}] = \frac{[\mathrm{I}]}{\max((\mathrm{blur}([\mathrm{I_{S+P}}]))} \tag{6.9}$$

Where $[\mathrm{I_h}]$ is the matrix of the normalized heterogeneous image and I_{s+p} is the matrix of the scatter plus primary region of the heterogeneous image. The average was calculated for the sequence of 15 images and further used for the estimation of the scatter function.

MSPR estimation using spline interpolation

The MSPR cannot be obtained directly from the x-ray image, because the primary and scatter signals cannot be measured independently. However, using the facts that the scatter function must be a continuous function and that the MSPR is at the center of the material region of the image, the scatter and scatter plus primary signals can be estimated using spline interpolation between the two scatter fractions behind the lead plate and the collimator of the Allura.

By identifying the position of the edges of the lead plate (x_l), previously derived in equation 6.3 and the edge of the right collimator shutter along the ESF of the image (x_c) (equation 6.10), two scatter fractions can be obtained.

$$x_c = \min\left(\lim_{x=650\rightarrow1024}\left(\frac{d^2 ESF\,(x)}{dx^2}\right)\right) \tag{6.10}$$

A spline interpolation is then applied between these scatter factions in order to reconstruct the total scatter function (after calibration, normalization and averaging) (figure 6.13).

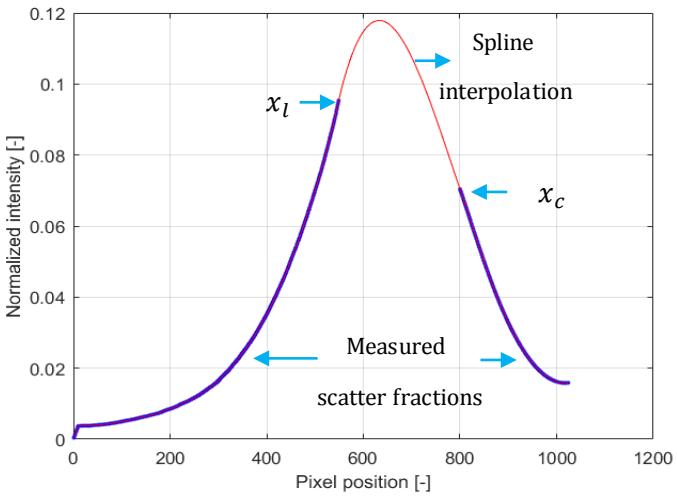

Figure 6.13 – Reconstructed scatter function using a spline interpolation between the scatter fractions. The blue lines are the measured scatter fractions up to the lead plate and collimator edge (x_l and x_c respectively). The red line is the estimated scatter function.

6.2.5 ADDITIONAL CALIBRATION FOR RADIATION LEAKAGE

Because the lead collimator (at the right scatter fraction) showed a significant signal of x-ray photons that apparently have leaked from the collimator shutter (figure 6.14a), an additional calibration step was performed at the right scatter fraction in order to remove the this signal fraction from the mean ESF. This was done by performing a 2nd order polynomial fit between the edge of the collimator (x_c) and the right scatter fraction where the leakage signal stopped (manually determined) (figure 6.14b).

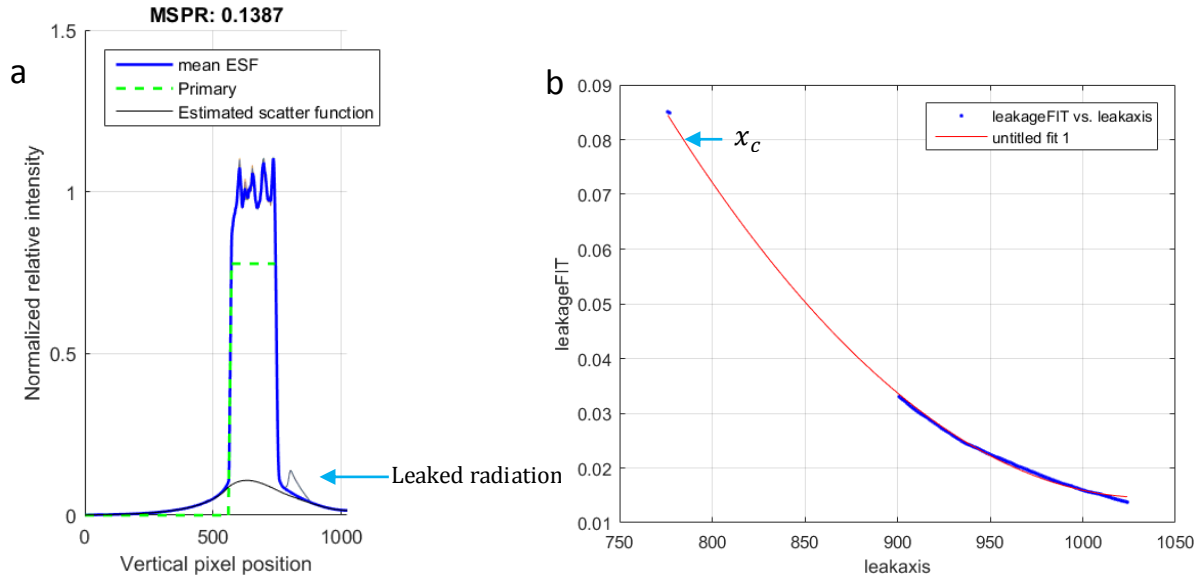

Figure 6.14 – Leaked x-ray photons on the right side of the mean ESF, where the x-ray beam is blocked using the collimator shutter of the Allura. This region is calibrated by removing the peak and applying a 2nd order polynomial fit (red line on right figure) between the collimator edge before leakage (x_c) and the mean ESF after the leakage (blue dots and blue line on the right figure).

6.2.6 VALIDATION EXPERIMENTS AND COMPARISON WITH MC SIMULATIONS

A validation of the experimental setup was performed in order to check in which extent the measured scatter characteristics would resemble the simulated characteristics of a same material, since the comparison between the measured TEMs and simulated tissues can only be done if the scatter characteristics are similar between the measurement and simulation for the same material. For this purpose, the scatter measurements of PMMA samples were compared with MC scatter simulations (Scatter simulator, M. Pieters, Philips Healthcare, Best, the Netherlands) of PMMA, in a similar setup.

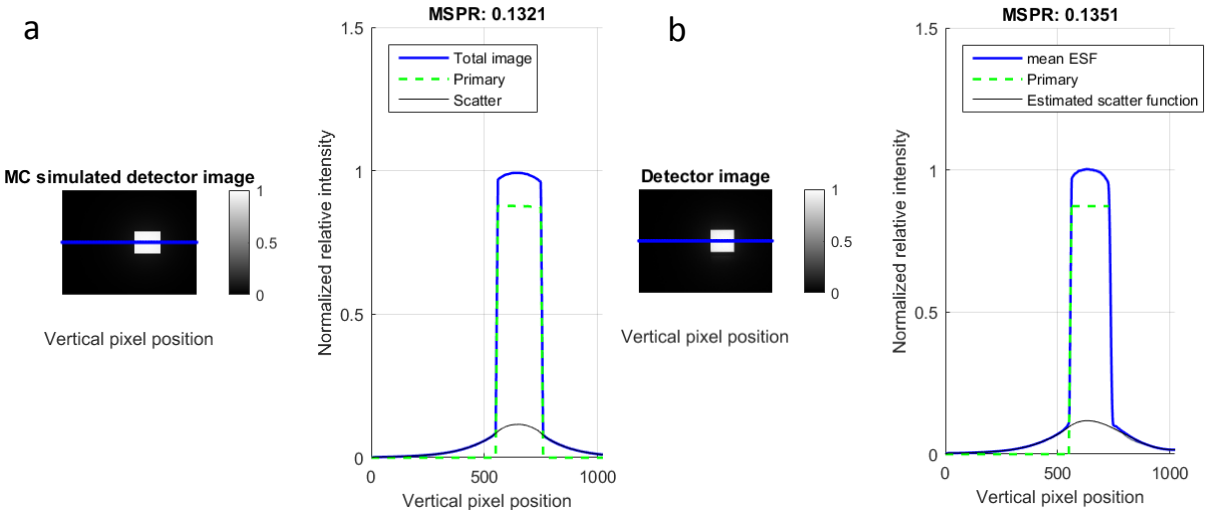

Figure 6.15 – Example of comparison between simulated (a) and measured (b) PMMA sample of 60 mm.

PMMA was selected for the simulation because of two reasons. Firstly, the material is homogeneous and the measurements of homogeneous materials are potentially more accurate compared to heterogeneous materials. Secondly, not many materials are (yet) available in the materials database of the simulator, but PMMA was one of the available materials.

The MSPR, EM and SD of the simulated tissues (bone, muscle and brain) were calculated using equation 6.1 to 6.4. The measured scatter characteristics of the TEMs for all specified material thicknesses (20, 40 and 60 mm) and tube voltages (60, 80, 100 and 120 kVp) were compared with Monte Carlo based simulations by calculating the MSPR *ratio* (equation 6.11), the EM *ratio* (equation 6.12) and SD *ratio* (equation 6.13). Figure 6.15 is an example of a measured scatter function and a simulated scatter function of PMMA. The scatter functions of all measurements and simulations of the TEMS can be found in appendix C. The results that were obtained from these measurements can be found in section 6.3.

$$MSPR\ ratio = \frac{MSPR_m}{MSPR_s} \tag{6.11}$$

$$EM\ ratio = \frac{EM_m}{EM_s} \tag{6.12}$$

$$SD\ ratio = \frac{SD_m}{SD_s} \tag{6.13}$$

Where the $MSPR_m$, EM_m, and SD_m are the MSPR, EM and SD of the measurement respectively and where the $MSPR_s$, EM_s, and SD_s are the MSPR, EM and SD of the simulation respectively.

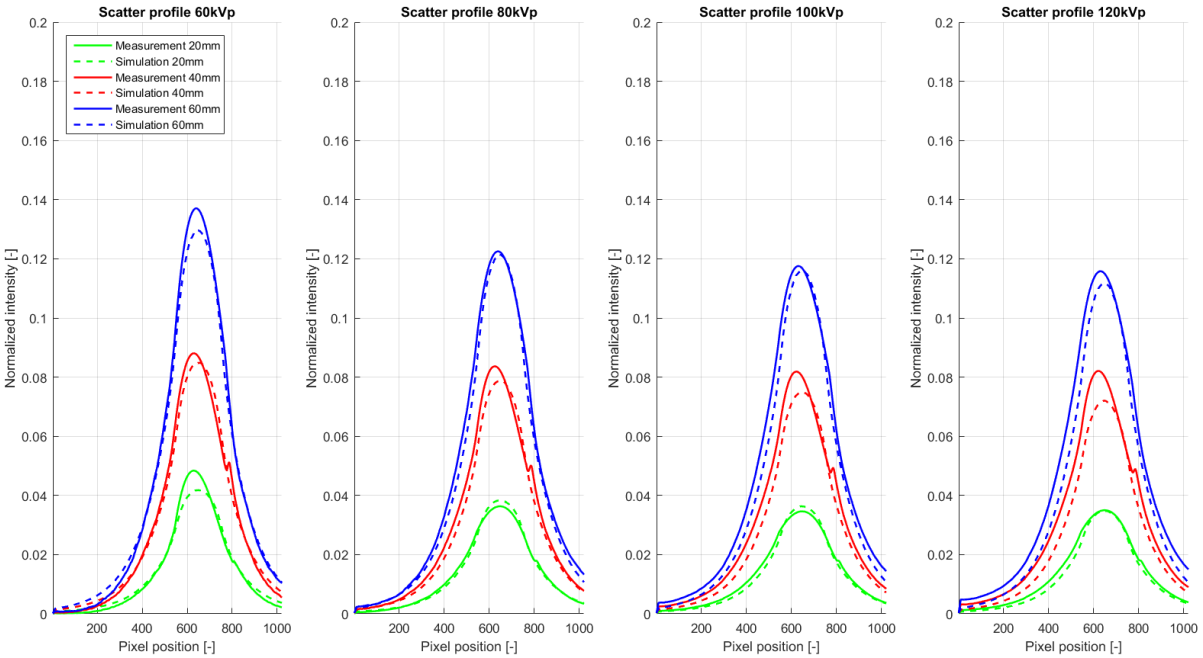

Figure 6.15 – Example of the comparison between Monte Carlo based simulations of scatter and measured scatter of PMMA for all thicknesses and tube voltages. The dashed lines are simulations and the solid lines are measurements of the scatter functions.

6.3 RESULTS

6.3.1 OVERVIEW OF TEM SCATTER CHARACTERISTICS VERSUS SIMULATIONS

This section is an overview of the MSPR, EM and SD of the measurements (PMMA, MCPH, nylon, SMP, MCPH/G), compared with simulations of PMMA and human tissues (bone, muscle and brain). The mean ESF and scatter functions of the individual measurements and simulations can be found in appendix C. The x-ray images and mean ESF of each measurement can be found in appendix D. Each material is plotted against the material/tissue that the material should represent (i.e. MCPH with bone tissue) in figure 6.16 to 6.18. A summary of the ratios between the measured TEM and simulated tissue for each metric can be found in section 6.3.2 of the results.

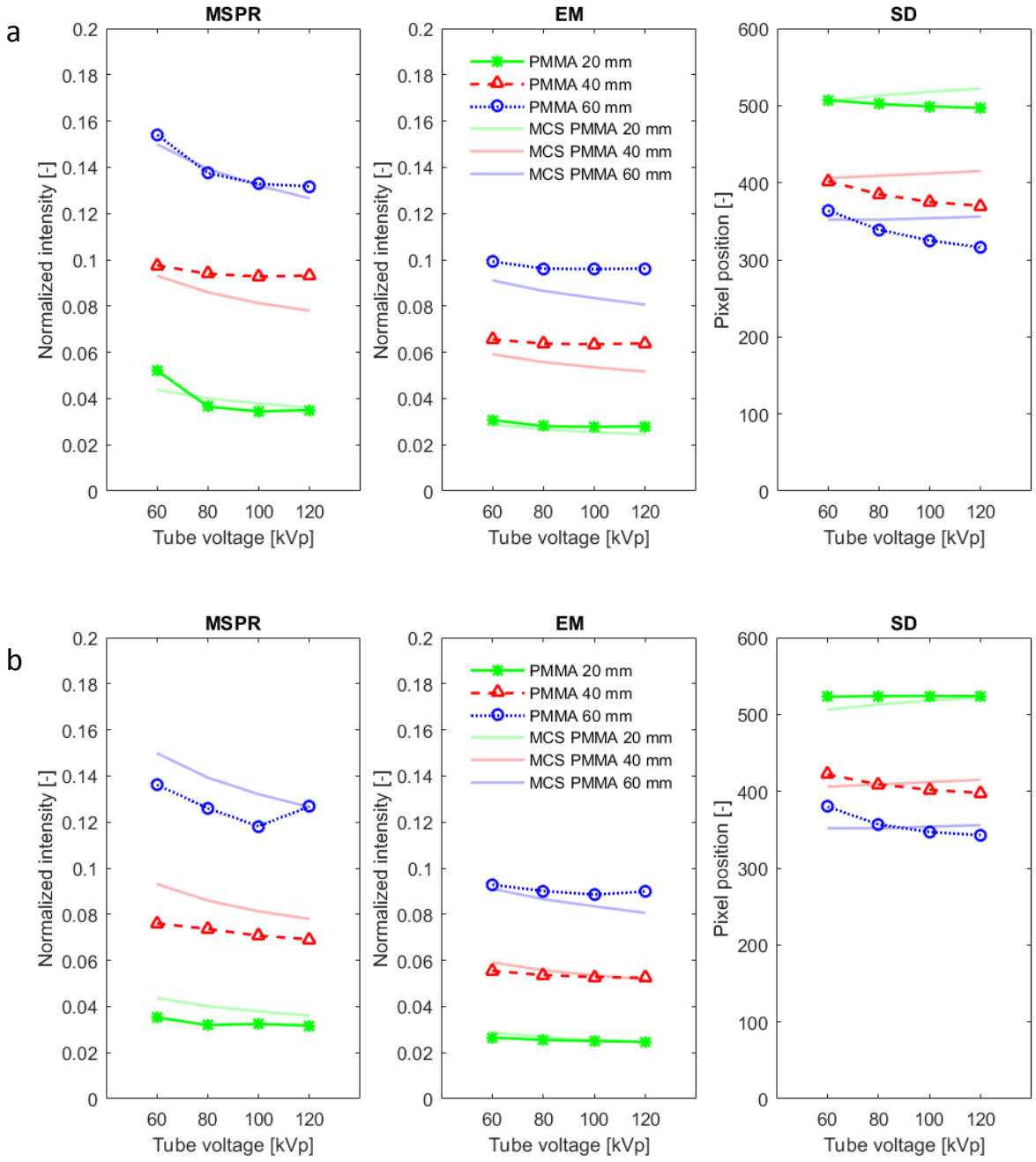

Figure 6.16 – MSPR, EM and SD of the measurements and simulations of PMMA for the validation of the experimental setup. A) Pieterburen lab. B) IGIT lab.

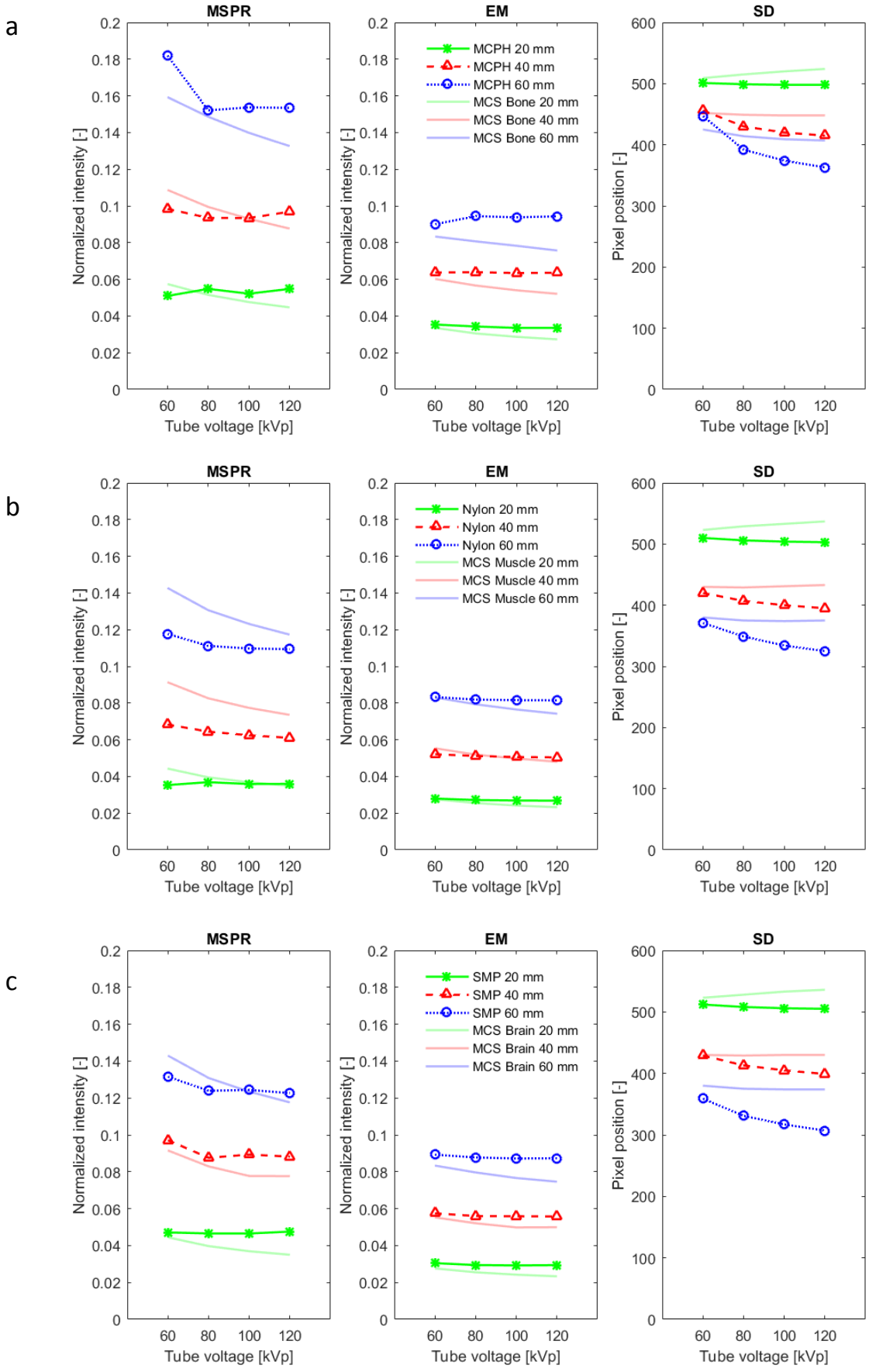

Figure 6.17 – Comparison of the MSPR, EM and SD of the measurements of the TEMs and simulations of the tissues. A) MCPH versus bone tissue. B) Nylon versus muscle tissue. C) SMP versus brain tissue.

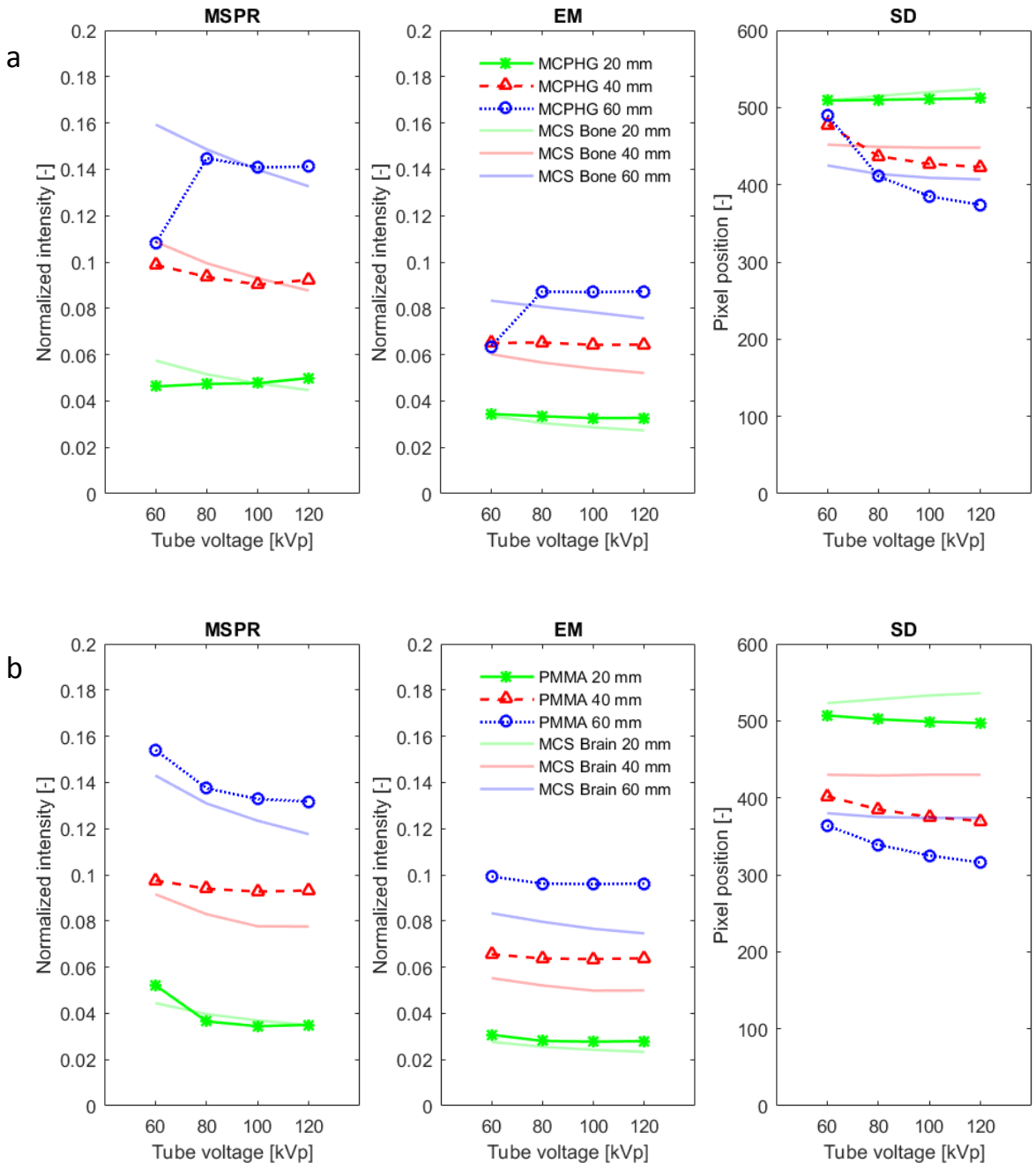

Figure 6.18 – Comparison of the MSPR, EM and SD of the measurements of the TEMs and simulations of the tissues. A) MCPHG versus bone tissue. B) PMMA versus brain tissue.

6.3.2 MEASUREMENT/SIMULATION RATIOS

The median values and the interquartile range of the MSPR ratio, EM ratio and SD ratio between the measurements and simulations are summarized in table 6.3. Figure 6.19 and 6.20 are an overview of the summarized measurement/simulation ratios.

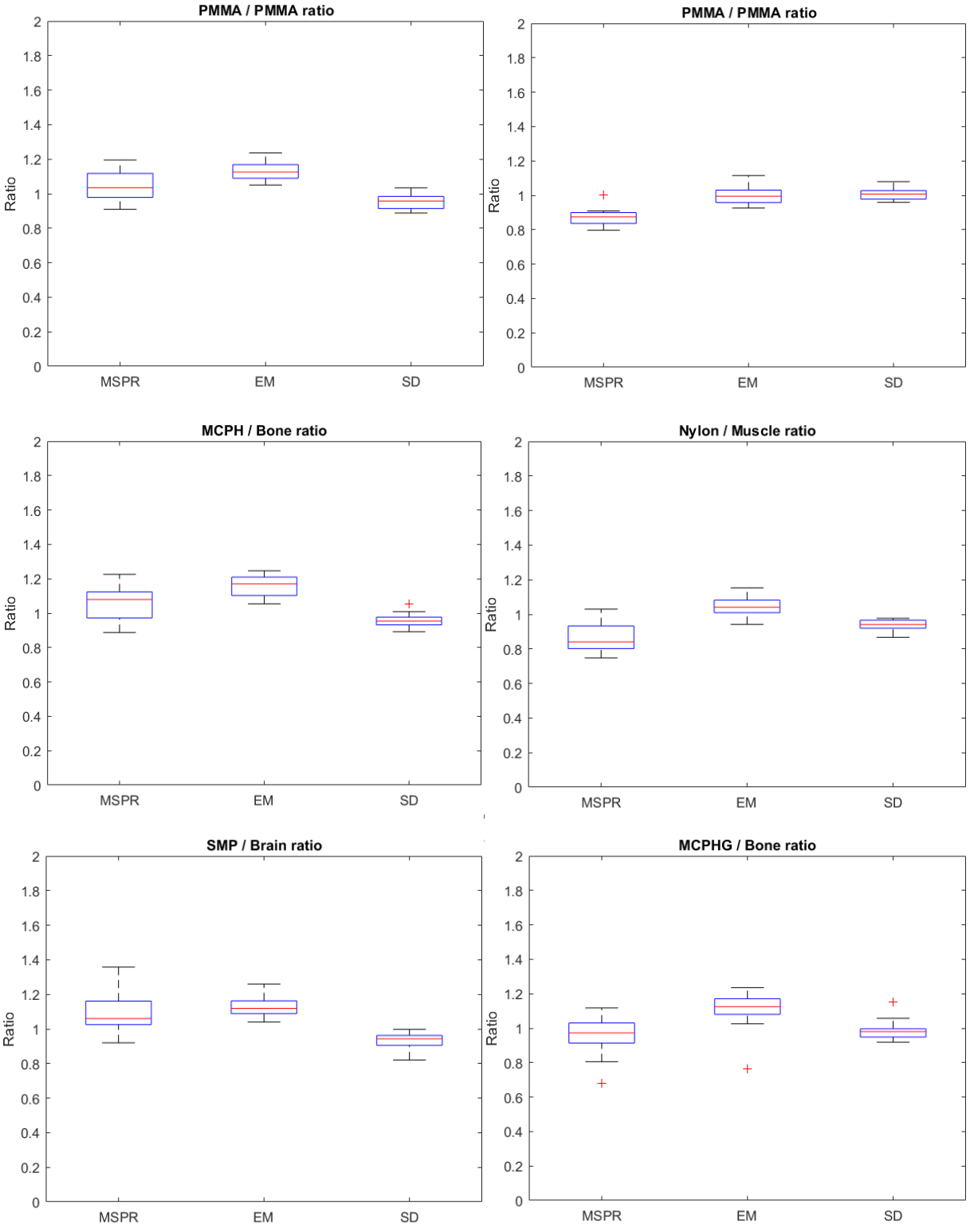

Figure 6.19 – Summary plots of the ratio between the measured TEM and simulated material/tissue.

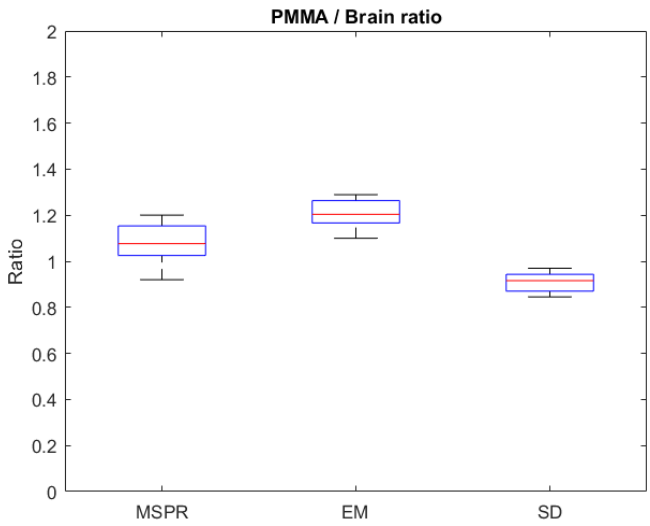

Figure 6.20 – Summary plot of the ratio between the measured TEM and simulated tissue.

Table 6.3 – Median and interquartile range of the ratios between the scatter measurements and simulations.

Material/human tissue	MSPR ratio (n=12)		EM ratio (n=12)		SD ratio (n=12)	
	Median	IQR	Median	IQR	Median	IQR
PMMA PB/PMMA	1.03	0.14	1.13	0.08	0.96	0.07
PMMA IGIT/PMMA	0.87	0.06	1.00	0.07	1.00	0.05
MCPH/bone	1.08	0.15	1.17	0.11	0.95	0.04
Nylon/muscle	0.84	0.13	1.04	0.07	0.94	0.05
SMP/brain	1.06	0.14	1.12	0.07	0.94	0.06
MCPHG/bone	0.95	0.13	1.13	0.10	0.98	0.05
PMMA/Brain	1.07	0.13	1.20	0.10	0.92	0.07

6.4 DISCUSSION

Validity of the experimental setup

The results from the validation of the experimental setup using PMMA showed that the median ratio of the scatter magnitude (MSPR and EM) was between 0.87 and 1.13 and that the median ratio between of the spatial scatter distribution was 0.96 and 1.00. These results suggest that the maximal absolute difference between the measurements and simulations were less than 3 percent.

Interpretation of the results

The comparison between the measured MSPR, EM and SD showed that the proposed TEMs are overall in good agreement with the simulations of the tissues which the TEMs should resemble, except for the measurement of the 60 mm MCPHG sample at 60 kVp. After closer inspection of the scatter function (in Appendix C5), an abnormal right scatter fraction was observed. Since the estimation of the scatter function between the scatter fractions rely on the angle of the scatter fractions at the edge of the lead plate and at the edge of the collimator, this abnormal right scatter fraction was likely the cause for a bad estimation. It was therefore considered reasonable to consider this measurement as an outlier and exclude the measurement from the overall results. The median differences for the scatter magnitude (MSPR and EM) after exclusion of the outlier ranged between 0.84 (nylon/muscle) and 1.20 (PMMA/brain) and the IQR of the measurements ranged between 0.04 and 0.15. This means that the

absolute difference between all measured TEMs and simulated tissues was less than 3 percent, in terms of (normalized) intensity. The median differences for the spatial scatter distribution (SD) ranged from 0.92 (PMMA/Brain) to 0.98 (MCPHG/Bone). Based on these results, it can be concluded that the proposed TEMs are representative as the tissue they should resemble, in terms of scatter characteristics. The results also showed that the measured scatter magnitude (EM) of PMMA was slightly higher in comparison with the simulated EM of brain tissue. This result once again suggests that the widely used PMMA is potentially not an optimal material for the construction of phantoms for IQA.

Limitations and recommendations

There are several limitations in this work that should be improved in the future. Although the validation of the experimental setup using PMMA showed good results, the sample size of the current measurements were considered small. With such a small sample size it is difficult to form a conclusion regarding the reliability or to perform a sensitivity analysis about the accuracy of the measurements. Therefore, the validation should be extended by using a wider range of materials that are available in the material database (i.e. copper, water) to see whether the measurements are still in agreement with the simulations of the same material. It is also recommended to evaluate the scatter characteristics of materials that are commonly or commercially used for the construction of phantoms for IQA in CT and CBCT, when available, since the scatter characteristics of (most of) these materials are not yet evaluated in terms of both the scatter magnitude and spatial distribution.

6.5 CONCLUSIONS

In this chapter, the included TEMs were measured for their scatter characteristics, in terms of MSPR, EM and SD. The edge spread technique was a simple to implement technique for scatter measurement and EM and SD could be directly quantified using this technique. The MSPR was obtained based on an estimation, using a spline interpolation technique. The estimation of the MSPR proven to be valid, based on validation with measurements and Monte Carlo based simulations of PMMA. It is however recommended to investigate the accuracy of the estimated MSPR in future work (for example by increasing the sample size and by including more materials that are available in the database of the simulation tool for comparison) in order to make the results more reliable.

Overall, MCPH, nylon, SMP and MCPHG are all considered representative as bone, muscle, brain and bone equivalent material, respectively, since the median ratios result in a difference in scatter to primary ratio of less than 3 percent.

7

PROTOTYPE FABRICATION AND EVALUATION

7.1 INTRODUCTION

Two prototypes were fabricated for preliminary evaluation of the imaging characteristics and some practical aspects of the TEMs such as the suitability of the TEMs for the selected fabrication techniques and potential flaws in the design of the phantom. Also expert opinions were gathered regarding the design and usability of the phantom (representativeness of important anatomical landmarks and impact of image artifacts introduced by the phantom). Based on these findings, improvements were made for the final prototype of the phantom. The first prototype was fabricated in an early stage of the project, with the main purpose of investigating the practical aspects of the design and early measurements of the radiodensity of the selected TEMs for this prototype. The second prototype was fabricated in a late stage of the project, after implementing the points of improvements, based on the findings from the first prototype. In order to be time- and cost efficient, only a part of the phantom design (the anterior right side) was selected for the fabrication of the prototypes, because this part of the design contains a wide variation of anatomical landmarks (i.e. frontal sinus, ocular cavity) and each TEM of interest (i.e. bone, brain, CSF[4] and muscle equivalent material). The following sections in this chapter describe the steps that were taken for the fabrication of each prototype and discusses the results of the quantitative (radiodensity) and qualitative (anatomical landmarks and image artifacts) evaluation of the two prototypes.

7.2 MATERIALS AND METHODS

7.2.1 FABRICATION OF THE FIRST PROTOTYPE

The TEMs that were used for the fabrication of the first prototype are MCPH powder (de Bron B.V., Harderwijk, the Netherlands) as bone equivalent material and nylon (polyamide 12, Shapeways, Eindhoven, the Netherlands) as brain and muscle equivalent material. Initially, the skull was supposed to be fabricated by selective laser sintering of the MCPH powder. Unfortunately, the required equipment became unavailable during the project. For this reason, the MCPH powder was carefully poured into the space between the muscle shell and the brain model for initial testing after seaving out the bigger grains. The muscle shell and brain model (figure 7.1) were fabricated using an EOS P7 selective laser sintering (SLS) machine (Shapeways, Eindhoven, the Netherlands) and the open sides of the prototype were closed using PMMA plates that were cut into the shapes of these open sides.

Figure 7.1 – Muscle shell and brain model for the first prototype.MCPH powder was poured into the open area as bone equivalent material.

[4] CSF within the ventricles was not specifically evaluated in the radiodensity and scatter measurements because it is mainly a water-like substance. For the prototype, nylon was taken as ventricle/CSF substitute because the scatter characteristics of nylon are similar to water.

7.2.2 FABRICATION OF THE SECOND PROTOTYPE

The TEMs that were used for the fabrication of the second prototype are MCPHG (3.85 wt% MCPH, 60 wt% calcium sulfate and 36.15 wt% water) (de Bron B.V., Harderwijk, the Netherlands) as bone equivalent material, SMP-gel (Bison Polymax crystal express, Bolton adhesives, Rotterdam, the Netherlands) as brain equivalent material and nylon 12 (Shapeways, Eindhoven, the Netherlands) as muscle shell and ventricle material. Inserts for (low) contrast resolution and a part of the ventricles (also from nylon) were also incorporated into the brain area of the second prototype. The MCPHG skull was fabricated using silicone casting (Shore 15 silicone casting rubber, Polyestershoppen B.V., Moordrecht, the Netherlands), where a positive mold of the skull (two pieces) fused deposition modeling (FDM) printed (Ultimaker 2, Geldermalsen, the Netherlands) at the student workshop of the faculty of mechanical, maritime and materials engineering at Delft university of technology. The MCPHG mixture was stirred with intervals for approximately one hour in order to remove air bubbles that emerged during the hardening of the mixture, before being poured into the cast. The SMP-gel was injected into the cranial cavity of the skull using a silicone kit injector. The muscle shell was taken from the first prototype and attached to the casted MCPHG skull using SMP gel. The ventricles and low contrast inserts were fabricated using SLS (Shapeways, Eindhoven, the Netherlands) (figure 7.2a to f) and positioned within the SMP gel in the cranial cavity.

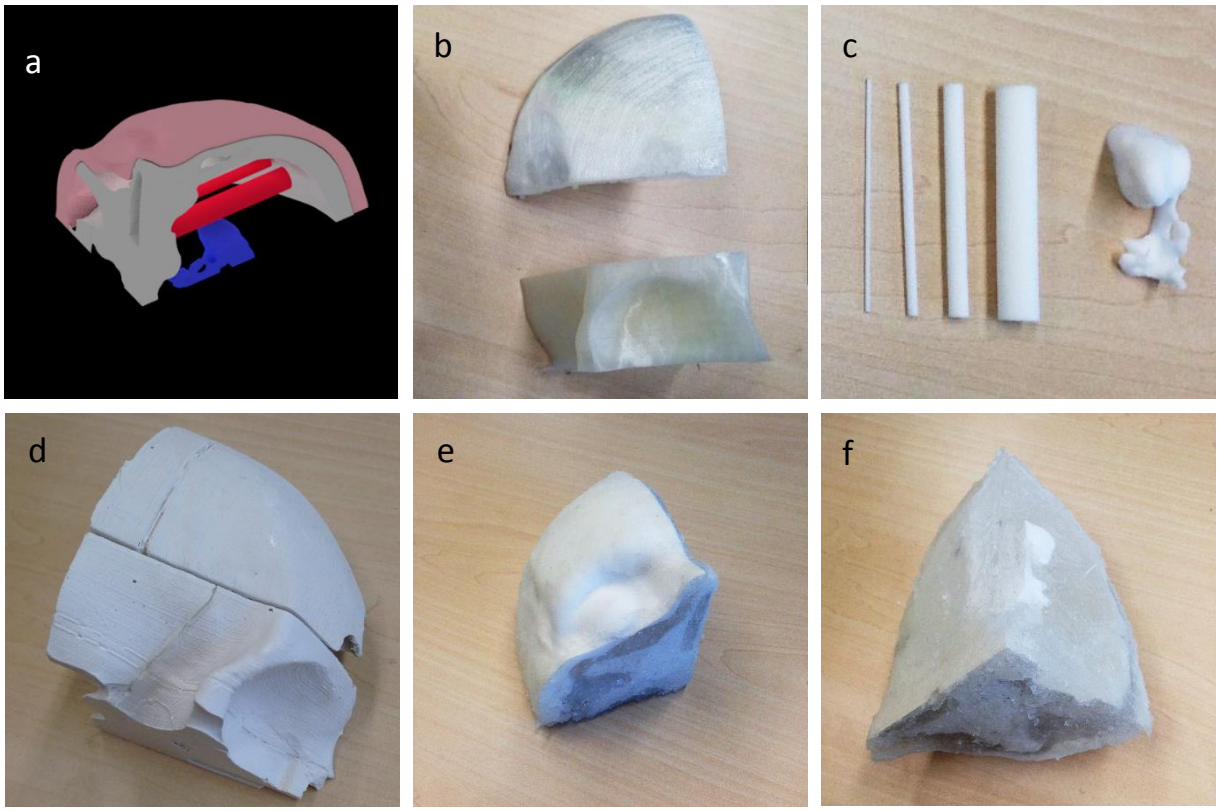

Figure 7.2 – Design and parts of the second prototype. A) Isometric view of the design with muscle shell (pink), skull (grey), inserts (red) and ventricles (blue). B) 3D printed skull mold. C) SLS fabricated nylon inserts. D) Silicone casted MCPHG skull. E and F) isometric view of finished prototype.

7.2.3 EVALUATION OF THE RADIODENSITY

Both prototypes were quantitatively evaluated in terms of the radiodensity (HU values), by comparing the TEMs with human tissues of the original CBCT data, using DviewX. The methodology of the measurement of the HU values was similar to the methodology from chapter 5 (assessing 10 points on 3 CBCT slices and calibrating the results with a calibration phantom). The measurements of the prototypes were calibrated using the calibration phantom, by calculating the HU bias and by checking for scaling effects. The measurements of the patient data could not be calibrated because during the data acquisition, no calibration phantom was positioned close to the head.

7.2.4 EVALUATION OF THE ANATOMICAL LANDMARKS AND IMAGE ARTIFACTS

The prototypes were also qualitatively compared with CBCT data using AixiaViewer (figure 7.3). The similarity of important anatomical landmarks of the skull (i.e. the frontal sinus and the ocular cavity) were evaluated from the anterior-posterior, lateral and axial view and noticeable differences between the prototype and patient data were noted. The prototypes were also evaluated for the presence of image artifacts. Examples of image artifacts that could result in a biased image quality assessment are the presence of air pockets and significant seams where these should not be present.

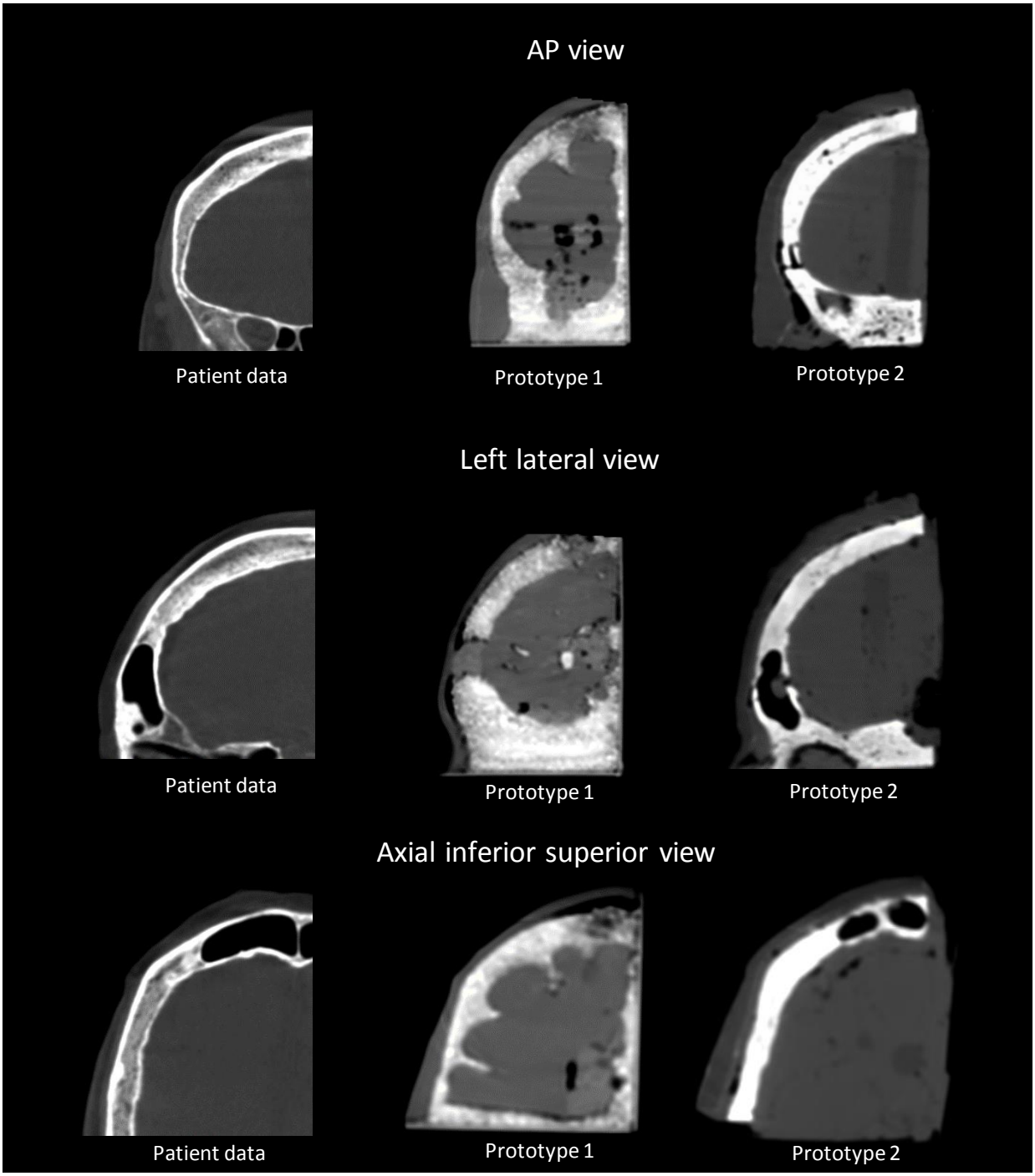

Figure 7.3 – CBCT slices of the anterior-posterior (AP) view (first row), left lateral view (second row) and axial inferior superior view (third row) of the patient data (first column), prototype 1 (second column) and prototype 2 (third column).

7.3 RESULTS

7.3.1 THE RADIODENSITY

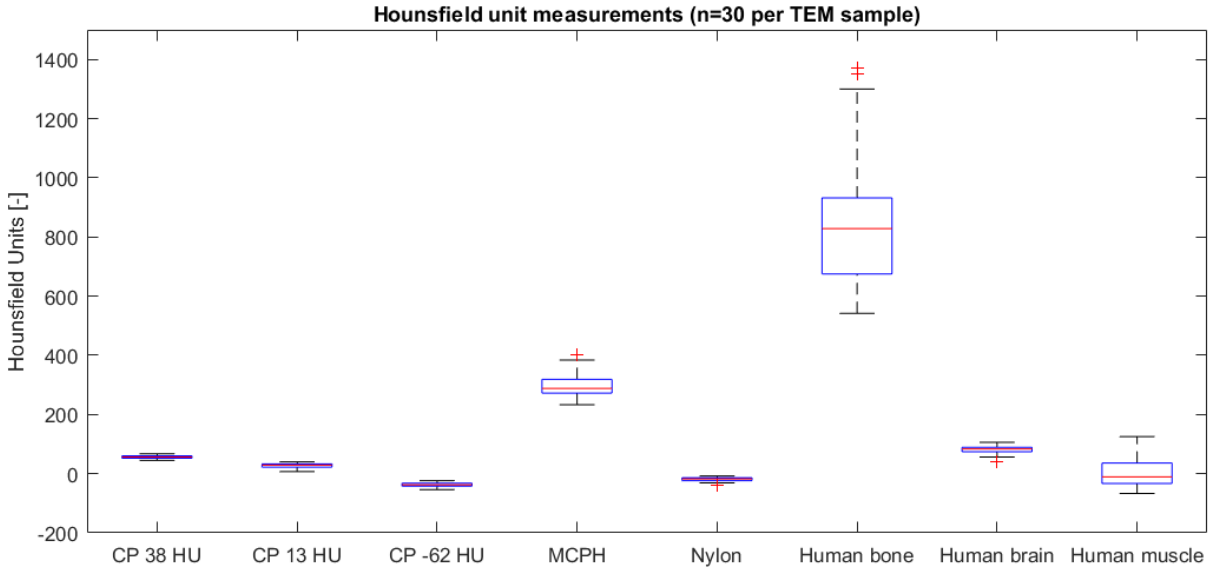

Figure 7.4 – Measured Hounsfield Units for the calibration phantom (CP) at three different HU levels, monocalcium phosphate (MCPH), nylon and human tissues.

Figure 7.4 and 7.5 are a summary of the HU measurements of the calibration phantom (CP), of the TEMs before calibration and of real tissues within the human head before calibration, for the first and second prototype respectively. The median HU value and the 25th (Q1) and 75th (Q3) percentile of the measurements are summarized in table 7.1.

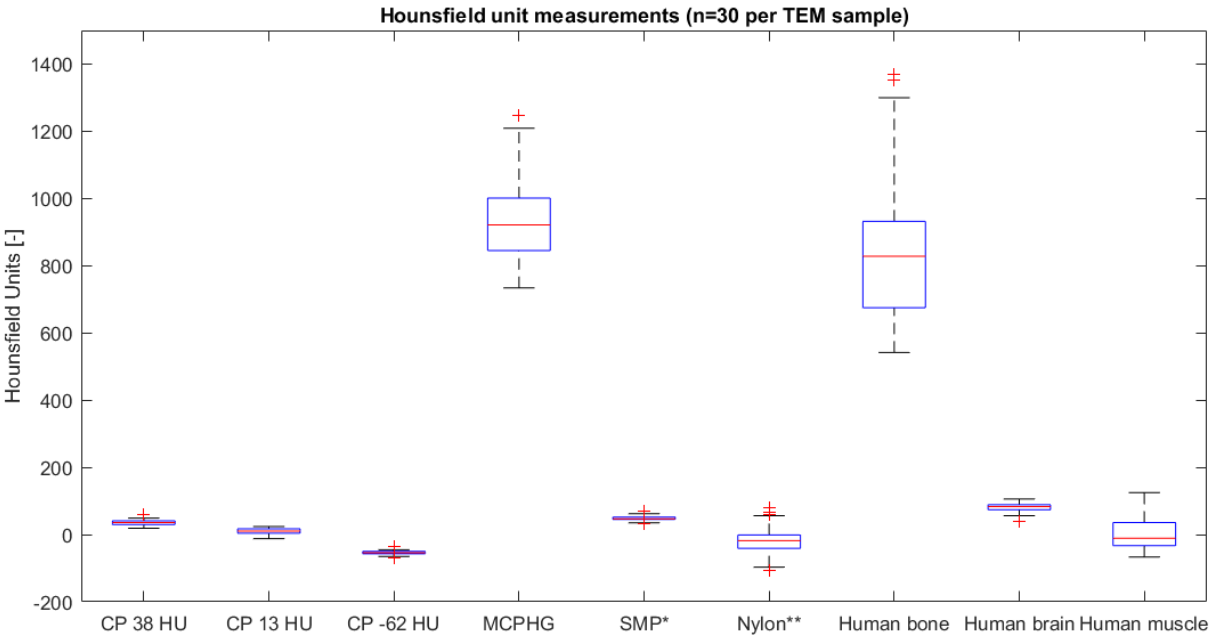

Figure 7.5 – measured Hounsfield Units for the calibration phantom (CP) at three different HU levels, monocalcium phosphate with gypsum (MCPHG), silyl modified polymer (SMP), nylon and human tissues.

Table 7.1 – Summary of radiodensity measurements for the first (left) and second prototype (right).

Material/tissue	Median	Q1	Q3
CP 38	56	51	60
CP 13	28	21	33
CP -62	-37	-42	-32
MCPH	286	259	314
nylon	-18	-24	-11
Bone tissue	820	651	912
Brain tissue	82	69	88
Muscle tissue	-6	-33	33
CP 38	56	51	60

Material/tissue	Median	Q1	Q3
CP 38	36	30	41
CP 13	11	4	17
CP -62	-54	-57	-50
MCPHG	922	845	1001
nylon	-18	-41	-1
SMP	47	45	52
Bone tissue	828	675	932
Brain tissue	84	74	89
Muscle tissue	-11	-33	36

7.3.2 ANATOMICAL SIMILARITY AND IMAGE ARTIFACTS

The image artifacts and several differences between the anatomical landmarks of the *first* prototype and of the patient that were observed by the author and experts are listed in table 7.2.

Table 7.2 – Image artifacts and differences between the first prototype and patient data.

Skull	Brain	Muscle
No distinction between trabecular and cortical bone	Large air pockets within the 3D printed brain	Homogeneous , whereas the muscle structure of a real patient is heterogeneous (adipose tissue and skeletal muscle)
No bone structure	Significantly smaller size of brain	
Minor air pockets throughout entire skull area	No ventricles	

The image artifacts and several differences between the anatomical landmarks of the *second* prototype and of the patient that were observed by the author and experts are listed in table 7.3.

Table 7.3 – Image artifacts and differences between the second prototype and patient data.

Skull	Brain	Muscle
No distinction between trabecular and cortical bone	Several air pockets within the brain area	Several air pockets between muscle shell and MCPHG skull
Minor air pockets throughout entire skull area		
Some regions in skull thicker (due to design)		

7.4 DISCUSSION

Radiodensity

The results that were obtained from the radiodensity (HU) measurements show that some significant improvements were made from the first design iteration to the second design iteration. The Hu value of both MCPH as bone equivalent material and nylon as brain equivalent material (from the first prototype) did not fall within the theoretical range of HU values for bone and brain tissue respectively. However, the HU values of the MCPHG and nylon fell well within the range of the theoretical HU values of bone and muscle/adipose tissue respectively. The SMP had a median HU value of 47, while the median HU value of the SMP measured in chapter 5 was 34. Nevertheless, the HU value of SMP was still within the range of the theoretical HU values of brain tissue. It is however of importance to further investigate what could have caused the difference in the measurements. What was particularly interesting was the fact that the IQR was relatively big for the measured MCPHG and nylon/SMP mixture used in the soft tissue shell, which was actually similar for the measured bone and muscle tissue for the patient data.

Qualitative evaluation

In the qualitative comparison between the prototypes and the patient data, some differences between the anatomy of the patient data and the prototypes were observed. Because the skull model of the first prototype was created by pouring MCPH grains into the prototype, it was obvious that the anatomical features were different compared to the anatomy of the patient data. In the second prototype, the anatomy of the skull was much more representative in comparison with the patient data, but there was no distinction between trabecular bone and cortical bone in the prototype. In theory, cortical bone is more dense compared to trabecular bone and thus may result into higher HU values and more scatter radiation. This phenomenon could be improved in future work, by incorporating separate trabecular and cortical bone layers into the design.

Some image artifacts that were introduced by the prototypes were also observed during the qualitative comparison between the prototypes and the patient data. The presence of air pockets was seen throughout the skull, brain and muscle area. For measurements of the image quality that include averaging over a specific region of the phantom, this could be an issue since the air pockets could result in a lower average HU value. Especially air pockets in the brain area should be avoided, by carefully injecting the SMP into the cranial cavity. Whether this can be done adequately for the final phantom can only be verified after the fabrication of the phantom. Some preliminary tests using a wider nozzle for the injection of the SMP showed that the amount of air pockets can be reduced significantly.

7.5 CONCLUSIONS

Prototypes of two design iterations were evaluated for practical aspects regarding the image quality and suitability for fabrication using the specified fabrication techniques. The first prototype had some significant drawbacks, such as an underattenuation of the bone and brain equivalent materials, bad resemblance of the anatomy of the human head and image artifacts that could influence the image assessment, such as air pockets. Therefore, the first prototype was not an improvement on existing phantoms. However, even though the prototype of the second design iterations showed several inconsistencies, compared to CBCT data of a patient, including the presence of small air pockets in the bone and brain equivalent material, the similarity of the anatomy and attenuation characteristics were highly representative. Also, with the addition of inserts for quantitative image quality assessment, this prototype can be considered as a cost efficient and improved alternative for commercial phantoms that are currently widely used for image quality assessment in (cone beam) CT.

8

OVERALL DISCUSSION

The goal of this study was to develop an anthropomorphic head phantom for quantitative image quality assessment in (cone beam) computed tomography. From a previously performed literature, it became clear that the TEMs of commonly used commercial phantoms for image quality assessment in CT or CBCT show an underattenuation in the diagnostic x-ray energy range and the scatter characteristics of these TEMs were not explicitly validated. Many commercial phantoms also lacked inserts for quantitative image quality assessment, such as inserts for the assessment of the contrast and spatial resolution of the CBCT image. Furthermore, commercial phantoms are relatively expensive and a wide adoption of these phantoms is therefore limited. Critical requirements for this study were therefore (1) having a realistic anatomy, (2) having representative attenuation characteristics in comparison with tissues in the human head and (3) contain inserts that can be used for the quantification of the (low) contrast resolution and spatial resolution of the (enhanced) CBCT image. Additionally, the desire was to achieve this goal with TEMs that allow for 'home made' fabrication methods in order to make phantoms more cost efficient and therefore more accessible for researchers.

The following (major) steps were taken in order to achieve the desired goal: First a 3D mesh model of the phantom was designed, based on CBCT data of an anonymous male patient. Then a selection of TEMs, based on theory from the literature were evaluated for their radiodensity. Additionally, the same TEMs were evaluated for their scatter characteristics, using the edge spread technique for scatter quantification. Finally, a prototype was fabricated to evaluate practical aspects of the included TEMs in this study, by quantitatively comparing the imaging properties (radiodensity and image artifacts) of these TEMs within the prototype with CBCT data of the male patient and by qualitatively evaluating the prototypes for the similarity of the anatomy and image artifacts. Whether the goals of this study are met using this approach and limitations of this approach are discussed in this chapter. Based on this discussion, recommendations for future work are provided.

CBCT based design and similarity of the anatomy

The phantom was designed by creating a CBCT data based model of a human head, where important and relevant tissue types for IQA in CBCT (bone, brain, muscle and CSF) were separated into different meshes by adjusting the threshold level of the voxels from the CBCT data. These data were then manually edited and made compatible for 3D printing. While the muscle and brain layer remained similar to the anatomy of the CBCT data after editing, the skull was manually adjusted, by removing natural cavities that could not be fabricated using 3D printing and by increasing the thickness of some weak anatomical features in the maxillofacial region of the skull. These adjusted in the skull areas might lead to more scatter radiation compared a real skull, since the thickness and the geometry of a material can influence the scatter characteristics. However, these adjustments are necessary in order to sustain forces and stress that occur during (normal) usage of the phantom. Furthermore, in reality, the human skull varies in thickness and geometry, depending on the gender, age and ethnicity, which may also lead to different scatter characteristics. Therefore, this design is considered valid to be used for the construction of the phantom.

The radiodensity of the TEMs

The theoretical HU values of the TEMs were compared with HU values that were measured using the Allura FD20 CBCT system. After calibration of the measurements, several differences between the theoretical values and the measured values were observed: The measured HU values of MCPH and MCPHG were significantly lower than the theoretical HU values for these materials respectively. The median HU values were 302 (IQR = 70) and 897 (IQR = 126) for MCPH and MCPHG respectively (the theoretical HU values were 1275 and 1398 for MCPH and MCPHG respectively). This can be explained by the fact that the calculation of HU values within a volume are based on the intensity of each voxel within that volume. Because of the presence of air in the MCPH and MCPHG samples, the averaging intensity of a voxel containing both material and air could result in these low values. However, while MCPH fell outside the range for common HU values of bone tissue, MCPHG was still within this range and therefore MCPHG was considered as representative bone equivalent material in terms of radiodensity.

The measured values for nylon were also slightly below the theoretical HU value of nylon. The median HU value was -29 (IQR = 10), instead of the calculated 1 HU. This could be explained by the fact that there are many different types of nylon polymers and the calculation of the theoretical HU value for nylon was based on one specific type of nylon (PA12). Even though the measured HU values of nylon were slightly lower than the theoretical HU values of muscle tissue, nylon was still considered as a suitable muscle equivalent material, because in reality, the 'soft tissue' layer of the human head surrounding the skull does not only consist of smooth muscle, but also of adipose (fat) tissue. Adipose tissue has low HU values of -100 to -50. The measured HU values of nylon fall within the range of the average of muscle and adipose tissue.

The measured HU values of SMP were slightly higher compared with the theoretical HU values of SMP. The median HU value was 34 (IQR = 11) whereas the theoretical HU value for SMP was 27. However, the measured HU value of SMP are within the range of HU values for brain tissue and can therefore be considered as a representative brain equivalent material (taken into account that there was no distinction made between white and grey matter). It should be noted that the SMP samples contained (relatively large and visible) air pockets. During injection of the SMP into the cranial cavity, these air pockets should be minimized, by using a wide nozzle injector for the injection.

The HU values of the TEMs were also measured after implementation into a prototype of the phantom. The measured HU values of MCPHG and nylon were similar to the HU values of the HU measurement using the TEM samples. However, the measured HU values of SMP were found to be higher in the prototype, compared to the HU values of the SMP sample. In future work, the cause of these differences should be investigated, to see whether the material shows inconsistencies or whether the methodology used for the radiodensity measurements were insufficient.

Overall, the HU values of MCPHG, SMP and nylon all fell within the theoretical range of HU values for bone, brain and muscle tissue respectively and can therefore be considered as suitable TEMs in terms of radiodensity.

The scatter characteristics of the TEMs

The scatter characteristics of the TEMs were measured using the edge spread technique for scatter quantification. In a comparison with alternative techniques for the measurement of scatter radiation, the edge spread technique was considered the most suitable technique for in this study since the implementation into the available experimental setup was relatively easy and the scatter magnitude and scatter distribution could be directly measured using this technique. The scatter magnitude at the edge of the lead plate (EM) and the scatter distribution (SD) were evaluated using a modified setup of the Allura FD20 CBCT system, by positioning a lead plate in front of the detector to block a part of the

x-ray beam and by removing the anti-scatter grid that was positioned in front of the detector. The max scatter to primary ratio (MSPR) was estimated using a spline interpolation technique. The EM, SD and MSPR of MCPH, nylon, SMP and MCPHG were then compared with Monte Carlo based scatter simulations of bone, muscle, brain and bone tissue respectively.

Based on the comparison between the measurements of the TEMs and the simulations the different tissue types, MCPH, SMP and MCPHG can all be considered as very similar to bone, brain and bone equivalent materials respectively, in terms of MSPR. The median ratios between the measurements of these TEMs and simulations were between 0.95 and 1.08. This means that for TEMs of up to 60 mm thickness, there is only a maximal difference of less than 2 percent in terms of MSPR, compared to the simulated tissues. The median ratio between the measured MSPR of nylon and simulated MSPR of muscle tissue was slightly lower (0.87). However, this means that there is only a maximal difference of less than 3 percent in terms of MSPR, so nylon was still considered as representative muscle equivalent material.

The EM of nylon was considered similar to the EM of muscle tissue, since the median ratio was 1.04. The median ratio of the measured EM of MCPH, SMP and MCPHG were slightly higher compared to the simulated EM of bone, brain and bone tissue respectively, between 1.12 and 1.17. However, these differences would only result in less than 2 percent absolute differences in the scatter to primary ratio (since the EM of the measurements were all under 10 percent), so MCPH, nylon, SMP and MCPHG were all considered as representative bone, muscle, brain and bone equivalent materials respectively, in terms of EM.

The median ratio between the measured SD of the TEMs and the simulated tissues were all between 0.92 and 1.00 and were considered as similar to each other.

Limitations of this study and recommendations for future work

There are several aspects of this study that could be improved in future work. The scatter characteristics of MCPH were based on MCPH grains, whereas the initial concept was to fabricate a solid 3D model from these MCPH grains using selective laser sintering. The attenuations should be evaluated again if MCPH is fabricated with selective laser sintering techniques in the future. Also, the scatter measurements and estimation using the spline fitting technique were only verified by comparing measurements of PMMA with Monte Carlo based simulations of PMMA. While this verification provided good results, it is still recommended to perform the verification with a larger sample size and with more materials that are available in the database of the simulation tool. This can result in a higher reliability, especially for the estimated MSPR values. Another drawback of the scatter measurement with the current experimental setup is that only one side of the x-ray beam radiating the TEM was blocked with a lead plate, whereas the other side was blocked using built in collimators. The results of the measurements have shown that the collimator introduced leakage of radiation, which ultimately can lead in accuracies during the estimation of the scatter function. It is therefore recommended to perform scatter measurements with two lead plates blocking both sides of the x-ray beam radiating the TEM. Because a limited range of TEMs were evaluated in this study, optimizations are still possible. It is therefore recommended to investigate the attenuation characteristics of novel materials in the future, using the same methodology as in this study in order to find materials that are easier to work with or have better attenuation characteristics than the current ones used. Especially materials that do not introduce air bubbles in the phantom are potentially good substitutes for the currently used materials.

9

FINAL CONCLUSIONS

The goal of this study was to develop an anthropomorphic head phantom with realistic attenuation characteristics and inserts for quantitative image quality assessment in cone beam computed tomography. As an addition to these requirements, the desire was to use TEMs that are suitable for simple 'home made' fabrication methods such as silicone casting and 3D in order to make the design more affordable and accessible for researchers, since commercial phantoms are relatively expensive.

By looking back at all aspects of this study, from the design of the phantom using CBCT data, to the evaluation of the TEMs in terms of radiodensity and scatter characteristics, to the construction of the prototype, the goal of creating such a phantom can be considered achieved in a large extent. The radiodensity of the TEMs fell well within the theoretical range of radiodensity for human tissues.

Differently to other works, the scatter characteristics of the TEMs were explicitly evaluated in terms of magnitude and the spatial distribution of the scatter radiation. The ratio between the measured scatter characteristics of the TEMs and simulated scatter characteristics of human tissue did not differ significantly for MCPH, SMP and MCPHG compared to bone, brain and bone tissue respectively. The scatter characteristics of nylon were somewhat different compared to the scatter characteristics of muscle tissue, but these differences result in only a 3 percent difference in scatter to primary ratio.

Evaluation of prototypes has shown that it is feasible to fabricate a head phantom for quantitative IQA in CBCT using selected TEMs that are suitable for 'home made' fabrication techniques, which makes this design affordable and easy to adopt as an alternative for commercial anthropomorphic head phantoms.

10

BIBLIOGRAPHY

[1] T. M. Buzug, "Computed Tomography," p. 526, 2008.

[2] J. Wiegert, "Scattered radiation in cone-beam computed tomography : analysis , quantification and compensation," p. 232, 2007.

[3] J. A. Edlow, "Diagnosis of Subarachnoid Hemorrhage," *Neurocrit Care*, vol. 2, no. 1, pp. 99–109, 2005.

[4] F. E. Boas and D. Fleischmann, "CT artifacts: causes and reduction techniques," *Imaging Med.*, vol. 4, no. 2, pp. 229–240, 2012.

[5] K. P. Maher and J. F. Malone, "Computerized scatter correction in diagnostic radiology," *Contemp. Phys.*, vol. 38, no. 2, pp. 131–148, 1997.

[6] H. Gao, R. Fahrig, N. R. Bennett, M. Sun, J. Star-Lack, and L. Zhu, "Scatter correction method for x-ray CT using primary modulation: phantom studies," *Med. Phys.*, vol. 37, no. 12, pp. 934–946, 2010.

[7] M. Baer and M. Kachelrieß, "Hybrid scatter correction for CT imaging," *Phys. Med. Biol.*, vol. 57, no. 21, pp. 6849–6867, 2012.

[8] Y. Kyriakou, M. Meyer, and W. A. Kalender, "Towards quantitative flat-detector CT using advanced scatter correction," *IFMBE Proc.*, vol. 25, no. 2, pp. 390–393, 2009.

[9] A. Sossin, V. Rebuffel, J. Tabary, J. M. Létang, N. Freud, and L. Verger, "A novel scatter separation method for multi-energy x-ray imaging," *Phys. Med. Biol.*, vol. 61, no. 12, p. 4711, 2016.

[10] H. Hirayama, "Lecture Note on photon interactions and cross sections. 2000," *KEK Intern.*, no. November, 2000.

[11] J. H. Hubbell, "Review and history of photon cross section calculations.," *Phys. Med. Biol.*, vol. 51, no. 13, pp. R245–R262, 2006.

[12] M. J. Berger, J. H. Hubbell, S. M. Seltzer, J. Chang, J. S. Coursey, R. Sukumar, D. S. Zucker, and K. Olsen, "XCOM: Photon Cross Sections Database," *National Institute of Standards and Technology*, 1998. [Online]. Available: http://physics.nist.gov/PhysRefData/Xcom/Text/version.shtml. [Accessed: 10-Nov-2016].

[13] K. S. Mann, M. Kurudirek, and G. S. Sidhu, "Verification of dosimetric materials to be used as tissue-substitutes in radiological diagnosis," *Appl. Radiat. Isot.*, vol. 70, no. 4, pp. 681–691, 2012.

[14] D. N. Irani, *Properties and Composition of Normal Cerebrospinal Fluid*, First Edit. Elsevier Inc., 2009.

[15] Y. Wang, "Anthropomorphic head phantoms for quantitative image quality assessment in cone beam computed tomography: a literature study about state of the art phantom tools and tissue equivalent materials," 2017.

[16] ICRU, “Tissue substitutes in radiation dosimetry and measurement (report 44),” Bethesda, MD, 1989.

[17] N. C. Yang, P. K. Leichner, and W. G. Hawkins, “Effective atomic numbers for low-energy total photon interactions in human tissues.,” *Med. Phys.*, vol. 14, no. 5, pp. 759–766, 2008.

[18] P. C. Shrimpton, B. F. Wall, and E. S. Fisher, “The tissue-equivalence of the Alderson Rando anthropomorphic phantom for x-rays of diagnostic qualities.,” *Phys. Med. Biol.*, vol. 26, no. 1, pp. 133–139, 1981.

[19] C. B. Chiarot, J. H. Siewerdsen, T. Haycocks, D. J. Moseley, and D. A. Jaffray, “An innovative phantom for quantitative and qualitative investigation of advanced x-ray imaging technologies,” *Phys. Med. Biol.*, vol. 50, no. 21, pp. N287–N297, 2005.

[20] Computerized Imaging Reference Systems, “Dental & Diagnostic Head,” no. 800, pp. 37–38.

[21] Radiology Support Devices, “Angiographic Head Phantoms.” RSD Alderson, Long beach, CA 90810, pp. 30–31.

[22] Kyoto Kagaku, “Angiographic CT Head Phantom ACS.” Kyoto.

[23] J. F. Winslow, D. E. Hyer, R. F. Fisher, C. J. Tien, and D. E. Hintenlang, “Construction of anthropomorphic phantoms for use in dosimetry studies,” *J. Appl. Clin. Med. Physics; Vol 10, No 3*, Aug. 2009.

[24] QRM GmbH - Quality Assurance in Radiology and Medicine, “The semianthropomorphic head phantom.” [Online]. Available: http://www.qrm.de/content/products/anthropomorphic/sahp.htm. [Accessed: 14-Nov-2016].

[25] A. Sisniega, W. Zbijewski, J. Xu, H. Dang, J. W. . Stayman, J. Yorkston, N. Aygun, V. Koliatsos, and J. H. Siewerdsen, “High-fidelity artifact correction for cone-beam CT imaging of the brain,” *Phys. Med. Biol.*, vol. 60, no. 4, pp. 1415–1439, 2015.

[26] Embodi3d, “STL Files for 3D Printable Brain Model with Alzheimers Disease - Brain and nervous system - embodi3D.com.” [Online]. Available: https://www.embodi3d.com/files/file/6365-stl-files-for-3d-printable-brain-model-with-alzheimers-disease/. [Accessed: 09-Dec-2016].

[27] P. Akhlaghi, H. Miri Hakimabad, and L. Rafat Motavalli, “Determination of tissue equivalent materials of a physical 8-year-old phantom for use in computed tomography,” *Radiat. Phys. Chem.*, vol. 112, pp. 169–176, 2015.

[28] V. P. Singh, N. M. Badiger, and N. Kucuk, “Determination of Effective Atomic Numbers Using Different Methods for Some Low- Z Materials,” *J. Nucl. Chem.*, vol. 2014, pp. 1–7, 2014.

[29] R. E. Ximenes, A. Silva, D. Balbino, M. E. Poletti, and A. F. Maia, “Development of an anthropomorphic head phantom using dolomite and polymethyl methacrylate for dosimetry in computed tomography,” *Radiat. Phys. Chem.*, vol. 117, pp. 203–208, 2015.

[30] R. R. Gallas, N. Hünemohr, A. Runz, N. I. Niebuhr, O. Jäkel, and S. Greilich, “An anthropomorphic multimodality (CT/MRI) head phantom prototype for end-to-end tests in ion radiotherapy,” *Z. Med. Phys.*, vol. 25, no. 4, pp. 391–399, 2015.

[31] A. K. Jones, D. E. Hintenlang, and W. E. Bolch, “Tissue-equivalent materials for construction of tomographic dosimetry phantoms in pediatric radiology.,” *Med. Phys.*, vol. 30, no. 8, pp. 2072–2081, 2003.

[32] D. Bor, E. Unal, and A. Uslu, “Comparison of different phantoms used in digital diagnostic

imaging," *Nucl. Instruments Methods Phys. Res. Sect. A Accel. Spectrometers, Detect. Assoc. Equip.*, vol. 795, pp. 160–166, 2015.

[33] C. C. Ferreira, R. E. M. Ximenes Filho, J. W. Vieira, A. Tomal, M. E. Poletti, C. A. B. Garcia, and A. F. Maia, "Evaluation of tissue-equivalent materials to be used as human brain tissue substitute in dosimetry for diagnostic radiology," *Nucl. Instruments Methods Phys. Res. Sect. B Beam Interact. with Mater. Atoms*, vol. 268, no. 16, pp. 2515–2521, 2010.

[34] V. Singh and N. Badiger, "Effective atomic numbers of some tissue substitutes by different methods: A comparative study," *J. Med. Phys.*, vol. 39, no. 1, p. 24, 2014.

[35] K. P. Hermann, L. Geworski, T. Hatzky, R. Lietz, and D. Harder, "Muscle- and fat-equivalent polyethylene-based phantom materials for x-ray dosimetry at tube voltages below 100 kV.," *Phys. Med. Biol.*, vol. 31, no. 9, pp. 1041–6, 1986.

[36] M. E. Poletti, O. D. Gonçalves, and I. Mazzaro, "Measurements of X-ray scatter signatures for some tissue-equivalent materials," *Nucl. Instruments Methods Phys. Res. Sect. B Beam Interact. with Mater. Atoms*, vol. 213, pp. 595–598, 2004.

[37] P. Akhlaghi, H. Miri Hakimabad, and L. Rafat Motavalli, "Determination of tissue equivalent materials of a physical 8-year-old phantom for use in computed tomography," *Radiat. Phys. Chem.*, vol. 112, pp. 169–176, 2015.

[38] J. A. Inzana, D. Olvera, S. M. Fuller, J. P. Kelly, O. A. Graeve, E. M. Schwarz, S. L. Kates, and H. A. Awad, "3D printing of composite calcium phosphate and collagen scaffolds for bone regeneration," *Biomaterials*, vol. 35, no. 13, pp. 4026–4034, 2014.

[39] L. Duddleston, "Polyamide (Nylon) 12 Powder Degradation During The Selective Laser Sintering Process," 2015.

[40] Madehow, "How acrylic plastic is made - material, making, used, processing, parts, Raw Materials." [Online]. Available: http://www.madehow.com/Volume-2/Acrylic-Plastic.html. [Accessed: 13-Jan-2017].

[41] T. Razi, M. Niknami, and F. Alavi Ghazani, "Relationship between Hounsfield Unit in CT Scan and Gray Scale in CBCT.," *J. Dent. Res. Dent. Clin. Dent. Prospects*, vol. 8, no. 2, pp. 107–10, 2014.

[42] M. E. Poletti, O. D. Gonçalves, H. Schechter, and I. Mazzaro, "Precise evaluation of elastic differential scattering cross-sections and their uncertainties in X-ray scattering experiments," *Nucl. Instruments Methods Phys. Res. Sect. B Beam Interact. with Mater. Atoms*, vol. 187, no. 4, pp. 437–446, 2002.

[43] W. Geraldelli, A. Tomal, and M. E. Poletti, "Characterization of tissue-equivalent materials through measurements of the linear attenuation coefficient and scattering profiles obtained With Polyenergetic Beams," *IEEE Trans. Nucl. Sci.*, vol. 60, no. 2, pp. 566–571, 2013.

[44] V. N. Cooper, J. M. Boone, J. a Seibert, and C. J. Pellot-Barakat, "An edge spread technique for measurement of the scatter-to-primary ratio in mammography.," *Med. Phys.*, vol. 27, no. 5, pp. 845–853, 2000.

[45] D. Lazos and J. F. Williamson, "Impact of flat panel-imager veiling glare on scatter-estimation accuracy and image quality of a commercial on-board cone-beam CT imaging system," *Med. Phys.*, vol. 39, no. 9, p. 5639, 2012.

[46] E. Hofmann, M. Schmid, M. Lell, and U. Hirschfelder, "Cone beam computed tomography and low-dose multislice computed tomography in orthodontics and dentistry: a comparative

evaluation on image quality and radiation exposure.," *J. Orofac. Orthop.*, vol. 75, no. 5, pp. 384–98, 2014.

[47] U. V. Elstrøm, L. P. Muren, J. B. B. Petersen, and C. Grau, "Evaluation of image quality for different kV cone-beam CT acquisition and reconstruction methods in the head and neck region," *Acta Oncol. (Madr).*, vol. 50, no. 6, pp. 908–917, 2011.

[48] P. H. Kraus, M., Fischer, E., Gebhard, F., Richter, "Image quality and effective dose of a robotic flat panel 3D C-arm vc computed tomography," *Int. J. Med. Robot.*, vol. 7, no. April, pp. 375–392, 2015.

[49] Computerized Imaging Reference Systems, "Tissue Simulation and Phantom Technology." Norfolk, Virginia 23513, p. 20, 2013.

[50] "Philips Allura Xper FD10." [Online]. Available: http://www.philips.nl/healthcare/product/HC722024CA/allura-xper-fd10-10-biplane-cardiovascular-x-ray-system. [Accessed: 12-Nov-2016].

[51] Advanced dentistry, "Cone Beam CT - Dentist Middletown NJ - Dentist Red Bank NJ - DrKorwin.com," 2015. [Online]. Available: http://www.drkorwin.com/blog/cone-beam-ct. [Accessed: 12-Nov-2016].

[52] M. Söderman, D. Babic, S. Holmin, and T. Andersson, "Brain imaging with a flat detector C-arm: Technique and clinical interest of XperCT," *Neuroradiology*, vol. 50, no. 10, pp. 863–868, 2008.

[53] J. A. Seibert and J. M. Boone, "X-ray imaging physics for nuclear medicine technologists. Part 2: X-ray interactions and image formation.," *J. Nucl. Med. Technol.*, vol. 33, no. 1, pp. 3–18, 2005.

[54] Quality Assurance in Radiology and Medicine, "ConeBeam Phantom." Moehrendorf, Germany.

[55] S. Gonzalez, "x ray – Attenuation: Photoelectric effect, Compton scatter, Coherent scatter," 2012. [Online]. Available: http://drgstoothpix.com/tag/x-ray/. [Accessed: 12-Nov-2016].

[56] T. Winslow, "Paranasal cavities," 2012. [Online]. Available: https://www.cancer.gov/types/head-and-neck/patient/paranasal-sinus-treatment-pdq. [Accessed: 12-May-2016].

[57] S. Bose, S. Vahabzadeh, and A. Bandyopadhyay, "Bone tissue engineering using 3D printing," *Mater. Today*, vol. 16, no. 12, pp. 496–504, 2013.

[58] L. Ryan and R. Norris, *Cambridge international AS and A level Chemistry*, 3rd ed. Cambridge: Cambridge university press.

[59] K. Schörner, M. Goldammer, and J. Stephan, "Comparison between beam-stop and beam-hole array scatter correction techniques for industrial X-ray cone-beam CT," vol. 269, pp. 292–299, 2011.

[60] V. N. Cooper, J. M. Boone, J. a Seibert, and C. J. Pellot-Barakat, "An edge spread technique for measurement of the scatter-to-primary ratio in mammography.," *Med. Phys.*, vol. 27, no. 5, pp. 845–853, 2000.

11

APPENDIX

A DESCRIPTION OF ANTHROPOMORPHIC HEAD PHANTOMS[5]

The overview and description of anthropomorphic head phantoms for image quality assessment in (cone beam) CT was obtained directly from a previously performed literature study.

A1 THE RANDO-ALDERSON PHANTOM

One of the most popular phantoms for (image) quality assurance is the Rando Alderson phantom (RSD phantoms, Long Beach, CA 90810 USA) (figure A1). For example, [46]–[48], have used this phantom for IQA purposes. The phantom is equipped with a standard 5-step wedge and a 2-10 line pair/mm test pattern is optional [21]. What should be noted is that the wedge and test pattern are located axially in the neck of the phantom. This means that these two inserts can only be used in angiographic imaging and not for IQA in CT. In the brain, a high contrast blood vessel group is situated. According to the manufacturer, this phantom consists of tissue equivalent material with a male skull. However, [18] has shown that the tissue-equivalence only holds for therapeutic energy ranges of mega electron volts. When the energy level is under 90 keV, a noticeable underattenuation of the tissue is present.

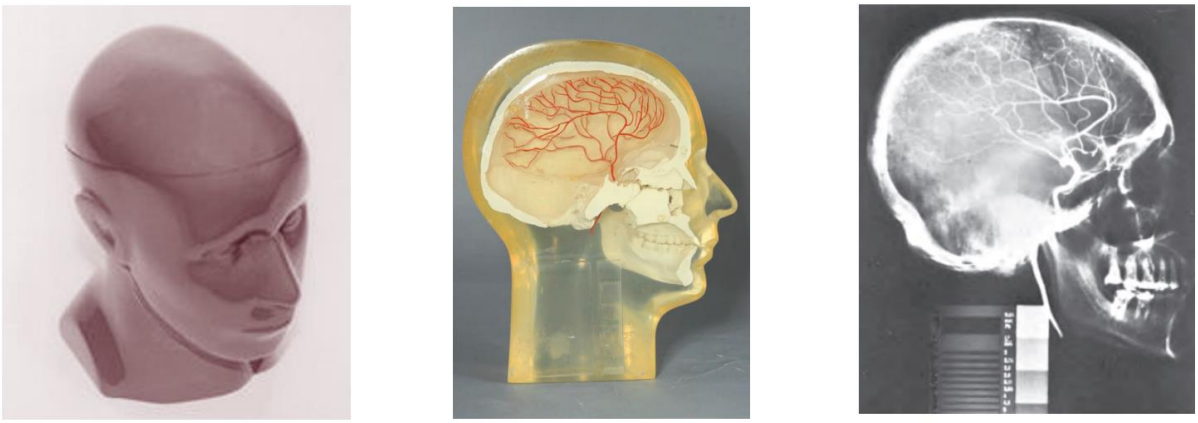

Figure A1 – The anthropomorphic head phantom by Rando-Alderson (RSD phantoms, Long Beach, CA 90810 USA). The phantom can optionally contain a step wedge and line pairs for angiographic image quality assessment. Adopted from [21]

A2 ATOM MAX PHANTOM BY CIRS

The 711-HN dental and diagnostic head phantom (Computerized Imaging Reference Systems, Norfolk, Virginia 23513 USA) (figure A2) is intended for monitoring, training and IQA in both dental cone beam as well as regular cone beam CT procedures [20]. The phantom contains several anatomical features, including a brain, sinus, nasal cavities, detailed bone structures (cortical and trabecular), neck vertebrae (C1-C7) and detailed teeth (dentine, enamel and root structure) [49]. However, there are no standard inserts for the measurement of the contrast resolution and the spatial resolution present. Furthermore, although the manufacturer claims that the phantom is made of representative tissue

[5] Appendix A was directly adopted from a previously performed literature study [15].

equivalent material for energy ranges between 50 keV and 25 MeV, the linear attenuation coefficient varies a lot within this energy range, so it is doubtful that this claim is true.

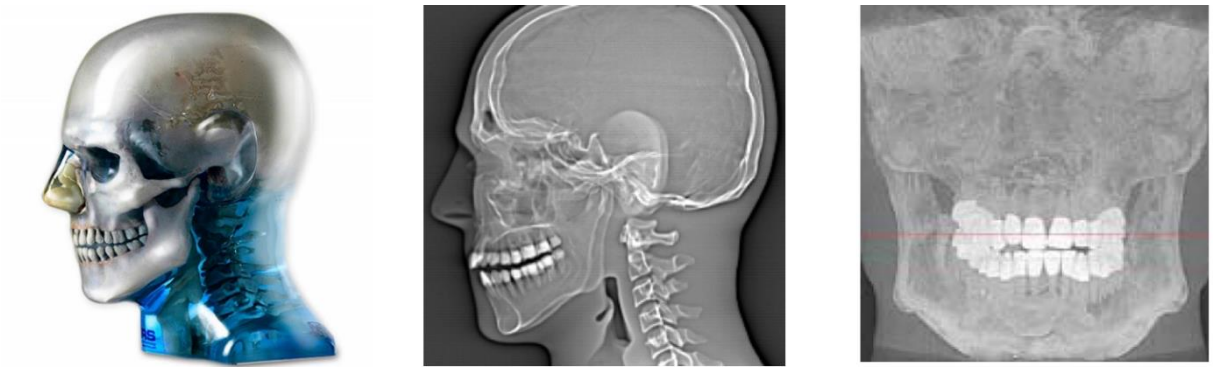

Figure A2 – The Atom Max phantom by CIRS (Computerized Imaging Reference Systems, Norfolk, Virginia 23513 USA). The Atom Max phantom can be used for qualitative image quality assessment. Adopted from [49]

A3 ACS PHANTOM BY KYOTO KAGAKU

The ACS angiographic phantom (Kyoto Kagaku, Kyoto, Japan) (figure A3) contains a soft tissue shell, eyes, detailed brain and neck vertebrae (C1-C7). The left half of the brain contains arteries, filled with contrast medium. Like the CIRS phantom, the ACS phantom does not have IQA inserts. The materials that were used have similar absorption characteristics compared to the human tissue type that is being simulated. The soft tissue shell and eye balls have a CT-number of 0 and the brain has a CT-value of 40 [22]. However, nothing was mentioned in terms of scatter properties by the manufacturer.

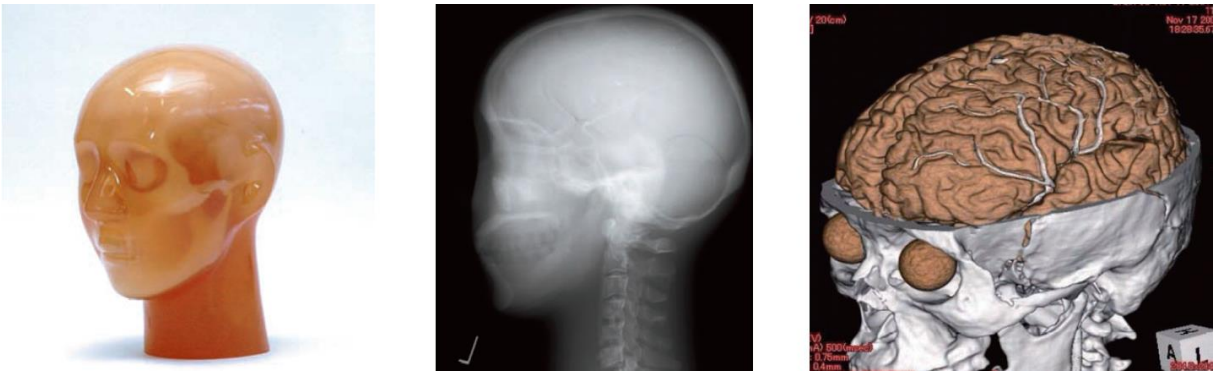

Figure A3 – The ACS angiographic head phantom by Kyoto Kagaku (Kyoto Kagaku, Kyoto, Japan). The ACS phantom contains high contrast blood vessels and can be used for qualitative image quality assessment. Adopted from [22]

A4 SEMI-ANTHROPOMORPHIC HEAD PHANTOM BY QRM

The semi-anthropomorphic head phantom by QRM (Quality Assurance in Radiology and Medicine, Moehrendorf, Germany) (figure A4) was designed for image quality assessment for CT. The inside of the phantom contains tissue equivalent material and inserts for quantitative IQA can be positioned at the location of the brain. The outside of this phantom, which has to represent the skull, is composed of simplified shapes of the human skull [24]. The material that was used for the skull was not specified by the manufacturer.

Figure A4 – The Semi-Anthropomorphic head phantom by QRM (Quality Assurance in Radiology and Medicine, Moehrendorf, Germany). The brain compartment of this phantom can possibly be replaces with an insert for quantitative image quality assessment. Adopted from [24]

A5 A MODIFIED RANDO-ALDERSON PHANTOM

Even though the commercially available phantoms are not very suitable for quantitative IQA purposes (because of the lack of IQA metrics for example), they are still widely used by researchers due to the lack of better alternatives. Some researchers have developed custom phantoms to make them more suitable for quantitative IQA, by adding inserts. For example [25] used a Rando-Alderson phantom as basis and added inserts for low contrast resolution into the skull (figure A5) (the phantom was modified by the phantom laboratory). Even though such modifications are an improvement on the unmodified phantoms, the material of the phantom is still the same as from the original Rando-Alderson phantom. Therefore, the tissue equivalence, and more importantly, the scatter characteristics of such phantoms remain questionable. Furthermore, by opening the original phantom, unwanted image artifacts such as black lines cause by air are created.

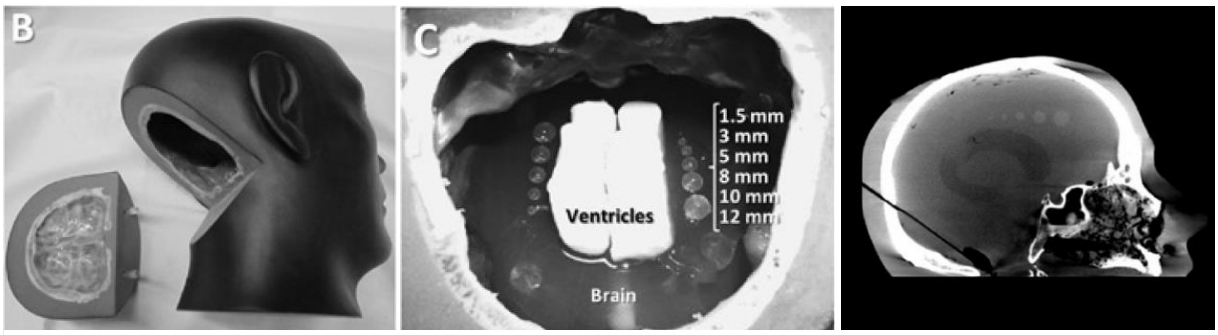

Figure A5 – A modified Rando-Alderson phantom (modified by the Phantom Laboratory, as requested by). Low contrast resolution inserts and ventricles have been added in order to provide the possibility for quantitative image quality assessment. Adopted and modified from [25]

A6 NEWLY DEVELOPED BY CHIAROT

Another phantom that was designed specifically for quantitative IQA was presented by [19]. This phantom represents the human from the head to the lower part of the abdomen (figure A6a) and contains low contrast and high contrast inserts on relevant locations (i.e. the brain, lungs, liver) (figure A6b). The materials that were used as soft tissue substitute were referred to as Rando-Alderson material. This is a poly-urethane based material with a CT-number of 20-30 HU. The material was tweaked into the right HU by adding lead particles. Even though this phantom offers the possibility for quantitative IQA, there are several drawbacks in the design. The first drawback is that the head cannot be separated from the rest of the phantom, which can make it cumbersome to use. The second drawback is that the used materials are not representative for certain tissue types in terms of HU, as stated by the authors. (However, the relative difference between the materials within the phantom however are correct.) Therefore, this offset in HU have to be corrected for each time the phantom is being used.

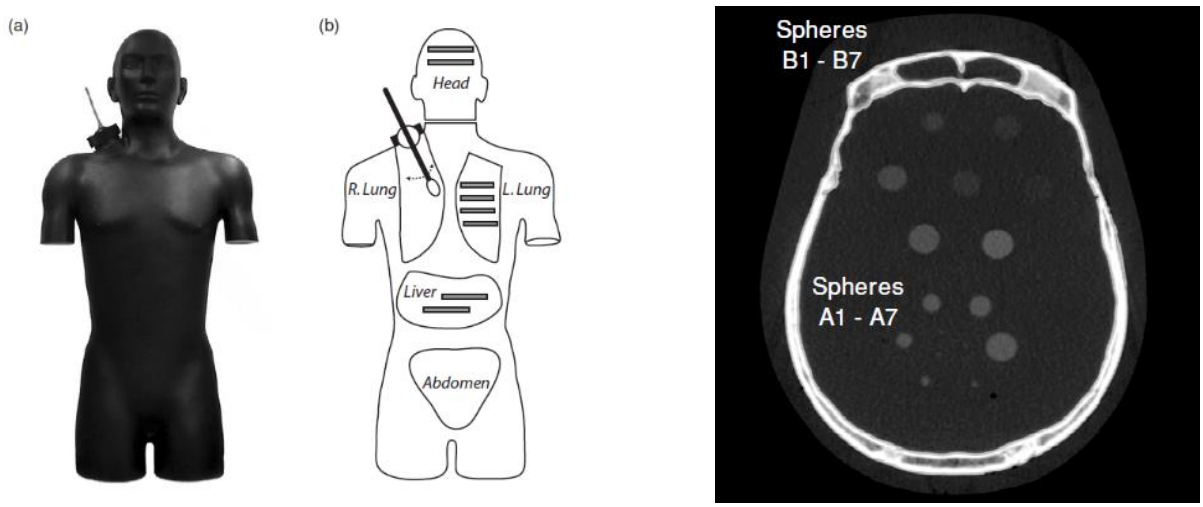

Figure A6 – a) A newly developed full body phantom (without limbs) for quantitative image quality assessment. b)The head section contains inserts with low contrast resolution inserts. Adopted from [19]

B HU VALUES OF RADIODENSITY MEASUREMENTS

The data of the measured Hounsfield Units from the calibration phantom (CP) and TEMs of chapter 5 are listed in table B1. The data for the two prototypes are listed in table B2 and B3.

Table B1 – HU measurements of the calibration phantom (CP) and TEMs from chapter 5.

TEMs	**Slice number**	**1**	**2**	**3**	**4**	**5**	**6**	**7**	**8**	**9**	**10**
CP 38	192	47	44	43	35	41	31	48	44	56	45
CP 13	110	12	17	14	4	6	15	22	18	13	17
CP -62	110	-64	-51	-61	-56	-45	-58	-55	-40	-49	-52
CP 38	150	39	48	54	30	56	46	52	48	30	47
CP 13	70	13	8	11	10	-2	15	13	-6	12	13
CP -62	70	-56	-65	-62	-48	-53	-51	-59	-62	-52	-55
CP 38	104	42	53	47	36	47	53	21	44	35	55
CP 13	50	7	11	7	10	12	6	-6	6	11	18
CP -62	50	-56	-64	-64	-63	-59	-58	-53	-59	-60	-55
MCPH	192	427	349	292	347	241	221	344	277	322	293
Nylon	192	-21	-28	-17	-26	-22	-22	-12	-30	-33	-20
SMP	192	22	45	49	38	57	43	38	42	49	31
MCPHG	192	862	918	793	944	731	998	929	896	886	1002
PMMA	192	123	100	83	117	115	135	108	143	103	129
MCPH	175	361	394	238	339	237	217	354	298	295	367
Nylon	150	-24	-29	-19	-28	-16	-19	-15	-27	-21	-10
SMP	150	50	44	37	33	38	34	40	49	51	40
MCPHG	225	749	818	776	866	802	930	935	803	820	1004
PMMA	150	104	116	116	114	115	126	157	127	119	134
MCPH	150	208	326	244	300	363	320	283	323	279	321
Nylon	235	-36	-27	-19	-21	-14	-22	-18	-15	-21	-16
SMP	104	71	54	39	42	47	48	31	39	39	42
MCPHG	255	913	996	830	769	872	959	940	982	1016	938
PMMA	100	82	115	139	139	172	137	132	129	123	95

Table B2 - HU measurements of the calibration phantom (CP) and prototype 1 from chapter 7.

Prototype 1	Slice number	1	2	3	4	5	6	7	8	9	10
CP 38	120	49	56	47	54	59	52	51	48	56	51
CP 13	120	28	29	32	24	22	18	7	18	26	20
CP -62	120	-47	-47	-54	-51	-46	-42	-42	-44	-41	-42
CP 38	80	60	59	53	55	54	65	45	51	56	56
CP 13	80	30	37	39	30	21	23	10	29	27	29
CP -62	80	-39	-38	-37	-32	-35	-28	-35	-36	-30	-37
CP 38	30	65	59	64	59	59	60	64	67	61	60
CP 13	30	34	40	39	34	31	26	22	33	34	33
CP -62	30	-32	-33	-39	-39	-32	-24	-40	-31	-30	-36
MCPH	190	276	309	281	282	258	270	272	400	356	308
Nylon	190	-26	-11	-16	-27	-23	-17	-25	-16	-26	-41
MCPH	215	284	303	253	259	290	353	234	360	328	313
Nylon	215	-21	-28	-31	-14	-24	-11	-18	-10	-8	-8
MCPH	240	294	343	319	245	384	304	233	273	286	286
Nylon	240	-14	-14	-21	-24	-24	-18	-21	-10	-17	-18

Table B3 - HU measurements of the calibration phantom (CP) and prototype 2 from chapter 7.

Prototype 2	Slice number	1	2	3	4	5	6	7	8	9	10
CP 38	70	25	23	37	42	39	35	29	30	40	30
CP 13	70	15	10	5	2	1	1	4	11	10	9
CP -62	70	-62	-65	-69	-57	-57	-59	-54	-59	-57	-60
CP 38	32	30	35	38	25	26	42	19	41	46	49
CP 13	32	20	15	18	10	-1	11	1	-12	18	6
CP -62	32	-51	-54	-50	-49	-52	-47	-57	-56	-45	-50
CP 38	50	41	38	38	58	31	58	41	25	35	31
CP 13	50	19	17	18	24	14	4	14	11	18	-2
CP -62	50	-55	-52	-55	-51	-51	-45	-46	-57	-47	-35
Nylon	192	-38	40	-10	-7	-21	80	-53	30	-107	-26
SMP	192	52	47	47	44	51	40	46	45	46	46
MCPHG	192	999	915	873	955	768	928	845	834	765	863
Nylon	225	-82	-45	56	66	-41	-28	-67	-97	60	-4
SMP	225	44	35	55	62	46	35	69	31	32	47
MCPHG	225	1002	1001	943	907	734	859	978	789	748	936
Nylon	160	-22	-9	-1	18	-41	-48	-15	-29	-6	-15
SMP	160	54	48	51	58	50	56	47	49	45	55
MCPHG	160	1209	1246	889	966	864	1098	787	1051	1021	1116

C MEASURED VERSUS SIMULATED SCATTER FUNCTIONS

The following figures (figure D1 to D6) are the measured scatter functions of the TEMs, plotted along the simulated scatter functions of the tissue type these TEMs should resemble.

C1 MCPH GRAINS

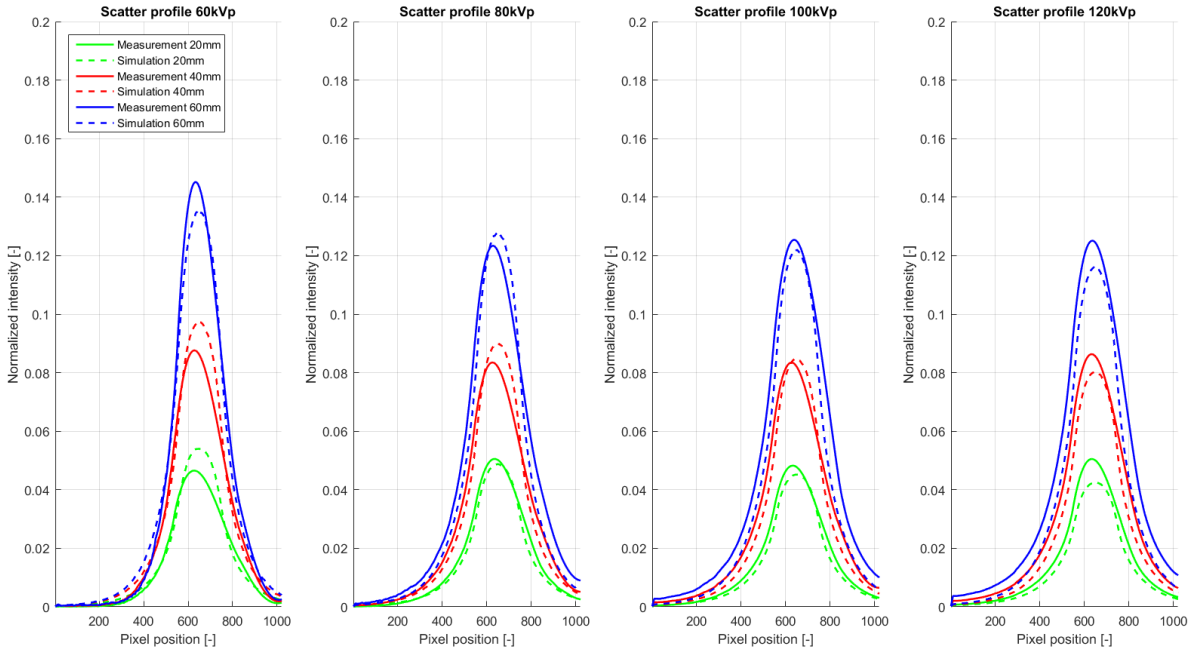

C2 NYLON

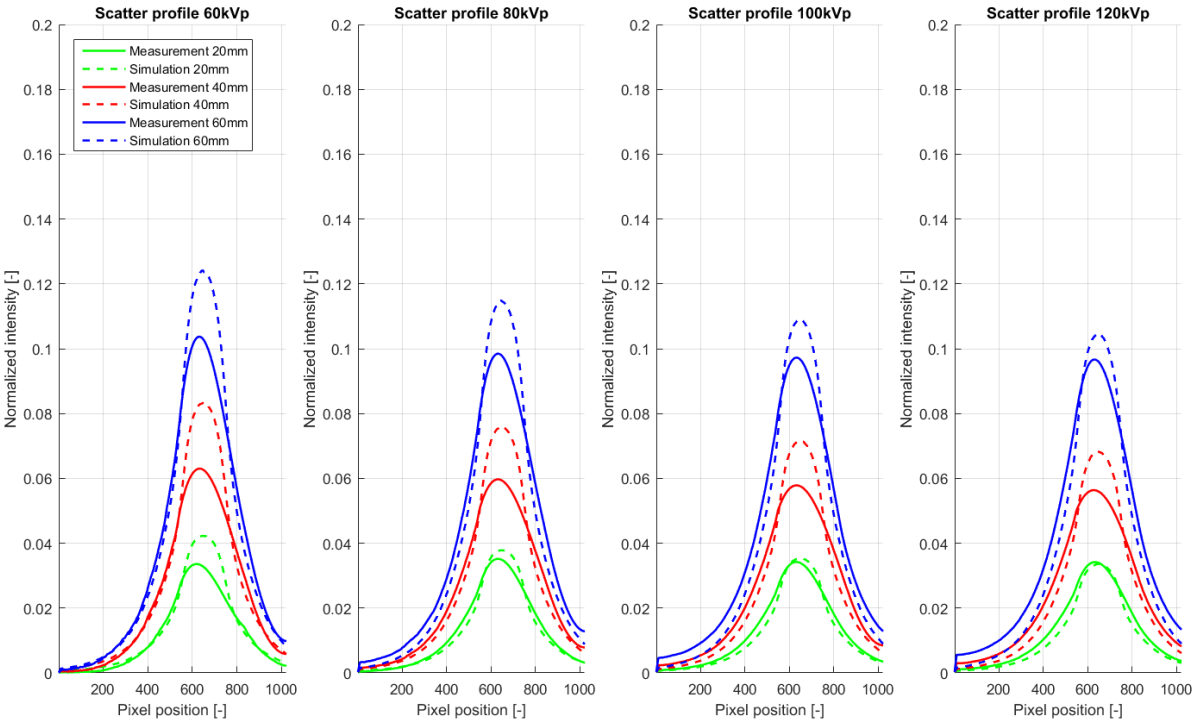

C3 SMP

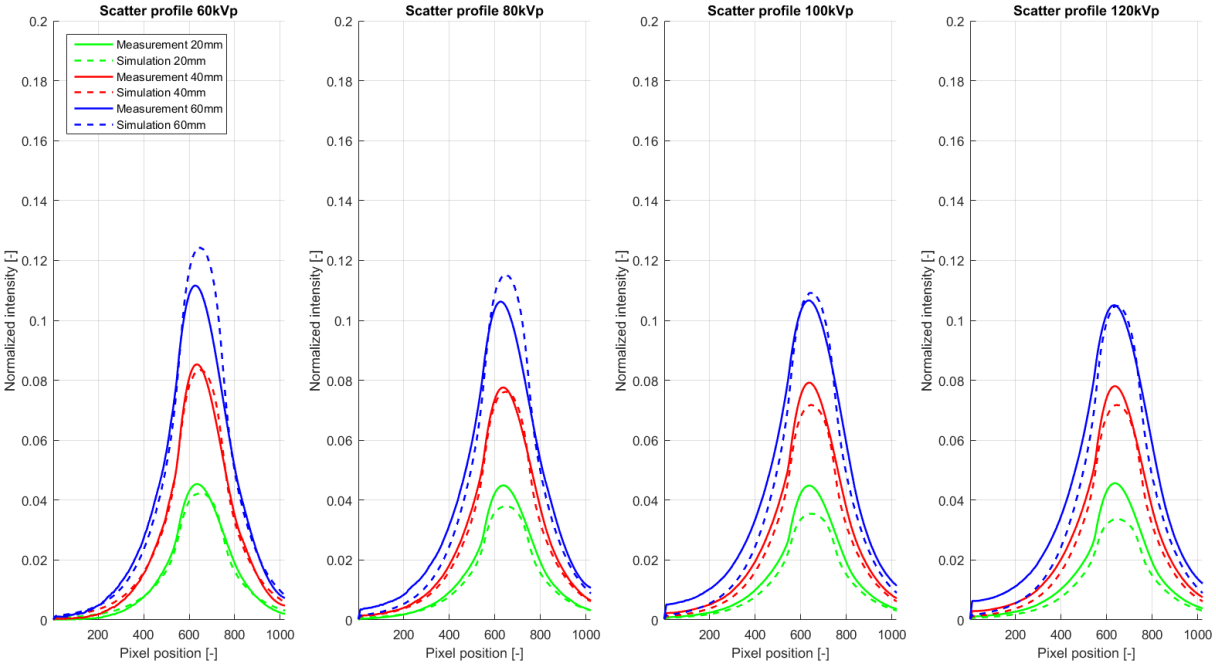

C4 MCPHG

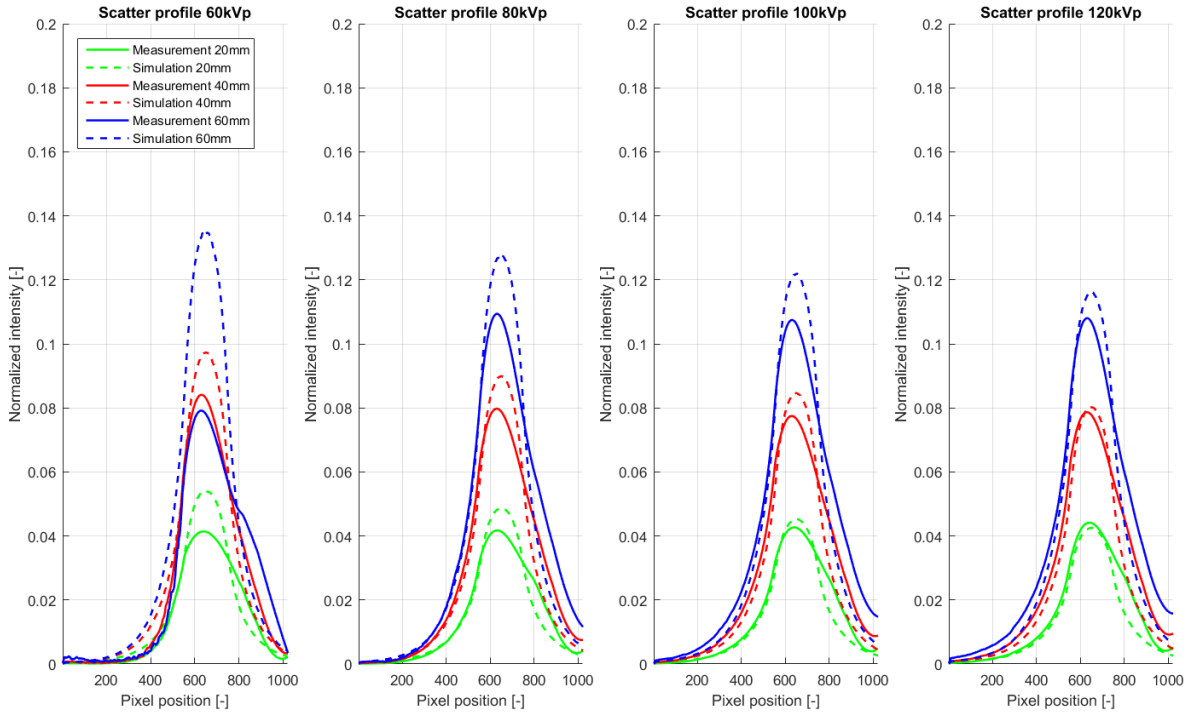

C5 PMMA PIETERBUREN LAB

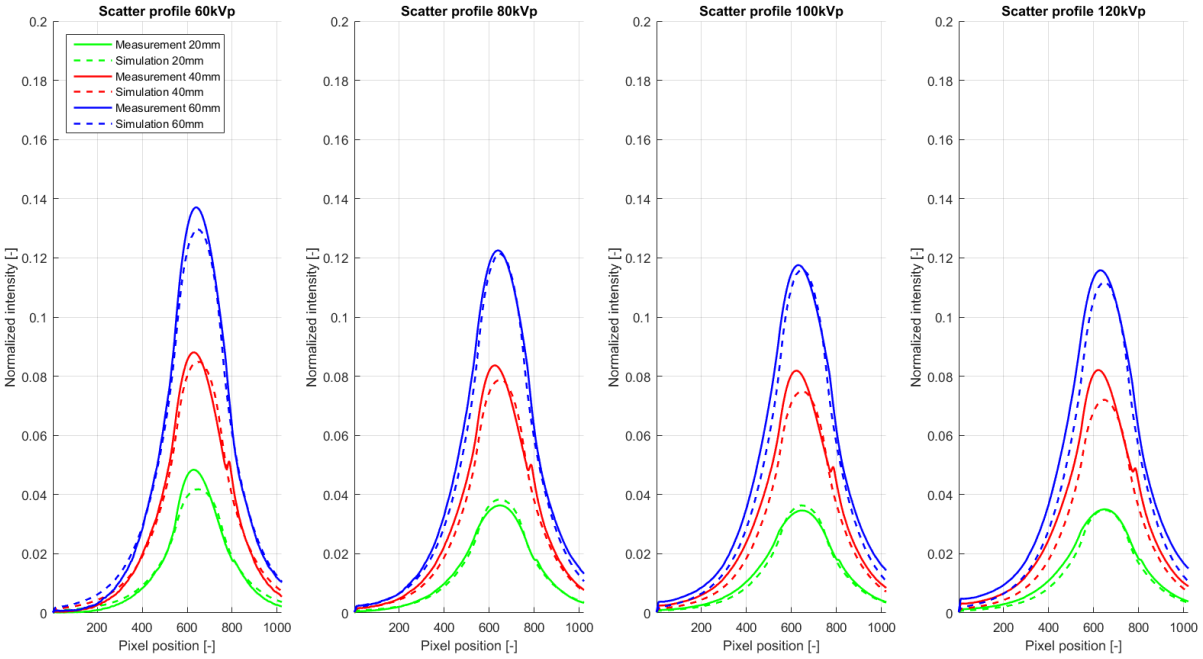

C6 PMMA IGIT LAB

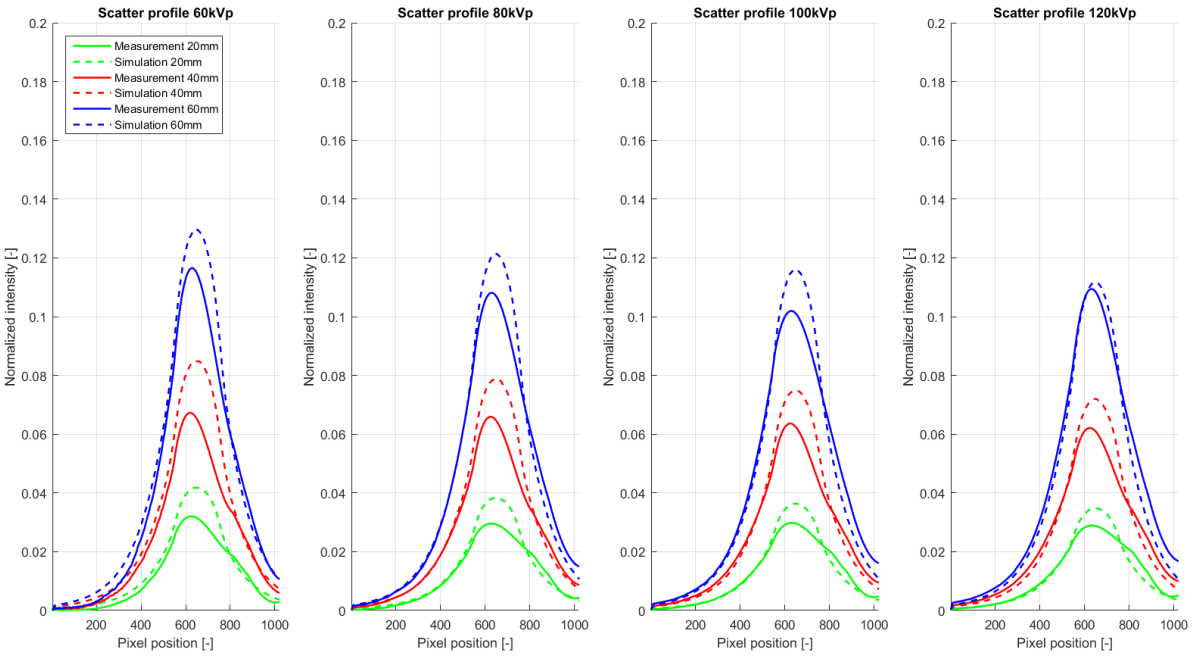

D IMAGES OF MEASURED TEMS

The following figures (E1a to E6c) are the measured images of the detector and the mean ESF, primary function and scatter functions that were derived from these images. The figures are all measurements that were performed at 120 kVp, for TEMs with 20mm (a), 40 mm (b) and 60 mm (c) thickness.

D1A – MCPH 20 MM, 120 KVP

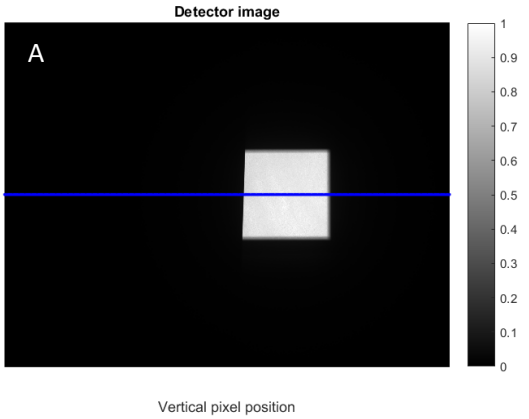

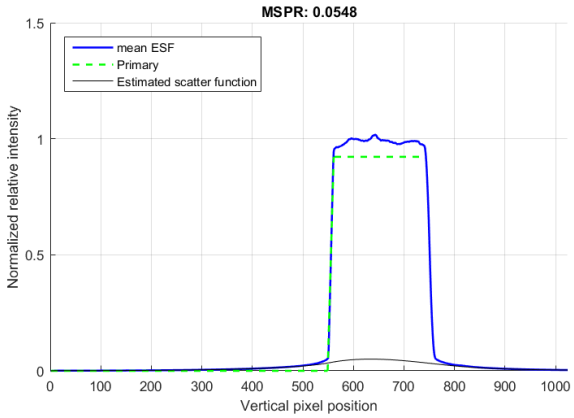

D1B – MCPH 40 MM, 120 KVP

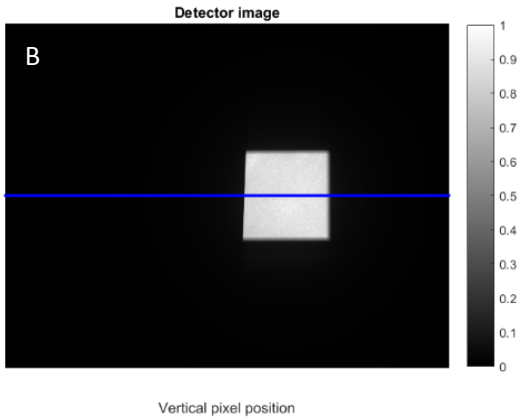

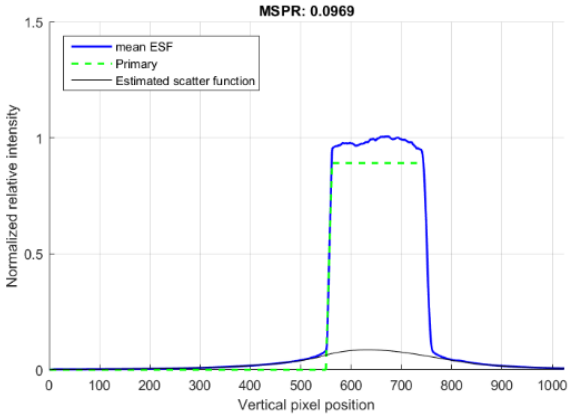

D1C– MCPH 60 MM, 120 KVP

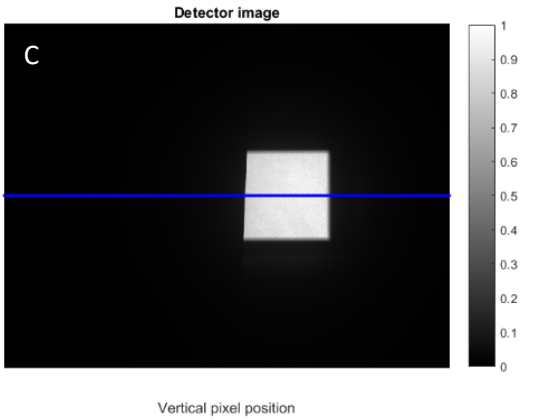

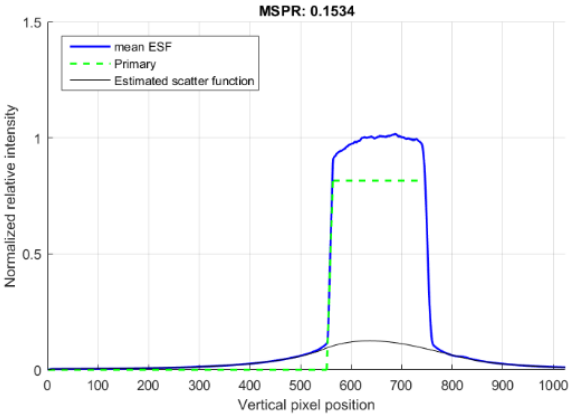

D2A - NYLON 20 MM, 120 KVP

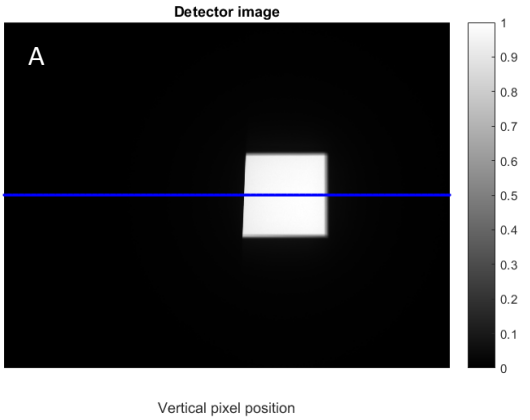

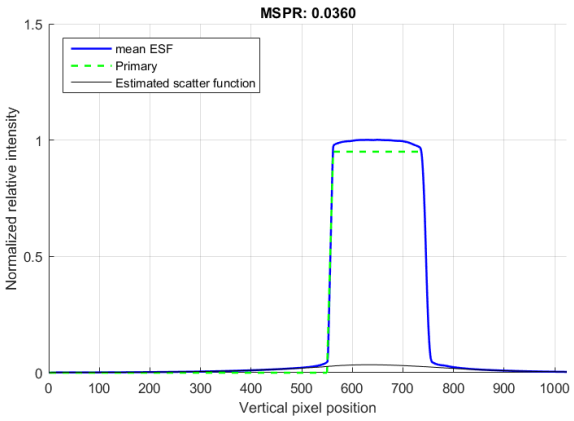

D2B - NYLON 40 MM, 120 KVP

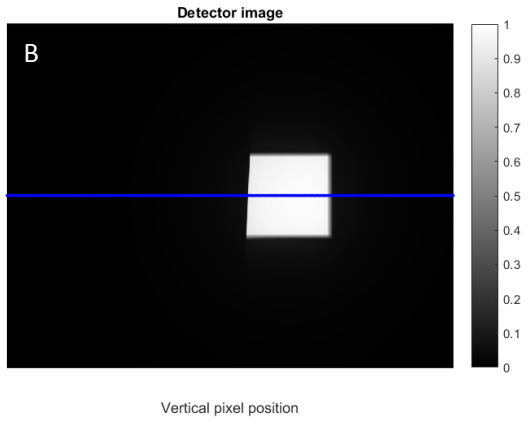

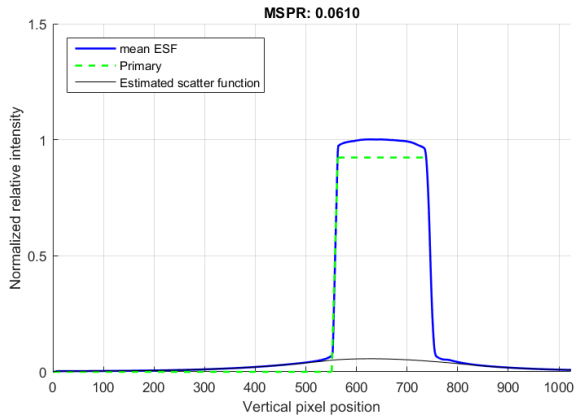

D2C - NYLON 60 MM, 120 KVP

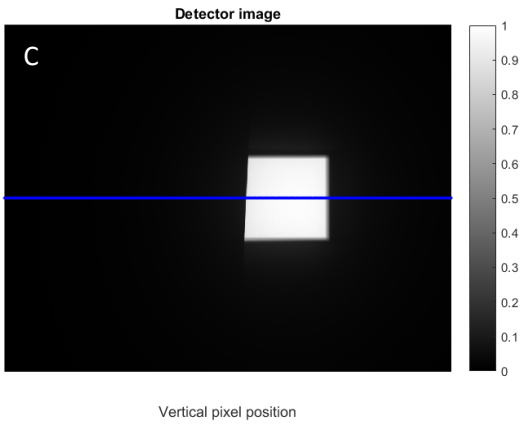

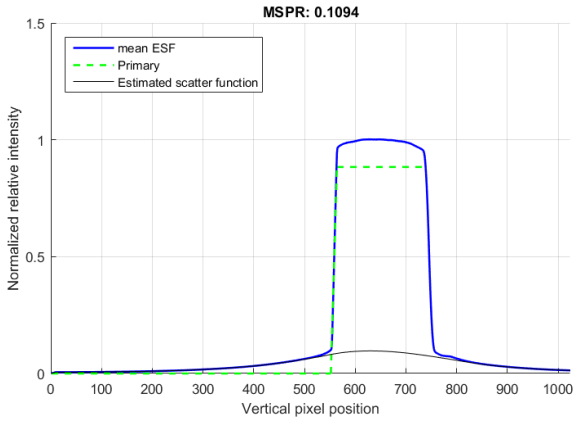

D3A - SMP 20 MM, 120 KVP

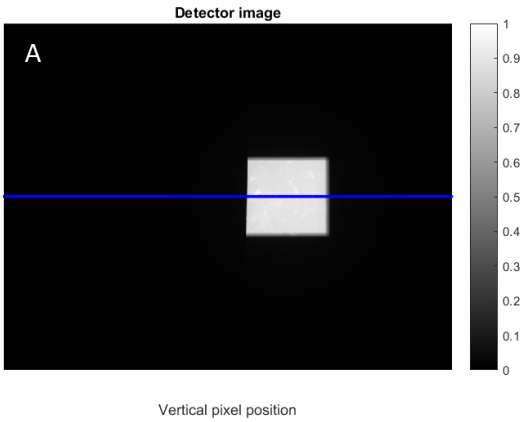

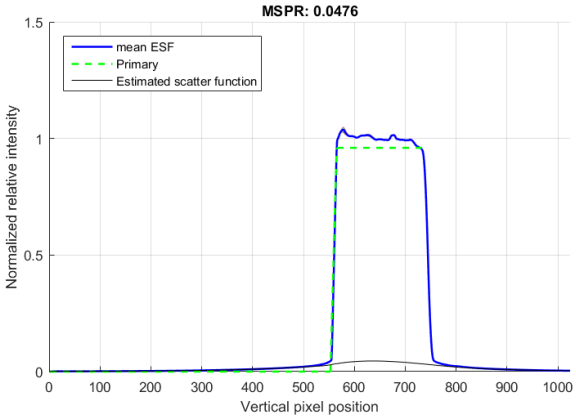

D3B - SMP 40 MM, 120 KVP

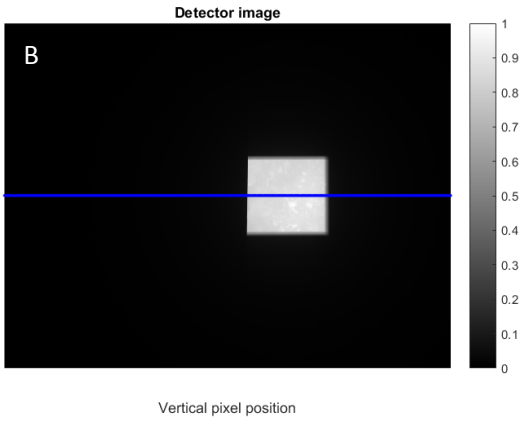

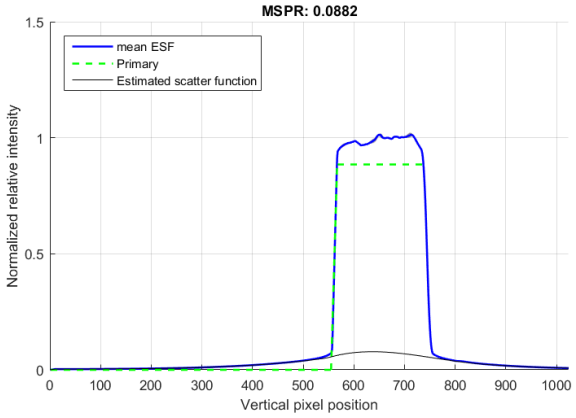

D3C - SMP 60 MM, 120 KVP

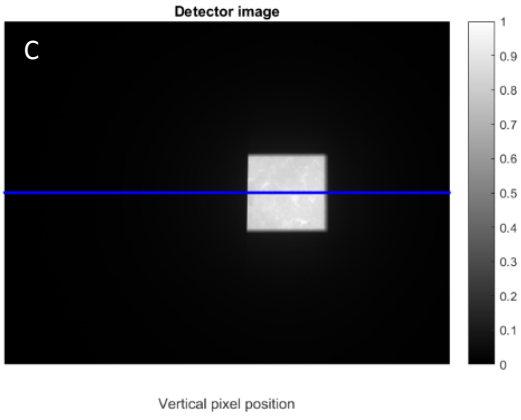

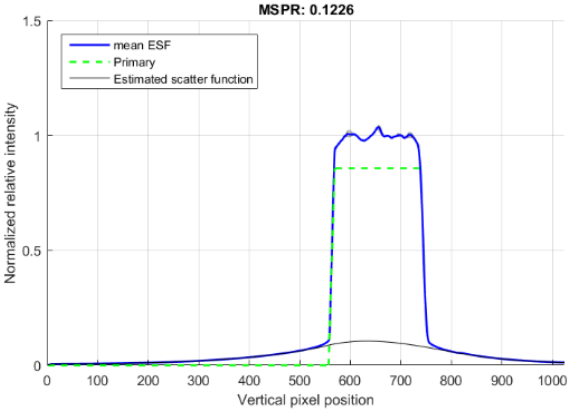

D4A – MCPHG 20 MM, 120 KVP

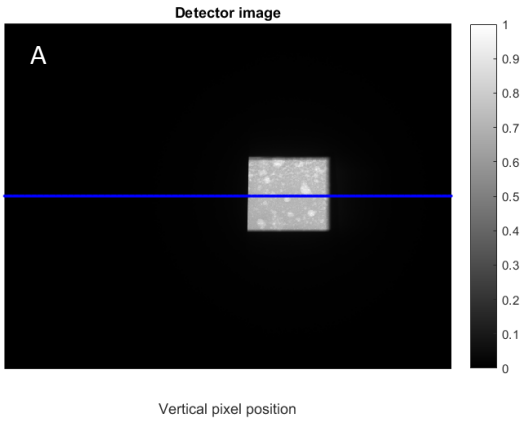

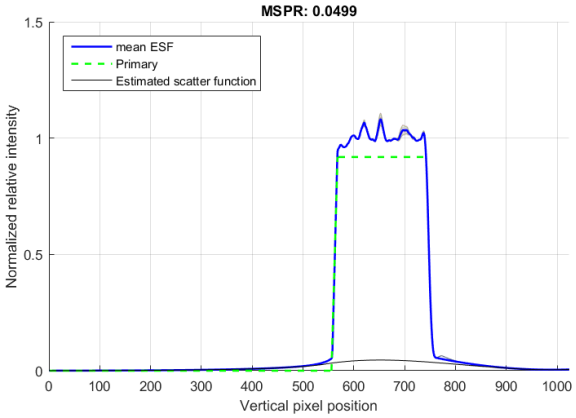

D4B – MCPHG 20 MM, 120 KVP

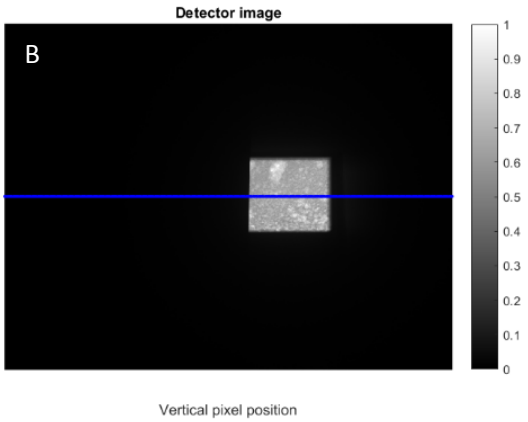

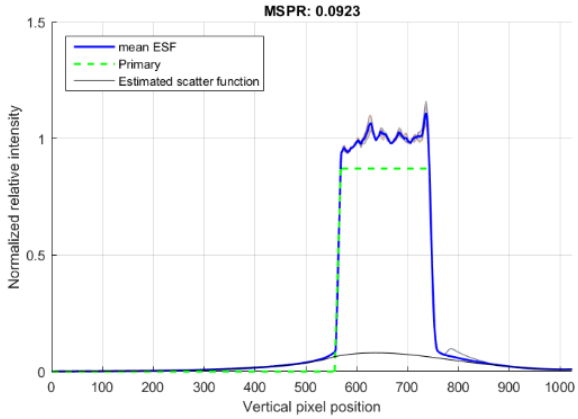

D4C – MCPHG 20 MM, 120 KVP

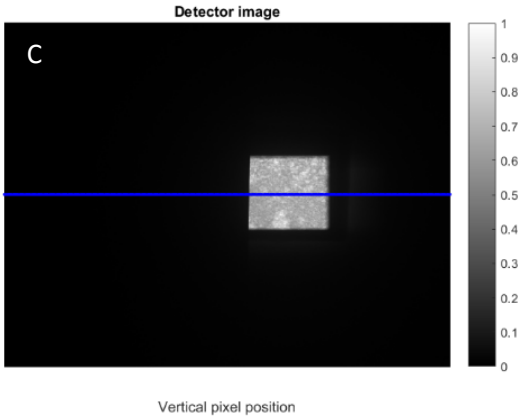

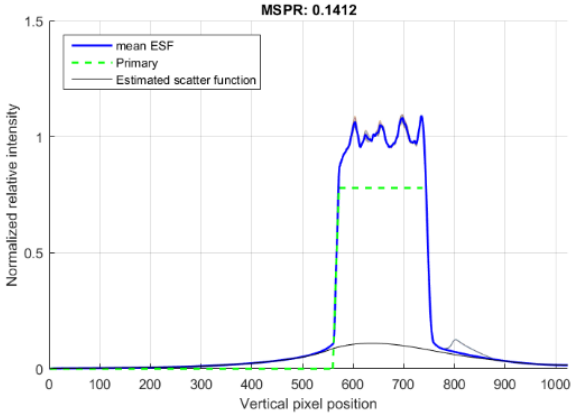

D5A - PMMA PIETERBUREN LAB 20 MM, 120 KVP

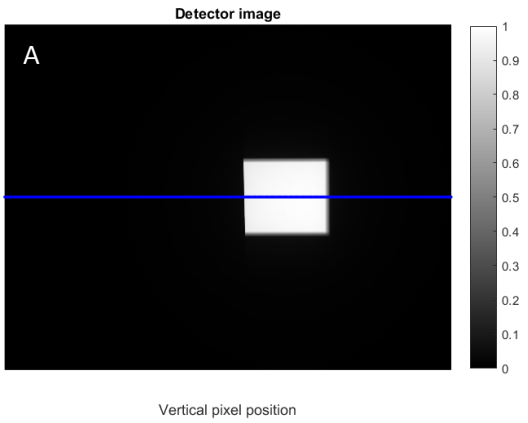

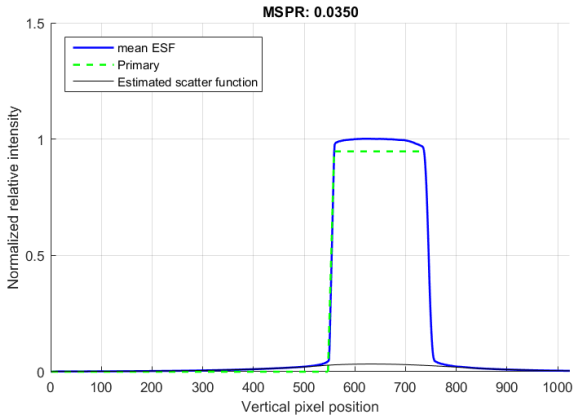

D5B - PMMA PIETERBUREN LAB 40 MM, 120 KVP

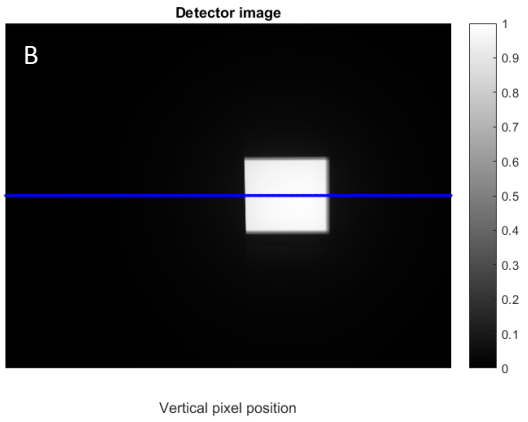

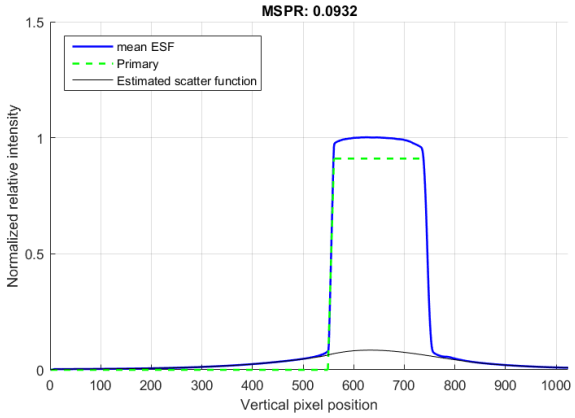

D5C - PMMA PIETERBUREN LAB 60 MM, 120 KVP

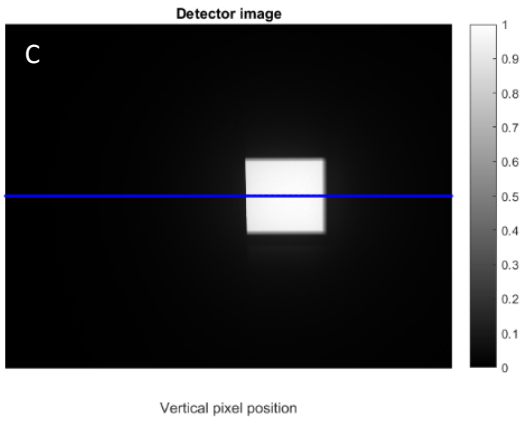

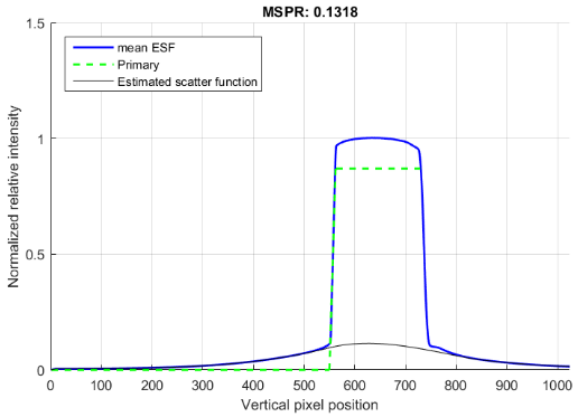

D6A - PMMA IGIT LAB 20 MM, 120 KVP

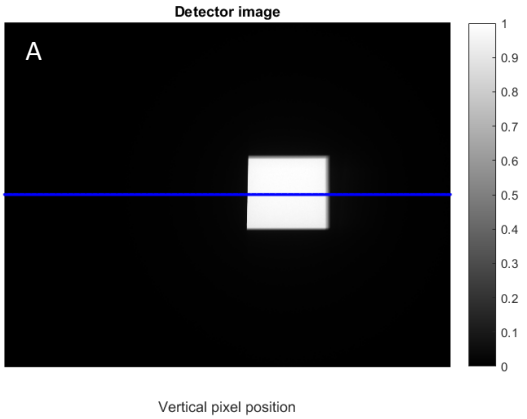

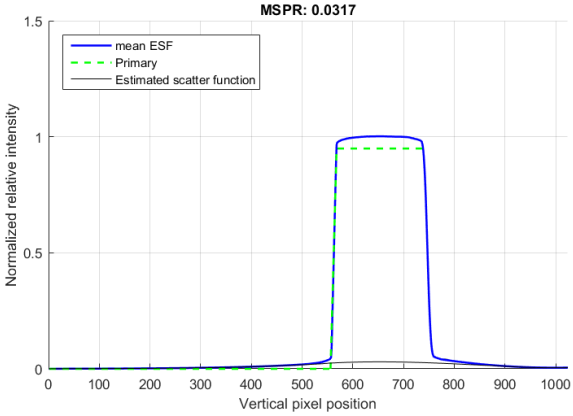

D6B - PMMA IGIT LAB 40 MM, 120 KVP

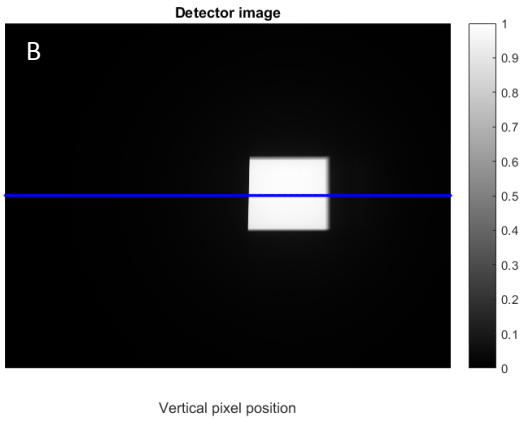

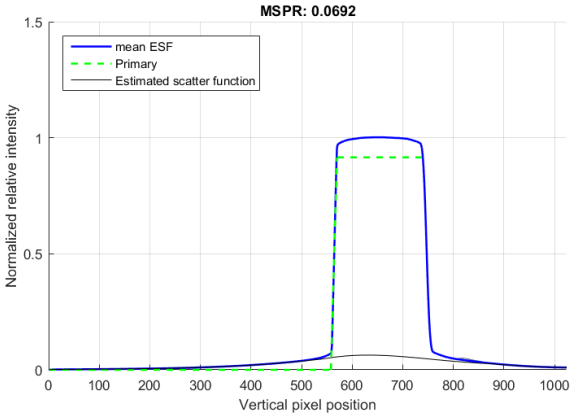

D6C - PMMA IGIT LAB 60 MM, 120 KVP